

2019-05

ELECTRONIC STRUCTURE IN VERTICALLY STACKED TRANSITION METAL DICHALCOGENIDES

CORTÉS MUÑOZ, NATALIA

<https://hdl.handle.net/11673/53694>

Repositorio Digital USM, UNIVERSIDAD TECNICA FEDERICO SANTA MARIA

Electronic Structure in Vertically Stacked Transition Metal Dichalcogenides

A thesis submitted to
the Physics Department of
Universidad Técnica Federico Santa María

In partial fulfillment
of the requirements for the degree of
Doctor en Ciencias Físicas

Presented by
Natalia Cortés Muñoz

Advisors
Dr. Luis Rosales and Dr. Pedro Orellana

May 2019

Abstract

In this thesis we theoretically investigate the electronic energy spectra of vertically stacked transition metal dichalcogenides structures, focusing in the electron charge and spin degrees of freedom. These structures are molybdenum disulphide MoS_2 bilayers with molybdenum (Mo) impurities in the interlayer region, and hybrid systems such as zigzag-terminated molybdenum ditelluride MoTe_2 nanoribbons on europium oxide EuO ferromagnetic substrate, forming MoTe_2 - EuO finite size heterostructures. We also study zigzag- and armchair-terminated MoTe_2 nanoribbons on antiferromagnetic (AFM) substrates, forming diverse MoTe_2 -AFM heterostructures.

We model MoS_2 bilayers with different stackings and incorporating Mo impurities in the interlayer region in diverse locations in a diluted regime, by means of density functional calculations including van der Waals interactions. We find that the ground state is for impurities located in hollow sites in between the layers, following octahedral crystal fields for the Mo impurities. The impurity electronic states are located in the midgap energy region with high density of states. Other less stable configurations are for impurities situated on top of a sulfur atom, following spin-polarized tetrahedral crystal fields. In these latter systems, we find larger bulk band gaps associated with larger interlayer distances, giving account of a weak van der Waals interaction due to the impurities. We reveal a stacking change from the pristine MoS_2 bilayer to a doped bilayer, driven by interstitial Mo impurities.

Zigzag- and armchair-terminated MoTe_2 nanoribbons on magnetic substrates are modeled by considering a suitable low energy three-orbital tight-binding approach, which considers realistic parameters as input, and respects the symmetries dictated by the transition metal dichalcogenide monolayers close to the band gap. We generalized this tight-binding model in order to reliably describe magnetic proximitized nanoribbons. As such, we include exchange and Rashba field terms into the pristine dichalcogenide Hamiltonian, giving account of the induced magnetism in the nanoribbons.

In the case of the hybrid MoTe_2 - EuO finite-size zigzag structure, we demonstrate that strong spin-polarized edge modes arise in the midgap energy region due to the competition of spin-orbit coupling and exchange interaction. The edge modes exhibit out-of-plane as well as in-plane spin polarization because of the induced Rashba coupling, and they are spatially confined to the zigzag edges. We show that zigzag edges act as one-dimensional conducting channels that carry spin-polarized currents while the bulk is insulating. The edge spin currents are acquired by the proximity to the mag-

netic substrate. By gating the sample to shift the Fermi energy through the optical gap, the resulting spin currents can be activated at tunable values and polarizations.

MoTe₂ zigzag nanoribbons on AFM substrates reveal enhanced parameters such as Rashba strength and spin-orbit spin splitting along the edge modes, which lie in the two-dimensional bulk energy gap. Armchair nanoribbons on AFM substrates show either, gapped or gapless midgap edge modes, which depend on the ribbon width. The edge modes carry either, charge currents or pure spin currents along the armchair edges of the sample, for different AFM ordering of the substrate.

Our results, obtained from reliable modelling and experimentally realistic parameters, suggest a pathway for effectively implementing systems with diverse functionalities. Doped MoS₂ bilayers suggest possible applications such as traps for electrons/excitons and an efficient way to control the stacking of the bilayers by Mo impurities in the growth process. MoTe₂ nanoribbons deposited on magnetic substrates may be useful for spin filters with tunable edge spin currents. We believe this work to be of general interest to researchers working on efficient solid-state electronic devices, magnetic proximity 2D materials, spin-polarized vertical structures and spintronics.

Resumen

En esta tesis investigamos teóricamente los espectros de energía electrónicos en estructuras de dicalcogenuros de metales de transición verticalmente apiladas, enfocándonos en los grados de libertad de carga y de espín del electrón. Estas estructuras son bicapas de disulfuro de molibdeno MoS_2 con impurezas de molibdeno (Mo), y sistemas híbridos como nanocintas de ditelenuro de molibdeno MoTe_2 con bordes *zigzag* sobre un sustrato ferromagnético de óxido de europio EuO , formando heteroestructuras MoTe_2 - EuO de tamaño finito. También estudiamos nanocintas de MoTe_2 con terminación *zigzag* y *brazo de silla* sobre sustratos antiferromagnéticos (AFM) formando varias heteroestructuras de tipo MoTe_2 -AFM.

Modelamos las bicapas de MoS_2 con diferentes tipos de apilamiento, incluyendo impurezas de Mo en la región intercapa en diversas posiciones y en un régimen diluido a través de cálculos de densidad funcional, incorporando interacciones tipo van der Waals. Encontramos que el estado fundamental es para impurezas localizadas en sitios vacíos entre las capas, siguiendo campos cristalinos octaedrales para las impurezas de Mo. Los estados electrónicos de impureza están localizados en la región de energía dentro del bulto con gran densidad de estados. Otras configuraciones menos estables son para impurezas situadas sobre un átomo de azufre, siguiendo campos cristalinos tetraedrales polarizados en espín. En estos últimos sistemas encontramos brechas de energía del bulto más grandes, asociados con grandes distancias intercapa, dando cuenta de una débil interacción van der Waals debido a las impurezas. Demostramos un cambio de apilamiento desde la bicapa de MoS_2 prístina hacia la bicapa dopada, conducido por impurezas de Mo intersticiales.

Las nanocintas de MoTe_2 terminadas en *zigzag* y *brazo de silla* sobre sustratos magnéticos son modeladas considerando una aproximación adecuada de baja energía, el modelo de enlace fuerte de tres orbitales. Este modelo considera parámetros realistas como entrada y respeta las simetrías dictadas por las monocapas de dicalcogenuro de metal de transición cerca de la brecha de energía del bulto bidimensional. Para describir realmente las nanocintas sujetas a proximidad magnética, generalizamos el modelo de enlace fuerte. Como tal, incluimos términos de campo de intercambio y Rashba en el Hamiltoniano prístino, dando cuenta así del magnetismo inducido en las nanocintas.

En el caso de la estructura híbrida finita con bordes *zigzag* MoTe_2 - EuO , demostramos que los modos de borde están fuertemente polarizados en espín, y surgen en la región de la brecha de energía bidimensional debido a la competencia entre el acoplamiento espín-órbita e interacción de intercambio. Los modos de borde exhiben polarización

de espín fuera y dentro del plano debido al acoplamiento Rashba inducido, y están espacialmente confinados en los bordes *zigzag*. Mostramos que los bordes *zigzag* actúan como canales conductores unidimensionales, los que llevan corrientes de espín polarizadas mientras el bulto es aislante. Las corrientes de espín en la nanocinta con bordes *zigzag* son adquiridas por la proximidad con el sustrato magnético. A través de un potencial de puerta sobre la muestra para sintonizar la energía de Fermi dentro de la brecha de energía óptica, las corrientes de espín resultantes pueden ser activadas a valores y polarizaciones sintonizables.

Las nanocintas *zigzag* de MoTe_2 sobre sustratos AFM revelan parámetros Rashba mejorados, tales como fuerza Rashba y separación de espín tipo espín-órbita a lo largo de los modos de los bordes, los que caen en la brecha de energía del bulto bidimensional. Las nanocintas *brazo de silla* sobre sustratos AFM muestran ya sea modos de borde con una brecha de energía o sin brecha de energía, lo que depende del ancho de la nanocinta. Estos modos de borde llevan ya sea corrientes de carga o corrientes puras de espín a lo largo de los bordes de la muestra, para diferentes órdenes AFM de los sustratos.

Nuestros resultados obtenidos de modelamientos confiables y parámetros experimentalmente realistas, sugieren un camino para implementar efectivamente sistemas con diversas funcionalidades. Las bicapas dopadas de MoS_2 sugieren posibles aplicaciones como trampas para *excitones* y una manera eficiente para controlar el tipo de apilamiento de las bicapas en el proceso de crecimiento, a través de impurezas de molibdeno. Las nanocintas de MoTe_2 depositadas sobre sustratos magnéticos podrían ser útiles para aplicaciones como filtros de espín llevando corrientes de espín sintonizables en los bordes de la muestra. Confiamos en que este trabajo será de interés general para investigadores trabajando en dispositivos electrónicos eficientes de estado sólido, materiales bidimensionales sujetos a proximidad magnética, estructuras verticales polarizadas en espín y espintrónica.

Agradecimientos

Este proceso ha sido un largo camino que he recorrido junto a valiosas y maravillosas personas. Agradezco a cada uno de ustedes por haber sido parte de esta inolvidable aventura. A mi amada familia por entregarme su apoyo en esta etapa 'final' de formación.

A las personas con las que he tenido la oportunidad de colaborar y compartir durante este proceso. Profesor Sergio E. Ulloa gracias por haberme hecho sentir una más del grupo en Ohio University, por el apoyo y confianza que me ha entregado durante todo este tiempo de estudio. Profesor Andrés Ayuela, gracias por tu apoyo y por haberme recibido en San Sebastián. A ambos les agradezco todo el conocimiento y enseñanzas que me entregaron durante esta última etapa. Profesores Pedro Orellana y Luis Rosales, gracias por los años de tutoría y los buenos momentos compartidos. Dr. O. Ávalos-Ovando, gracias por la amistad y por el constante feedback. Dr. Luis E. F. Foa Torres, Dr. Patricio Vargas y Dr. Patricio Häberle, gracias por haber aceptado ser parte de la comisión evaluadora.

Mis amigos especiales Freddie y Maria Luisa, gracias por la honestidad y por entregarme los máximos momentos de inspiración. A mis amigos Oscar, JP, Andrés, Mary, Karin, Verito, Marta, Romain, Tomás, Jhon, Fanny y Carina, gracias por los buenos y distractivos momentos durante los periodos de pasantías y momentos libres, las salidas de pinchos, los icazos, los paseos, los asados y los carretes. Gracias amigas de mi gran Iquique glorioso, Luna, Pamela, María José y Julia por estar presentes y compartir siempre conmigo inolvidables recuerdos y emociones.

Quisiera agradecer el apoyo financiero otorgado por la Universidad Técnica Federico Santa María, proyecto Internacionalización de Doctorados FSM 1204, beca Doctorado Nacional Conicyt, becas de investigación y estadía en el extranjero por parte de DGIIP USM y proyectos Fondecyt.

Finalmente, quisiera expresar que esta historia ha sido única y apasionante, me siento agradecida por haber tenido y por seguir teniendo siempre en mis manos la decisión y oportunidad de aportar desde la profunda verdad al conocimiento científico de la física.

List of Acronyms

• 1D	One Dimensional
• 1DEG	One Dimensional Electron Gas
• 2D	Two Dimensional
• 2DEG	Two Dimensional Electron Gas
• 3D	Three Dimensional
• 3OTB	Three-Orbital Tight Binding
• AFM	Antiferromagnetic
• BZ	Brillouin Zone
• CVD	Chemical Vapor Deposition
• DFT	Density Functional Theory
• DoF	Degree of Freedom
• FET	Field Effect Transistor
• FFT	Fast Fourier transform
• FM	Ferromagnetic
• LDOS	Local Density of States
• LEH	Low Energy Hamiltonian
• MBE	Molecular Beam Epitaxy
• MEF	Magnetic Exchange Field
• MPE	Magnetic Proximity Effect
• NN	Nearest Neighbor
• NNN	Next-Nearest Neighbor
• PBC	Periodic Boundary Condition

• PE	Proximity Effect
• POC	Projected Orbital Component
• SK	Slater Koster
• SOC	Spin-Orbit Coupling
• STM	Scanning Tunneling Microscopy
• TB	Tight Binding
• TMD	Transition Metal Dichalcogenide
• TRS	Time Reversal Symmetry
• VBM	Valence Band Maximum
• vdW	van der Waals

Contents

1	Introduction	1
2	Theoretical and Conceptual Background	6
2.1	Transition Metal Dichalcogenides	6
2.1.1	Pristine TMD Monolayers	9
2.1.2	Finite Size Structures	10
2.1.3	Molybdenum Disulphide Bilayers	12
2.2	Two-Bands $k \cdot p$ Model	15
2.3	Transition Metal Dichalcogenide Tight-Binding Hamiltonians	17
2.3.1	Three-Orbital Tight-Binding Hamiltonian	18
2.4	Rashba Spin Orbit Coupling in a 2D Electron Gas	23
2.4.1	Rashba Spin Orbit Coupling in a 1D Electron Gas	24
2.4.2	Extrinsic Rashba field	26
2.5	Magnetic Proximity Effects	26
2.6	Spin Currents	28
3	Stacking Change in MoS₂ Bilayers Induced by Interstitial Molybdenum Impurities	31
3.1	MoS ₂ bilayers with Mo Impurities	32
3.1.1	Energy and Geometry	32
3.1.2	Electronic Properties	34
3.1.3	Stacking Change	38
3.2	Final Remarks	40
4	Tunable Spin-Polarized Edge Currents in Proximitized Transition Metal Dichalcogenides	41
4.1	Pristine MoTe ₂ Zigzag Ribbons	42
4.2	Magnetized 3OTB Hamiltonian	44
4.3	Spin Projections	47

4.4	Edge Spin Currents	49
4.4.1	Pristine Spin Currents	50
4.4.2	Defective Spin Currents	53
4.5	Final Remarks	57
5	MoTe₂ Ribbons Proximitized to Antiferromagnetic Substrates	58
5.1	System	59
5.2	Tight-Binding Description	60
5.3	Zigzag-terminated Ribbons	61
5.4	Armchair-terminated Ribbons	67
5.5	Final Remarks	72
6	Conclusions	73
	References	63
	Appendix	
A	MoS₂ Bilayers	95
A.1	Simulation Details	95
A.2	Mo Impurities in 3R Phase	96
B	MoTe₂ Zigzag Ribbons with Defects	98
B.1	Vacancies	100
B.1.1	Te Vacancies at the Edges	100
B.1.2	Mo Vacancies at the Edges	101
B.1.3	Vacancies in the bulk	102
C	Pristine Armchair Ribbons	103
D	List of Publications and Presentations	106
D.1	Publications	106
D.2	Other publications	106
D.3	Work in progress	107
D.4	Presentations	107
D.4.1	Oral presentations	107
D.4.2	Posters presentations	108
E		109

E.1	Fellowships	109
E.2	Internships	109

List of Figures

2.2	(a) Top view for the MX_2 TMD monolayer, the red rhomboid indicates the unit cell with lattice constant a (M-M distance), the green triangle stands for the trigonal prismatic coordination. Blue (yellow) spheres indicate M (X) atoms. (b) The hexagonal Brillouin zone in reciprocal 2D space with vectors \vec{b}_1 and \vec{b}_2 (red arrows). High symmetry points Γ , $\pm Q$, M , K and K' are shown.	10
2.3	(a) Top view of a schematic 2D TMD monolayer square ribbon, with representative zigzag and armchair edges as shown. N and H are the dimensions for the ribbons when defined edges are considered. \mathbf{R}_1 through \mathbf{R}_6 are the lattice vectors connecting metal-metal (M-M) NN, shown by red arrows. Green rhomboid and magenta rectangle stand for the zigzag and armchair unit cells, respectively. (b) BZ for the 2D monolayer (black), as well as the reduced BZ for the ribbon with defined zigzag and armchair edges (brown). The high symmetry points are marked in the BZ as indicated.	12
2.4	Diverse stackings for MoS_2 bilayers with low energy: (a) 3R-AB, (b) 2H-AA' and (c) 2H-AB', which refers to different stacking types in the bilayer with 2H phase. Mo atoms are shown as cyan (Mo top) and purple (Mo bottom) spheres, sulfur atoms are shown as yellow spheres. Inset shows the Mo impurity location as red crosses relative to the bottom layer in B (bridge), H (hollow), T (top over Mo) and T' (top over S).	14
2.5	Band structures along high symmetry points in the BZ for the most stable MoS_2 pristine bilayers (in stability order in these calculations): (a) 3R-AB, (b) 2H-AA' and (c) 2H-AB'. The layer orientation for the different stackings can be seen in Fig. 2.4. The Fermi energy is set to zero eV.	14

2.6	(a) Band structure within the 3OTB model for MoTe ₂ 2D monolayer with SOC given by Eq. 2.7. Blue (red) colors correspond to spin up (down) conduction and valence bands, green color stand for conduction bands with higher energy. The MoTe ₂ gap at the valleys is $\simeq 1$ eV, while the SOC splitting of the valence band is $\Delta_{\text{SOC}} = 0.215$ eV. The VBM is set to zero energy. (b) Discrete energy levels for a MoTe ₂ square ribbon with $N_{\text{sites}} = 1600$ Mo sites, modeled with Eq. 2.8. The discrete spectrum as black dots shows midgap states with metallic character. The midgap levels are 1D-like extended states localized at the sample edges. Note that here we show the sorted eigenenergies, with the horizontal axis just listing the increasing electronic states.	21
3.1	Total and binding energy as a function of the structural configurations of Mo impurities within the MoS ₂ bilayer. The red spheres indicate the Mo impurity in each configuration. The relaxed structures are included, grouped in octahedral (T-AB' and H-AA') and tetrahedral (T'-AB' and T'-AA') structures of sulfur atoms around Mo impurities. The zero energy point is set for the most energetically favorable structure, namely, the T-AB' configuration. The top insets show the octahedral and tetrahedral configurations for the Mo _{imp} atom, and the relaxed side and top views structures are given for each configuration.	33
3.2	(a-c) Band structures for the given configurations. GS in T-AB' configuration indicates the ground state. The Fermi energy is set to 0 eV. Orange rectangles enclose the Mo _{imp} bands separated into several different energy regions, labeled as 1 , 2 and 3 . (d-f) Local density of states (LDOS) projected in space for the Mo _{imp} bands in the band gap region of the MoS ₂ bilayer.	35
3.3	Ligand field splitting for Mo _{imp} <i>d</i> -orbitals produced by the neighboring sulfur atoms in (a) octahedral and (b) tetrahedral environments.	36
3.4	(a) Energy profile and (b) interlayer distance (Δ_z) by sliding between the 2H stackings. The sliding coordinate goes along the armchair direction. Full lines are just guiding to the eyes. Energies and distances shown are referenced with respect to the most stable configuration, that is, the T-AB'.	39

4.1	(a) Top view of a free-standing pristine MoTe ₂ ribbon with zigzag Te and Mo-edges. N is the length and H is the width of the ribbon. For this example, $N = 5$ and $H = 5$, so that the ribbon have $N_{sites} = N \times H = 25$ Mo sites. (b) Schematic representation of the MoTe ₂ ribbon in proximity to a FM substrate such as EuO. Eu atoms are hidden directly below the Mo atoms (blue spheres).	43
4.2	Energy spectrum for the MoTe ₂ zigzag-terminated ribbon projected with spin $s_z = \uparrow, \downarrow$, of size $N = 40$, $H = 40$ (1600 Mo sites) for the pristine case in panel (a), when the MoTe ₂ ribbon is on the EuO substrate in panel (b). In both cases, the Mo edge modes are shown as green symbols, while orange symbols stand for the Te edge modes (see insets). Black (gray) dots characterize the bulk energy dispersion for spin up (down). In (a), the Mo and Te edge modes as well as the valence and conduction bulk states are TRS related. In (b), the spectrum shows TRS breaking, associated with a valley splitting in the valence bulk bands, as well as to strongly spin-polarized edge modes in the bulk gap. The pristine in (a), and the magnetic-proximitized in (b) dispersions correspond to systems schematically shown in Fig. 4.1(a) and (b) respectively.	44
4.4	Spin projections of energy spectrum near bulk gap along the zigzag edges of a MoTe ₂ ribbon on EuO. In (a)-(b) the exchange fields for EuO B_v and B_c are 100%. (a) Shows spin projections along the Y direction (S_Y); (b) along the Z direction (S_Z). In (b) Te_{\pm} , Mo_{\pm} label in-gap 1D edge modes located on the Te and Mo-edges termination, respectively. (c)-(d) Spectrum and S_Y , S_Z for weaker exchange fields as shown; notice smaller (larger) S_Z (S_Y) projection amplitudes than in (a) and (b). Gray lines indicate selected midgap Fermi levels used in Fig. 4.5. Color bar indicates positive (negative) spin projection as blue (red) gradient. . . .	48
4.5	Spin currents $\mathbf{j} = (j_Y, j_Z) = m\mathbf{j}^{spin}/\hbar$ for system in Fig. 4.4(c)-(d), for both Mo (green arrows) and Te (orange arrows) ribbon edges. Results for different Fermi levels, E_{F1} (a), E_{F2} (b) and E_{F3} (c). The spin current is along the zigzag direction ($k > 0$). The arrow's size (direction) indicates the magnitude (orientation) of the spin current. The magnetic substrate is not shown and the ribbon size is only schematic. E_{F4} yields similar results to E_{F3} (not shown).	51

4.6	(a) Analytical bands for Mo-edge (green lines) and Te-edge (orange lines) from Eq. (4.12) and TB bands (gray dots and color triangles); Mo _{+,−} and Te _{+,−} bands highlighted as up/down color arrows, for system in Fig. 4.4(c)-(d). (b) Spin current components j _Z (solid) and j _Y (dotted) obtained from analytical model for Mo-edge, and (c) for Te-edge, for $k > 0$. Symbols in (b) and (c) are numerical values as seen in Fig. 4.5. The 1D effective analytical model captures the dispersions, wave functions and the spin currents of the TB results.	53
4.7	Results for vacancies on the Mo-edge. (a) Pristine dispersion, (b) spin current j _Y , and (c) j _Z for midgap states obtained from magnetized 3OTB model calculations. In (b) and (c), the spin currents for pristine edges are shown as empty symbols, while cases for different molybdenum (Mo _v) or tellurium (Te _v) vacancy concentrations are shown as indicated by different lines (1: 2.5%, 2: 5%, and 5: 12.5% on edge).	55
4.8	Results for vacancies on the Te-edge. (a) Pristine dispersion, (b) spin current j _Y , and (c) j _Z in midgap region, as obtained from magnetized 3OTB calculations. In (b) and (c), spin currents for pristine edges are shown as empty symbols. Different molybdenum (Mo _v) or tellurium (Te _v) vacancy concentrations are shown as indicated by different lines (1: 2.5%, 2: 5%, and 5: 12.5% on edge).	56
4.9	Spin current along Mo-edge vs concentration of Mo _v on the Mo-edge. Symbols are 3OTB averaged between 0.6 and 0.8 eV ($\simeq E_{F3}$ and E_{F4}), and lines are exponential fits, Eq. 4.15, with $l = Y, Z$ as indicated. . . .	56

5.1	<p>Schematic representation of MoTe₂ ribbons when in proximity to AFM substrates with different magnetic ordering, AFM1 in (a), AFM2 in (b). The AFM substrates are not shown, the ribbon size and shape is only schematic. The zigzag edges are along x direction (N), armchair edges are along y direction (H). At $y = 0$ we obtain the Mo-zigzag edge, while at $y = H$ the Te edge is obtained. Conversely, at $x = 0$ we obtain the left-armchair edge, while at $x = N$ we obtain the right-armchair edge. For this example, both MoTe₂-AFM systems have dimension $N = 4$ and $H = 4$, then $N_{sites} = 16$ Mo sites. The top views in (a)-(b) are slightly tilted for a better visualization of the projected moments on the Mo atoms, shown as blue: up moment and red: down moment arrows, where equal amount of red and blue arrows identifies a net zero magnetic moment in either AFM system. Magenta (black) rectangles stand for the magnetic (geometric) unit cells in the ribbon. In (a) the magnetic cell is twice the geometric cell along the zigzag direction, in (b) both cells are the same.</p>	60
5.2	<p>Spin projections of the energy spectrum for the zigzag-terminated ribbon in the MoTe₂-AFM1 system in Fig. 5.1(a). In (a) and (b) the extrinsic Rashba field λ_R is 100%, (d) and (e) the Rashba field is set to 50%. (a) and (d) stand for S_Y projection, (b) and (e) stand for the S_Z projection. Note that S_X projection vanishes due to the Rashba symmetry of the system. Mo₁, Mo₂ and Te indicates the Rashba-type edge modes in the bulk midgap. Green (orange) solid lines indicate Mo₁ (Te) higher energy bands $E_+^{Mo_1}$ (E_+^{Te}), respectively. (c) and (f) are the spin expectation values (or spin projections) along the k_x momentum for the $E_+^{Mo_1}$ band (c) and E_+^{Te} band (f), indicated with solid lines in panels (a)-(b). Color bar indicates positive (negative) spin projection as blue (red) gradient.</p>	63
5.3	<p>Spin projections of the energy spectrum for the zigzag-terminated ribbon in the MoTe₂-AFM2 system in Fig. 5.1(b). Panels (a)-(b) indicate S_Y-S_Z projections when the zigzag-terminated MoTe₂ ribbon is on the AFM2 substrate. The zigzag-terminated MoTe₂ ribbon is on the AFM2 substrate with the exchange field reversed in panels (c) and (d), which is indicated by the symbol (-).</p>	67

5.4	Spin projections of the energy spectrum for armchair-terminated ribbons when on the AFM1 and AFM2 substrates as indicated. In panels (a-c) the spin projections are along S_X , in panels (d-f) the spin projections are along S_Z . The inset in each panel schematizes the propagation for the electrons for the higher energy valence edge modes (indicated with black arrows) along both armchair edges, the left and the right (note in panel (d) the inset only shows the propagation for the negative S_Z band). Insets: up (down) vertical gray arrows indicate $+k_y$ ($-k_y$) momentum; green (magenta) arrows indicate positive (negative) S_X and S_Z spin projections on the armchair edges. Color bar indicates positive (negative) spin projection as green (magenta) gradient.	69
A.1	Top and side views for relaxed structures of MoS ₂ bilayer with Mo _{imp} in the 3R phase with AB stacking. T-AB and T'-AB refers to Mo _{imp} on top of a Mo and S atom in the AB stacking, respectively. Red spheres show the Mo _{imp} in each configuration.	97
A.2	Band structures for MoS ₂ bilayers with Mo _{imp} in the 3R phase and AB stacking. The Fermi energy is set at 0 eV.	97
B.1	Projected d_{z^2} orbital component (POC) for midgap states in pristine MoTe ₂ ribbon on ferromagnetic substrate. Each circle corresponds to a Mo-atom site in the ribbon, while the heat color associated to each atom indicates the POC there. The ribbon is periodic along the x -direction so that the zigzag Mo-edge is at $y = 0$ and the zigzag Te-edge is at $y = H$, where H is the ribbon width (here $H = 40a\sqrt{3}/2$). Selected energy eigenstates have midgap energy close to Fermi level E_{F1} at the Mo-edge in (a), and close to E_{F3} at the Te-edge in (b). Both eigenstates shown here have positive k , and correspond to states with majority spin up and down along $\langle S_Z \rangle$, respectively. Fermi levels are indicated in Fig. 4.4(c-d).	99

B.2 Projected orbital component (POC) for different vacancy-configurations in MoTe₂ ribbon on a ferromagnetic substrate, and states with energies near the Fermi levels of Fig. 4.4(c)-(d). (a) A single Mo_v on the Mo-edge for $E \simeq E_{F1}$; (b) single Te_v on the Te-edge with $E \simeq E_{F2}$; (c) two Te_v on the Te-edge for $E \simeq E_{F3}$; and (d) state for single Te_v in the bulk for $E \simeq E_{F1}$. Red arrows indicate location and type of vacancy present. For Te_v, the red arrows point to the Mo-atom in the unit cell of the vacancy site, which is $(\mathbf{R}_1 + \mathbf{R}_2)/3$ away. 100

C.1 (a) Top view for a MX₂ pristine monolayer, zigzag/armchair edges are along the x/y -axis, their unit cells are showed as red rhomboid (zigzag) and cyan rectangle (armchair). N, H indicates the size of the ribbon, in this example, $N = 5$ M sites, $H = 5$ M sites, the total amount of M sites is then $N_{sites} = N \times H = 25$ M sites. (b) First BZ for the 2D monolayer (hexagonal), as well as for zigzag and armchair-terminated ribbons (rectangular). The band structure for zigzag/armchair ribbons is projected along the momentum k_x/k_y . The $X' - K - \Gamma - K' - X$ path correspond to k_x momentum projection, while the $Y - \Gamma - Y'$ path correspond to k_y momentum projection. 104

C.2 Energy spectrum for the MoTe₂ pristine armchair-terminated ribbon of size $N = 40$ (width), $H = 42$ (length) (1680 Mo sites). In panel (a) spin up, panel (b) spin down, panel (c) shows both, spin up and spin down [same legends as in panels (a) and (b) apply for panel (c)]. 105

List of Tables

3.1	Relaxed parameters for MoS ₂ pristine bilayers and Mo _{imp} bilayers, given in the order of stability. The interlayer Mo-Mo distance is given by Δ_z . For doped configurations, (*) indicates distances measured near the Mo _{imp} . Layer-gap is defined by the energy difference between the valence bulk band maximum and the conduction bulk band minimum at the Γ point.	38
5.1	Calculated effective Rashba parameters α and spin-splitting $\Delta_R(k_x)/2$ for momentum $k_x = 0.35 \pi/a$ (around the K' point) for the Mo ₁ and Te edge modes projected along the MoTe ₂ zigzag edges. The parameters are calculated for three cases, the freestanding MoTe ₂ ribbon with $\lambda_R = 0$, and the MoTe ₂ -AFM1 system when $\lambda_R = 36$ meV and $\lambda_R = 72$ meV. α is obtained through a linear fitting in the curve $\Delta_R(k_x)/2k_x = \alpha$ in Fig. 5.2(a)-(b).	65
A.1	Pseudopotentials core radii for s, p, d channels, and the pseudocore radii r_{pc} for the Mo and S atoms. All the radii are in Bohr.	96

Chapter 1

Introduction

The understanding about the behavior and manipulation of electronic degrees of freedom (DoF), such as charge, valley and spin in the diverse nature of available materials, is a fundamental task which is in constant evolution, as new materials with different electronic and structural properties continue to arise [1]. Stable and high quality two-dimensional (2D) materials have emerged to complement and add functionalities to the already available nanostructures in three-dimension (3D) (e.g., vertically stacked), quasi one-dimension (1D) (e.g., nanotubes) and quasi zero-dimension (0D) (e.g., cage molecules and quantum dots). As such, Novoselov *et al.* [2] in 2004, successfully exfoliated for the first time one atom-thick crystal from graphite: graphene, which is a semimetal conductor material that can be seen as a 2D layer compound of carbon atoms in a honeycomb (or hexagonal) arrangement highly flexible. Electrons in graphene have high mobility and always conduct electricity, so graphene can be considered as a good conductor. However, field effect transistors (FETs) based on graphene show a modest on-off resistance ratio due to the lack of a band gap. This can be a fundamental limitation in modern electronics because devices with controllable band gaps are required.

Conveniently, other 2D materials were reported in 2005 [3], satisfactorily isolated to individual crystal planes from the 3D bulk: boron nitride (BN) and transition metal dichalcogenides (TMDs), such as niobium diselenide NbSe_2 and molybdenum disulphide MoS_2 . All these exfoliated materials have diverse electronic properties, ranging from metallic (NbSe_2), semiconducting (MoS_2) to insulator (BN). It is worth mentioning that MoS_2 -based FETs have been already created in the monolayer limit [4, 5], as well as in the bilayer form [5, 6]. The common characteristic among those layered materials such as graphene, TMDs and BN, is that single layers are the building blocks of their 3D bulk. Adjacent single layers are vertically stacked and held together through weak

van der Waals (vdW) forces, while strong covalent bonds hold the atoms together in the plane.

Among these vertically stacked materials, semiconductor TMDs have received enormous scientific interest due to their numerous exciting physical properties. By means of typical synthesis procedures in the lab, such as mechanical exfoliation, chemical vapor deposition (CVD) or molecular beam epitaxy (MBE), experimental samples of TMDs can be obtained either, as a monolayer or as several number of layers, such as bilayers, trilayers, and so on [2, 7]. Those experimental samples can vary in thickness, stacking type, shapes and boundaries. For example, TMD bilayers with several stacking types [8], wide and ultranarrow nanoribbons with defined boundaries such as zigzag [9, 10] or armchair terminations [11, 12], and flakes with defined shapes such as triangles [13, 14] and snowflakes [15] have been synthesized. Depending on the growth procedure, the samples can be obtained on a substrate [8, 9, 16, 17], in pristine form (free of defects or without substrate interaction) [18, 19] or defective (with impurities, adatoms and/or vacancies, among others) [20, 21, 22, 23, 24]. Nevertheless, substrates and defects can effectively add properties and functionalities to those materials.

Given the abundant availability of experimental samples (such as the aforementioned), theoretical modeling needs to account accurately for these structures, also by considering the existence of defects/substrates. Theoretical approaches, such as density functional theory (DFT), tight-binding (TB) models and effective low-energy Hamiltonians can reliably construct and model these diverse TMD samples, allowing us to calculate their electronic energy spectra, that is, the band structure; which provide fundamental information to construct solid-state devices. Interestingly, the band structure in TMDs have a direct dependence on the number of layers: a transition from an indirect to a direct band gap occurs when the bulk is thinned to the single layer limit, making them attractive for optoelectronic applications [25, 18]. The direct band gap in the electronic spectrum of TMD monolayers ($\sim 1 - 2$ eV) is an intrinsic characteristic of the material, coming from the crystal-field splitting of the transition metal atom. TMD monolayers lack of inversion symmetry, allowing two degenerate (yet inequivalent) valleys in the momentum-space electronic band structure. The valleys called K and K' are of special interest in TMDs because the main electronic and optical properties occur therein [26, 27]. Moreover, due to the heavy metal atoms in the TMD lattice, spin-orbit coupling (SOC) arises strongly around the K and K' valleys. These properties lead to the unique physics of TMDs, such as the emergence of the spin-valley coupling phenomenon, giving unprecedented independent or simultaneous control for both, the valley and electron spin DoF [26, 27].

Another attractive property which is present in pristine multilayer TMDs such as bilayers, is the layer pseudospin DoF, associated with electrical polarization [28, 29]. Pristine TMD bilayers with several stacking types can induce modifications on the electronic and optical properties [8, 30]. The most notable changes can occur along the band edges (the valleys K , K' and Γ), giving rise to stacking-induced band structure engineering. However, to further exploit the physics of bilayers, external potentials such as strain, twisting, electric field, or doping, are necessary. In particular, experimentally doped MoS₂ bilayers increase the interlayer separation between adjacent two MoS₂ layers, which is attributed to the presence of MoS₂ nanoparticles between the individual layers [31]. By controlling the size of the nanoparticles trapped in-between, the interlayer distance and interlayer coupling of bilayer MoS₂ structures can be engineered over a wide range, resulting in different bandgap behaviors, interesting for modern electronic devices such as FETs. As the spin DoF is largely unexplored in doped MoS₂ bilayers, it is expected that their spin-polarized band structures due to the broken inversion symmetry, would result in novel and yet unexplored phenomena.

Spintronics is a branch of physics concerned with the storage and transfer of information by means of electron spins in addition to electron charge as in conventional electronics, defines the Oxford English Dictionary. In recent years, spintronics has emerged as one of the most exciting areas of condensed matter physics, partially due to the quick development of the control of low dimensional materials as previously described, which possess controllable band structures by means electrical, optical and/or magnetic external fields. Contrary to conventional electronics, nowadays spintronics allows the information to be injected, transferred and manipulated by means of the spin rather than the charge DoF, with greatly reduced energy dissipation [32, 33]. Spintronic devices exploiting the spin of electrons for information processing and storage, are a key emerging technology in modern electronics [34].

In TMDs, the charge, spin and valley DoF can be manipulated by magnetic fields from induced and/or external sources. Furthermore, the spin can be controlled by means of SOC, such as the Rashba effect [35, 36]. Induced magnetic sources on TMDs, can come from the magnetic proximity effect (MPE), which allows for the transfer or sharing of fundamental magnetic properties from a material A with magnetic properties (a substrate, for example) to a material B initially non-magnetic (e. g., a TMD), giving rise to modifications in the combined electronic states, as seen in the band structure responses. One could argue that proximity is a new way to create new “bulk 2D” materials with complex properties/behavior.

Recent experimental demonstrations for the MPE in proximitized vertical TMD

structures constructed with magnetic substrates, have measured large induced magnetic exchange fields (MEF) (9 - 20 T), and sizable valley splittings ($\simeq 2.5 - 18$ meV/T) [17, 37, 38, 39, 40]. MPE would take some advantages over applied external magnetic fields [41, 42, 43], since valley splittings can be two orders of magnitude larger than the valley splittings obtained through external magnetic fields. Furthermore, theory predicts a giant and tunable valley splitting, together with a sizable Rashba field in a 2D MoTe₂ layer when in proximity to a ferromagnetic (FM) substrate such as EuO due to the induced MEF [35, 44].

The focus of this thesis is to study the electronic and magnetic proximity properties in vertically stacked TMD-based structures, such as MoS₂ bilayers with impurity atoms in the interlayer region, and TMD nanoribbons with defined zigzag and armchair edges on magnetic substrates, the latter forming magnetic proximitized vertical heterostructures. In order to study the electronic band structures and the magnetic proximity properties in the systems, we use two different theoretical approaches: DFT and generalized TB models. Both approaches capture the relevant bands and symmetries, and allow us to reliably describe realistic TMD-based vertical structures.

In Chapter 2, we provide a general description for TMDs, by including illustrative and useful examples related to our vertical structures. We also incorporate the theoretical models and concepts used throughout the work, together with several theoretical and experimental achievements based on TMDs.

In Chapter 3, through a vdW-DF approach, we study the electronic spectrum for MoS₂ bilayers with diverse stacking orders with molybdenum Mo atoms as impurities in the interlayer region. We show that the Mo atoms are capable of changing the stacking order in the MoS₂ bilayer due to stability processes related to the crystal field for the impurity Mo atoms in the structure. Moreover, we also demonstrate that the interlayer distance and the electronic band gaps are modified in the presence of Mo impurities, as seen in the energy spectra and density of states.

In Chapter 4, we perform band structure and spin current calculations for MoTe₂ zigzag nanoribbons on a FM substrate such as EuO using a *magnetized* three-orbital tight-binding (3OTB) model. We demonstrate that zigzag edges act as 1D conducting channels that carry tunable spin currents acquired by the proximity to the magnetic substrate, even in the presence of moderate defect concentration in the sample.

In Chapter 5, employing an AFM-adapted *magnetized* 3OTB, we describe zigzag and armchair MoTe₂ nanoribbons on AFM substrates. When the ribbon is zigzag-terminated, our results show enhanced and tunable Rashba-type SOC (in comparison to the free-standing case). Armchair MoTe₂ ribbons show intriguing behavior when

on a AFM substrate, where gapped and gapless edge modes appear depending on the ribbon width, probably related to parity laws in low-dimensional systems.

Finally, in Chapter 6, we give conclusions and perspectives, including future work projects related with our work.

Chapter 2

Theoretical and Conceptual Background

Summary

This Chapter is devoted to describing TMD structures used throughout this work, as well as the theoretical framework to model it. In Section 2.1, TMDs as monolayers, finite-size structures, and bilayers are presented. Particular attention is given to the structural environment and electronic properties for each system. In Section 2.2 and 2.3 we describe the low energy Hamiltonians used in our calculations, emphasizing on how we use and modify them to model our vertical structures. Section 2.4 is a brief description of the intrinsic and extrinsic Rashba effect because both are present in our vertically stacked structures. Lastly, in Sections 2.5 and 2.6, we briefly introduce some useful concepts such as *magnetic proximity effect* and *spin current*, which are applied in our work.

2.1 Transition Metal Dichalcogenides

Transition metal dichalcogenides (TMDs or TMDCs, as alternately used in the literature) are a class of layered materials which can be experimentally obtained in the laboratory in their minimal atomically thin form, which is a 2D layer, referred as *single layer* or *monolayer*. Apart from mechanical exfoliation, other synthesis techniques used to obtain TMD samples are *bottom-up* methods, such as chemical vapor deposition (CVD) on metal substrates [45, 7], and molecular beam epitaxy (MBE) [46]. The former allows uniform and large-area sheets of TMDs, while the lower growth temper-

2.1 Transition Metal Dichalcogenides

ature typically used in MBE allows for the growth of vertical structures with minimal degradation or intermixing interaction among the different materials. From the first experimental exfoliation in 2005, the interest in TMDs has been growing rapidly.

TMDs can form a variety of materials with diverse electronic characteristics, such as metals (e.g., NbS₂, NbSe₂, TaS₂, among others) and semiconductors (e.g., MoS₂, MoTe₂, WS₂, among others). Charge density waves (CDW) were predicted in 2001 in group V dichalcogenide (e.g., NbS₂, TaS₂, NbSe₂ and TaSe₂), where CDW order coexists with superconductivity at low temperatures [47].

Concerning to the crystallographic structure of these laminated materials, TMDs crystallizes in four natural or synthetic typical phases (also referred to as polytypes in the literature), varying in stacking type and electronic properties. The phases are: 2H, 3R, 1T and 1T' (the numbers 1, 2 and 3 refer to the number of layers in each unit cell of the corresponding phase). 2H and 3R phases are more common and energetically stable than 1T and 1T' phases, which are unstable and possess metallic character. In Fig. 2.1 we present TMDs together with their typical phases. The upper panel in (b) shows the top view of TMD phases, while the lower panel shows layered TMDs have different stacking order in their vertical bulk form. The out-of-plane interaction between the layers is vdW-like coupling, while strong in-plane covalent bonds occur in each constituent layer (monolayer) of the bulk. Each monolayer is of the form X-M-X, that is a M plane in between two X planes, with formula MX₂, where M is the transition metal atom, and X is the chalcogen [X = S (sulfur), Se (selenium), Te (tellurium)] as shown in Fig. 2.1(a) top panel. Layers of MX₂ have M centers coordinated with six chalcogen ligands in a trigonal prismatic (2H and 3R phases) or octahedral (1T phase) arrangement, as shown in Fig. 2.1(c) [51, 27, 49, 50], following a hexagonal lattice of alternating chalcogen-metal-chalcogen planes as seen from above. Figure 2.1(a) also shows the position in the periodic table for the transition metal atoms, as well as for the chalcogens, which form the TMD compounds [48]. Atoms from group VI such as molybdenum (Mo) and tungsten (W) in combination with chalcogens, constitute the semiconducting TMD family. Semiconducting character for MoS₂ (one of the most studied TMD in the literature) was confirmed in 2010 [25, 18]. By optical spectroscopy techniques, the experiments revealed a crossover from an indirect to a direct-gap semiconductor in the monolayer limit. Other semiconducting TMD shows lower direct gaps, for instance, MoTe₂ \simeq 1 eV [16, 52], extending the range of direct gaps accessible in 2D semiconducting TMDs. The values of these gaps lie in the visible spectrum, important for FETs and optoelectronic devices [45, 27].

Illustrative breakthrough on TMDs are: the transition of indirect band gap in

2.1 Transition Metal Dichalcogenides

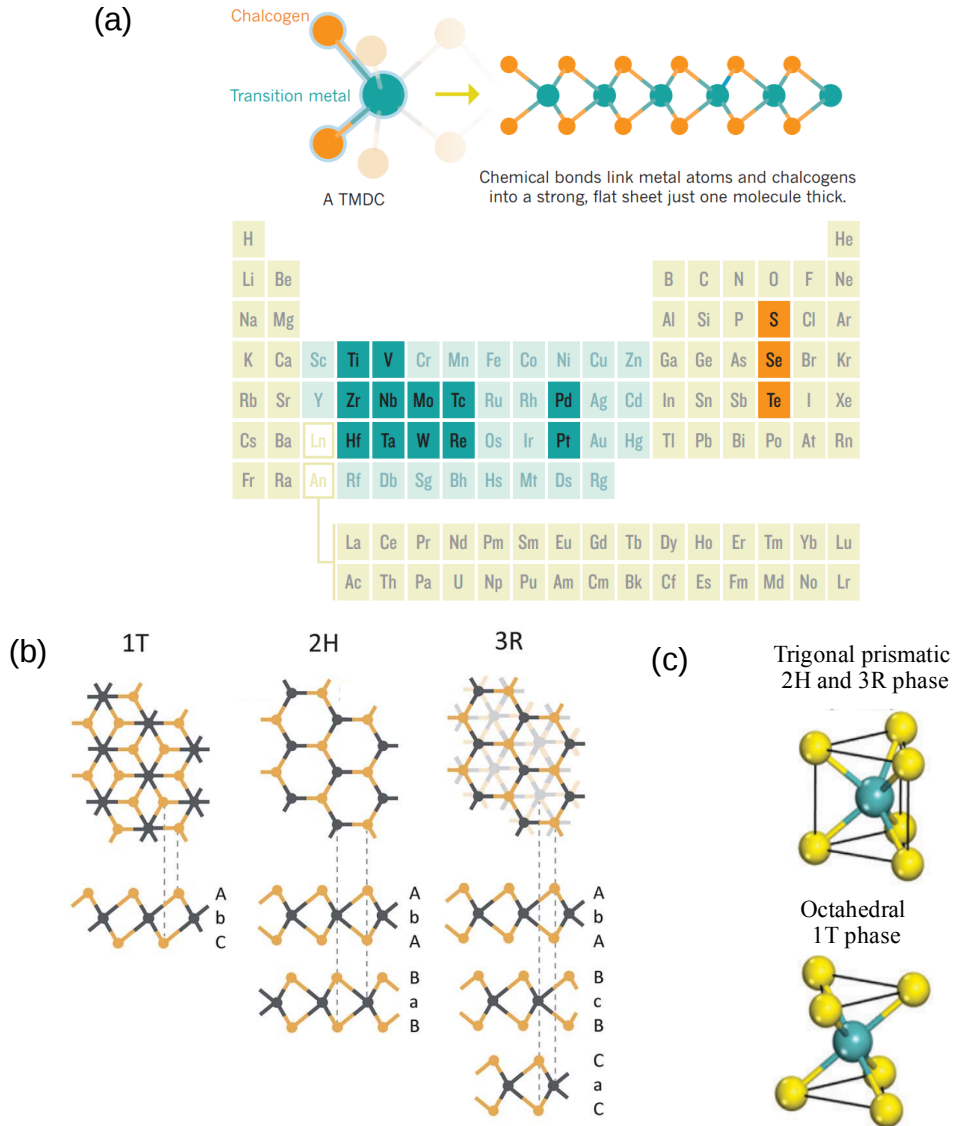


Figure 2.1: (a) A typical TMD structure, where the transition metal (dark green sphere) is sandwiched between two chalcogens (orange sphere). Transition metals are shown in dark green and chalcogens in orange in the periodic table [48]. (b) Schematic crystal structures for three typical TMD phases: 1T, 2H, and 3R, the dashed lines show how the top views and the lateral views match with each other [49]. (c) Trigonal prismatic (2H and 3R phases) and octahedral (1T phase) coordination for the metal atoms in each TMD monolayer. Yellow spheres in (c) represent the chalcogens [50].

multilayer to direct band gap in the monolayer in 2010 [25, 18]; the prediction of giant spin-orbit-induced spin splitting in 2011 [53] and observation in 2014 [54]; the

demonstration of the first single-layer MoS₂ FET in 2011 [4]; the prediction of coupled spin and valley physics in semiconducting TMD monolayers in 2012 [26]; prediction of quantum spin Hall state in distorted phases in 2014 [55] and observation in 2017 [56]; observation of WSe₂ as single photon emitters in 2015 [57]; and observation of charge density waves in twinning boundaries of MoSe₂ in 2016 [58].

Lately, research is focused on exploring the combination of different 2D materials for creating new tailored properties. TMD monolayers can be combined with either, the same TMD or different 2D or 3D materials, in such a way that lateral or vertical structures can be obtained. In this work we focus on Mo atoms in combination with either S or Te chalcogens, to build realistic vertical structures such as: (i) MoS₂ bilayers in 2H and 3R phase with several stackings, and (ii) zigzag and armchair-terminated MoTe₂ ribbons in 2H phase on FM and AFM substrates.

2.1.1 Pristine TMD Monolayers

The 2D single layer is the basic building block for TMD vertical structures, which possesses hexagonal lattice, as shown in Fig. 2.2(a). The 2D unit cell consists of a single metal atom and two chalcogens, as shown by the red rhomboid in Fig. 2.2(a). Pristine TMD monolayer possesses the D_{3h} point-group symmetry (threefold in-plane rotation symmetry and out-of-plane mirror symmetry). By taking the transition metal atom as the inversion center, the inversion symmetry is explicitly broken in-plane, because a chalcogen atom will be mapped onto an empty location [26]. On the other hand, the reflection symmetry in the z direction (σ_h) maps a chalcogen atom onto a chalcogen location, preserving the symmetry [see Fig. 2.1(c) upper panel] [59]. These general symmetry considerations determine the explicit form of the low-energy Hamiltonians [26, 59, 60, 35] which we use later in Sections 2.2 and 4.2.

In the monolayer limit, the corresponding reciprocal space is hexagonal, where the first Brillouin zone (BZ) has several symmetry k points: $\Gamma = (0, 0)$, $M = \frac{\pi}{a}(1, \frac{\sqrt{3}}{3})$, $Q_{\pm} = \pm \frac{\pi}{a}(\frac{2}{3}, 0)$, $K = \frac{\pi}{a}(\frac{4}{3}, 0)$ and $K' = \frac{\pi}{a}(-\frac{4}{3}, 0)$, as shown in Fig. 2.2(b). In 2011 Zhu *et al.* [53] predicted a large spin splitting of the energy bands along the lines $\Gamma - K$ and $\Gamma - K'$, associated to the strong SOC from the heavy transition metal atoms and from missing inversion symmetry in TMD monolayers. In presence of SOC, K and K' points are related each other by time reversal symmetry (TRS) [$E(\mathbf{k}, \uparrow) = E(-\mathbf{k}, \downarrow)$], and both valleys are fundamental symmetry points in the TMD BZ. The direct TMD energy gaps are located at the K and K' points, opening the field of light-valley interactions in 2D TMDs [18, 61]. Furthermore, strong SOC [53], spin-valley coupling and optical selection rules arise in these 2D materials [26, 27]. The consequences of the spin-valley coupling

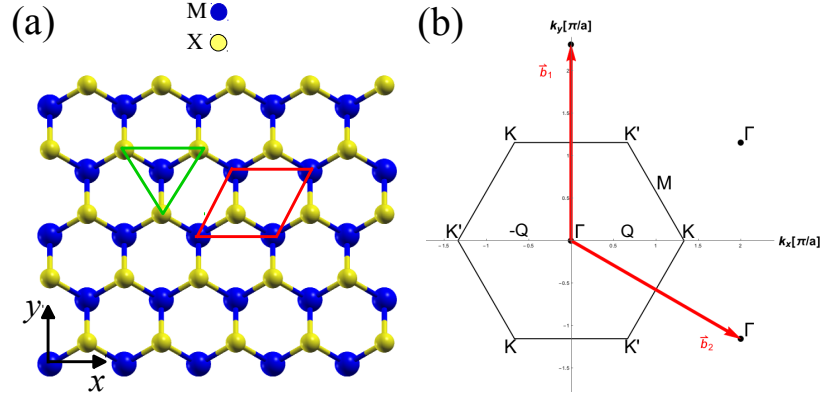


Figure 2.2: (a) Top view for the MX_2 TMD monolayer, the red rhomboid indicates the unit cell with lattice constant a (M-M distance), the green triangle stands for the trigonal prismatic coordination. Blue (yellow) spheres indicate M (X) atoms. (b) The hexagonal Brillouin zone in reciprocal 2D space with vectors \vec{b}_1 and \vec{b}_2 (red arrows). High symmetry points Γ , $\pm Q$, M , K and K' are shown.

effect are the valley Hall effect (a longitudinal electron current I drives a transverse valley current I^V) [62] and the spin Hall effect (a longitudinal electron current drives a transverse spin current I^S) [55, 33, 63] can coexist in doped regimes. Valley-dependent optical selection rules become spin dependent; that is, carriers with combination of valley and spin indices can be selectively excited by polarized optical fields [26]. The valley Hall effect was experimentally observed in a MoS_2 monolayer transistor by shining circularly polarized light onto the device [64]. Undoubtedly, all these effects have the potential to convert TMDs in a new class of electronic and optical devices by exploiting their rich physical properties.

As one can elucidate until now, the electrons in TMDs possess diverse DoF. In addition to their electric charge, valley, layer and real electron spin also are considered as DoF [29]. The valley and layer are pseudospins, the former coming from intrinsic symmetry breaking, the latter coming from the symmetry of bilayer structures. The electron spin coming from strong SOC in TMD monolayers.

In this thesis, we explore the charge and spin DoF, as we describe throughout the work.

2.1.2 Finite Size Structures

When a 2D monolayer is cut into finite structures, which is the usual experimental case, it can show regular or irregular edges. As such, nanoflakes and/or nanoribbons can be

obtained, which are good candidates for studying because quantum confinement and edge states are expected to give rise to new electronic, magnetic, transport and optical properties. TMD nanoflakes are crystals with different shapes and boundaries, and can be found when typical growth techniques such as micromechanical cleavage [3], CVD [65, 15], MBE [14] and reconstructed substrates [13] are employed. Two dimensional nanoflakes can show high crystallinity and defined edges, they can be found in a variety of forms such as triangles (MoS_2) [13, 65], rhomboids (MoS_2) [66], snowflakes (MoSe_2) [15], among others.

As nanoflakes, TMD nanoribbons with regular edges—which are usually along two high symmetry directions, the zigzag and the armchair—are of special interest because they possess fascinating 1D properties at its edges, as we describe later. Beautiful samples with atomically sharp edges can be obtained through diverse experimental techniques. By bottom-up growth procedures on prepatterned surfaces, ultranarrow (< 1 nm) or wide (≥ 3 nm) zigzag MoSe_2 ribbons are clearly observed by scanning tunneling microscopy (STM) [9]. By thermal annealing in vacuum, clean zigzag edges are seen in a MoS_2 ribbon, revealing unique Mo zigzag terminations [10]. Laser unzipping also is a versatile method for the production of high-quality nanoribbons with controllable width, edge states, and defects [67].

Concerning to the electronic properties in the TMD edges of nanoribbons, 1D metallicity has been predicted to universally occurring at the zigzag edges, related to the polar discontinuity across the zigzag direction (along the armchair direction) [68]. Chu *et al.* [69] predicted a well isolated single-edge band with strong SOC energy for the chalcogen-terminated zigzag edge, while multiple bands are found for the metal edges in semiconducting TMD ribbons. These edge bands possess strong Rashba-type SOC and are well separated from the bulk bands. Interestingly, 1D metallic edge states were experimentally revealed in MoSe_2 ribbons with zigzag edges by means spectroscopic techniques such as scanning tunneling spectroscopy [9]. Peculiar half-metallic states in MoS_2 zigzag ribbons [70] and spin currents along the MoTe_2 zigzag edges are predicted to occur when the ribbons are in close proximity to magnetic substrates [36], interesting for spintronics applications as spin filters.

Necessary for the study of the electronic structure in finite size systems, are the real and corresponding reciprocal spaces. Figure 2.3(a) shows a schematic nanoribbon representation, obtained when a 2D monolayer finite structure is synthesized, thus obtaining defined shape and edges. The unit cells are marked for zigzag- (green rhomboid) and armchair-terminated (magenta rectangle) ribbons. Panel (b) shows the corresponding rectangular BZ for zigzag and armchair-terminated ribbons, where we also show the

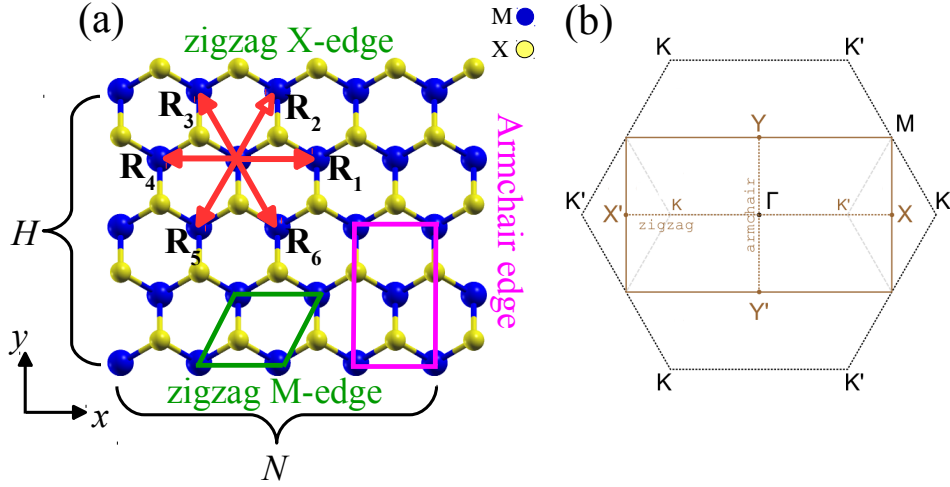


Figure 2.3: (a) Top view of a schematic 2D TMD monolayer square ribbon, with representative zigzag and armchair edges as shown. N and H are the dimensions for the ribbons when defined edges are considered. \mathbf{R}_1 through \mathbf{R}_6 are the lattice vectors connecting metal-metal (M-M) NN, shown by red arrows. Green rhomboid and magenta rectangle stand for the zigzag and armchair unit cells, respectively. (b) BZ for the 2D monolayer (black), as well as the reduced BZ for the ribbon with defined zigzag and armchair edges (brown). The high symmetry points are marked in the BZ as indicated.

hexagonal BZ of the 2D monolayer for comparison, with reciprocal symmetry points $K = \frac{\pi}{a}(\frac{4}{3}, 0)$ and $K' = \frac{\pi}{a}(-\frac{4}{3}, 0)$. For the zigzag case, the band structure is projected along the horizontal k_x -axis. One can see along the path $X' - K - \Gamma - K' - X$, the valleys K and K' are decoupled, while for the armchair case, the band projection is along the vertical k_y -axis, and K, K' points are both mapped onto $\Gamma = (0, 0)$ due to the larger unit cell for the armchair direction.

A detailed description that aims specifically to our study for armchair ribbons is in Appendix C, while zigzag ribbons are explained in Chapters 4 and 5.

2.1.3 Molybdenum Disulphide Bilayers

MoS₂ bilayers have been converted in an exciting field of research because of its intrinsic inversion symmetry and structural phases [27, 71, 72]. Interestingly, bilayers offer an unprecedented platform to realize a strong coupling between the spin, valley and layer pseudospin DoF, giving rise to the spin Hall effect and spin-dependent selection rules for optical transitions [28, 27]. Some representative experimental achievements based on MoS₂ bilayers include electrical tuning of valley magnetic moment [73], intrinsic

electronic transport properties [5], and electrical control of the valley Hall effect [74].

Unlike TMD monolayers, which lack an inversion center, bilayers with 2H phase possess an inversion center located in the middle plane between the two TMD layers, as shown in Fig. 2.1(b). TMD bilayers can crystallize more probably in 2H and 3R phases, as is demonstrated experimentally [3, 5, 75, 8, 76] and by DFT calculations [30, 49, 77]. The stacking order is an important structural characteristic in TMD bilayers as electronic transport [78], electronic and optical properties [27, 79] can be tuned. For instance, ultra flat bands at the valence band edge in twisted MoS₂ bilayers have been predicted, which are comparable to that of twisted bilayer graphene near “magic” angles [80]. The band gap size, the valence band splitting at the K points together with their relative energy with respect to Γ , and electron-hole binding energy vary with the stacking configuration in TMD bilayers [30].

In this work, we use DFT calculations to model our MoS₂ bilayers. The DFT approach is based on the idea that any property of the ground state of a system can be described as a functional of the ground state electron density, which is a function of the electron position. The functionals that can be used include the local-density approximation (LDA), generalized-gradient approximation (GGA), vdW functionals, among others. The MoS₂ bilayers we model in the next example and in Chapter 3 are based on the vdW-DF approach, this is density functional calculations with vdW-type functionals. This allows us to obtain the ground state of the systems, giving account for the vdW interactions present in the MoS₂ bilayer structures. More information about the details for the vdW-DF calculations within the SIESTA method [81] for MoS₂ bilayers can be found in Appendix A.

As a clear example of how it works vdW-DF within the SIESTA method, we have calculated the band structures for pristine bilayers with several stackings. We first consider the most stable phases of pristine MoS₂ bilayers, namely the 2H and 3R phases [82, 83, 84]. The MoS₂ layers in these natural phases have different stacking orders. The bilayer in the 2H-phase has inversion symmetry [85, 86], and shows the AA' and AB' stacking related each other by rotating the MoS₂ layers, as shown schematically in Fig. 2.4 panel (b) and (c). In AA' stacking, the hexagons in each layer are superposed in such a way that the molybdenum atoms of the bottom layer are located just below the sulfur atoms of the top layer, and vice-versa. For AB' stacking the hexagons in each layer are shifted with the sulfur atoms of the bottom layer beneath the hollow sites of top layer, and the molybdenum atoms in the top layer over the molybdenum atoms in the bottom layer [30]. In our calculations we found an energy difference between these stackings of $E_{AA'} - E_{AB'} = 2.6$ meV per atom, in good agreement with previous DFT

calculations [30, 87, 76]. The AB stacking in Fig. 2.4(a) with no rotation between the

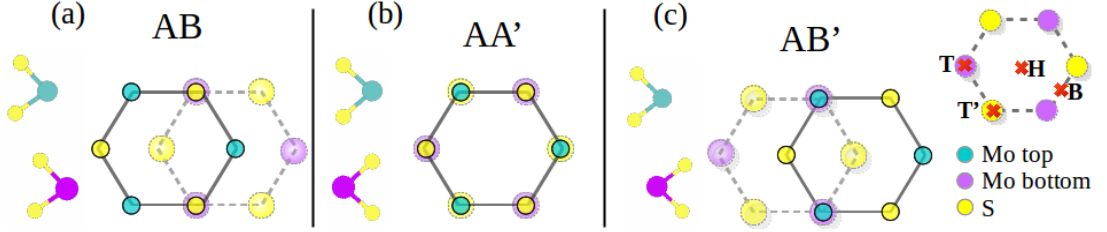


Figure 2.4: Diverse stackings for MoS₂ bilayers with low energy: (a) 3R-AB, (b) 2H-AA' and (c) 2H-AB', which refers to different stacking types in the bilayer with 2H phase. Mo atoms are shown as cyan (Mo top) and purple (Mo bottom) spheres, sulfur atoms are shown as yellow spheres. Inset shows the Mo impurity location as red crosses relative to the bottom layer in B (bridge), H (hollow), T (top over Mo) and T' (top over S).

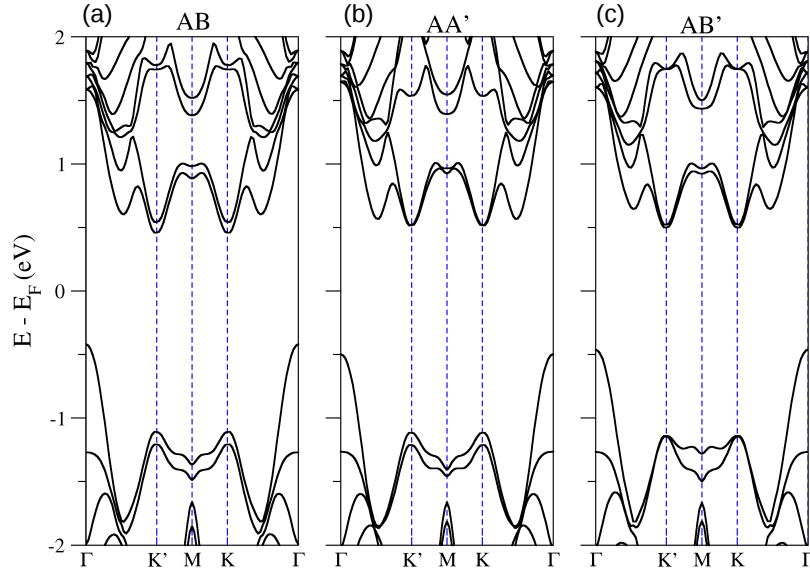


Figure 2.5: Band structures along high symmetry points in the BZ for the most stable MoS₂ pristine bilayers (in stability order in these calculations): (a) 3R-AB, (b) 2H-AA' and (c) 2H-AB'. The layer orientation for the different stackings can be seen in Fig. 2.4. The Fermi energy is set to zero eV.

two MoS₂ layers belongs to another kind of phase, the 3R-phase. The top layer slides on the bottom layer in the armchair direction so that some Mo and S atoms in different layers match.

In Fig. 2.5 we show the band structure calculations for pristine MoS₂ bilayers for the most stable stacking configurations. In panel (a), 3R-MoS₂ bilayer with AB stacking; in panel (b) and (c), 2H-MoS₂ bilayers with AA' and AB' stackings respectively, all the systems without SOC. Clearly, there is an indirect gap along the line $\Gamma - K$ for all the bilayers, as is demonstrated experimentally [88] and through other DFT calculations [6, 31]. Furthermore, the valence splitting for the AB' bilayer closes at K and K' points, while it opens for AB and AA' bilayers, indicating stacking-induced band structure changes.

In Chapter 3 we report how the stacking, the interlayer distance and the band gaps change in these MoS₂ bilayers when Mo impurities are located in the interlayer region [77]. These effects suggest that doped bilayers can add functionalities to the pristine bilayer systems.

2.2 Two-Bands $k \cdot p$ Model

The band structure near the K and K' band edges (or valleys) in semiconducting TMD monolayers can be well described through a suitable $k \cdot p$ model, introduced by Xiao *et al.* [26]. They showed that intrinsic inversion symmetry breaking together with strong SOC originated from the heavy metal d orbitals leads to coupled spin and valley physics in TMD monolayers. This combined effect is evidenced by means of a term proportional to $\lambda_v \tau s_z$ in the pristine TMD Hamiltonian, where λ_v is the strength of the SOC at the valence band ($\sim 75 - 250$ meV for different TMDs), τ is the valley index and s_z is the spin index. This simple and widely used two-bands $k \cdot p$ model is also versatile because allows one to add magnetic proximity effects [35, 44, 89], exciton effects [90], Rashba effect [59], among others to the pristine 2D TMD monolayer. This Hamiltonian has also been successfully used as a theoretical background in many experiments, where the control of the valley and spin DoF lies at the core of interest, expanding *valleytronics* and *spintronics* research.

Under the general symmetry considerations described in Subsection 2.1.1, the group of the wave vectors at the valleys is C_{3h} , and the basis functions are

$$|\phi_c\rangle = |d_{z^2}\rangle, \quad |\phi_v^\tau\rangle = \frac{1}{\sqrt{2}} \left(|d_{x^2-y^2}\rangle + i\tau |d_{xy}\rangle \right), \quad (2.1)$$

where $c(v)$ is the conduction (valence) band, $\tau = \pm 1$ is the valley index, (+) for K , (−) for K' . Approximating the SOC by intra-atomic contribution $\mathbf{L} \cdot \mathbf{S}$, the total $k \cdot p$

Hamiltonian to first order in $\mathbf{k} = (k_x, k_y)$ has the form

$$H(\mathbf{k}) = at(\tau k_x \sigma_x + k_y \sigma_y) + \frac{\Delta}{2} \sigma_z - \lambda_v \tau \frac{\sigma_z - 1}{2} s_z. \quad (2.2)$$

The first term refers to orbital interactions, the second term reflects the band gap, and the last term is the SOC-induced spin splitting in the 2D TMD lattice, which reflects the spin-valley coupling. σ_α ($\alpha = x, y, z$) are the Pauli matrices acting on the orbital pseudospin in Eq. 2.1. This Hamiltonian can be written in a 4×4 matrix form as [26, 27]

$$H(\mathbf{k}) = \begin{pmatrix} \frac{\Delta}{2} & at(\tau k_x - ik_y) & 0 & 0 \\ at(\tau k_x + ik_y) & -\frac{\Delta}{2} + \lambda_v \tau & 0 & 0 \\ 0 & 0 & \frac{\Delta}{2} & at(\tau k_x - ik_y) \\ 0 & 0 & at(\tau k_x + ik_y) & -\frac{\Delta}{2} - \lambda_v \tau \end{pmatrix}. \quad (2.3)$$

Equation 2.3 is projected to the orbital pseudospin basis of Eq. 2.1 as $\{|\phi_c, \uparrow\rangle, |\phi_v^\tau, \uparrow\rangle, |\phi_c, \downarrow\rangle, |\phi_v^\tau, \downarrow\rangle\}$, with spin $s_z = \uparrow, \downarrow$. Here the momenta k_x and k_y are measured from the K points, a is the TMD lattice constant, t is the hopping between sites, Δ is the energy gap at the K points, and $2\lambda_v$ is the spin splitting at the valence band due to SOC and inversion symmetry breaking. Because of TRS, the spin splitting is opposite at the K and K' valleys. We can note that near the valleys, the electrons in clean 2D TMD monolayers can be well described as massive Dirac fermions with strong SOC.

All the parameters can be obtained by fitting to first-principles calculations band structures in the neighborhood of K points for different TMDs. This model correctly captures the low-energy physics close to the valleys, including the SOC at the valence band, valley dependent Berry curvature, and valley dependent optical selection rules [26, 27]. To quadratic order in \mathbf{k} , electron-hole asymmetry and anisotropic dispersion (trigonal warping) in the band structure can be captured [91, 92].

More accurate approaches such as the six-band $k \cdot p$ model have been developed to account for the effective masses, Landau levels and the effective exciton g -factor in the K valleys for different TMDs [93]. The Γ [91], Q and M valleys [94] (which can be important for transport properties of hole- or electron-doped samples), as well as the spin splitting of the conduction band, are well described by effective-mass $k \cdot p$ models [94]. Real-space modifications to the TMD can also be considered in the $k \cdot p$ model, for example by deriving boundary conditions for zigzag or armchair edges [95].

In Chapter 4, we use the two-bands $k \cdot p$ model of Eq. 2.3 as starting point to construct a *magnetized* tight-binding Hamiltonian, accounting for magnetic proximity effects in 2D and finite size TMD-based vertical heterostructures.

2.3 Transition Metal Dichalcogenide Tight-Binding Hamiltonians

Unlike the $k \cdot p$ method described in the previous section, where the representation of the electronic structure for monolayer TMDs is only in the neighborhood of high symmetry points in the BZ, tight-binding (TB) models have the advantage that can reproduce the electronic band structure in the whole BZ. Tight-binding models also offer a real space description, suitable for studying finite size systems such as ribbons, flakes and quantum dots, as well as for describing defects such as vacancies, adatoms and twin grain boundaries. Tight-binding models have been constructed for TMD monolayers in various approximation levels, which depend on the number of bands involved, with multiple orbitals in the TMD unit cell. Later, we describe in more detail the three-orbital tight-binding (3OTB) Hamiltonian, which we use in Chapter 4 and 5 to model TMD ribbons. Now we briefly describe the main features of some TMD TB models reported in the literature with different number of bands and accuracy (by including the 3OTB model). In the following, the spinless cases are presented, but note that the number of bands in TMD TB models will double because of SOC.

- 3-bands TB model [60]. Contains only three M (M = Mo, W) d -orbitals $\{d_{z^2}, d_{xy}, d_{x^2-y^2}\}$. Symmetry-based M-M hoppings for nearest neighbor (NN) and M-M-M next-nearest-neighbors (NNN) interactions. This model is not Slater-Koster (SK)-like but fully based on the TMD symmetry. Accuracy around the K, K' valleys within the NN approximation, better fit is found in the entire BZ when NNN are included.
- 5-bands TB model [92]. Derived from a 7-bands TB model, contains three Mo- d orbitals and two X (X = S) p orbitals in a symmetric and antisymmetric linear combination: $\{d_{z^2}, d_{x^2-y^2} + id_{xy}, d_{x^2-y^2} - id_{xy}\}$ for the M atoms and $\{p_x + ip_y, p_x - ip_y\}$ for the X atoms. Accurate for energies around the K and K' valleys.
- 7-bands TB model [92]. Contains three Mo- d orbitals $\{d_{z^2}, d_{xy}, d_{x^2-y^2}\}$ and two chalcogen p orbitals, $\{p_x, p_y\}$ for each chalcogen atom, only Mo-X (X = S) NN

2.3 Transition Metal Dichalcogenide Tight-Binding Hamiltonians

in the SK approach for the hopping and overlap integrals are used. Accurate for energies around the K and K' valleys.

- 11-bands TB model [96, 97]. Contains all the M (M = Mo, W) d -orbitals $\{d_{z^2}, d_{x^2-y^2}, d_{xy}, d_{xz}, d_{yz}\}$ and the top (t) and bottom (b) p X orbitals (X = S) $\{p_{x,t(b)}, p_{y,t(b)}, p_{z,t(b)}\}$. NN SK hoppings of M-M, M-X, and X-X. The fitted bands agree qualitative well with the first principles band structure around the valleys, but a quantitative discrepancy can be seen away from the K and Γ points. An accurate parametrization is found for the MoS₂ band structure within the 11-bands TB model [98]. A recent improve scheme in the SK approach is found for M = Mo, W and X = S, Se, Te; which considers M-M-M and X-X-X NNN [99].
- 27-bands TB model [100]. Contains the complete set of sp^3d^5 orbitals for the Mo atom and the two chalcogen atoms. SK approach for the NN hopping and overlap integrals. Accurate for energies in the range -3 to 3 eV in the entire BZ.

2.3.1 Three-Orbital Tight-Binding Hamiltonian

The successful 3OTB Hamiltonian by Liu *et al.* [60] is fully based on symmetry considerations of the trigonal prismatic coordination of the pristine TMD monolayer. The essence behind this approach is twofold: first, exploit the fact that at low energies and near the fundamental gap, the Bloch states around the valence and conduction band edges mostly consist of three M (M = Mo, W) d -orbitals $\{d_{z^2}, d_{xy}, d_{x^2-y^2}\}$ of the transition metal atoms, which contribute the most to the electronic states for the TMD monolayers, with almost no p -orbital weight from the chalcogen atoms. Second, the crystal symmetry of 2D TMDs belongs to the D_{3h} space group, and the trigonal prismatic coordination of the metal atoms splits the d orbitals into three groups $\{d_{z^2}\}$, $\{d_{xy}, d_{x^2-y^2}\}$ and $\{d_{xz}, d_{yz}\}$. The σ_h symmetry (mirror reflection by the $x - y$ plane) allows hybridization only between $\{d_{z^2}\}$ and $\{d_{xy}, d_{x^2-y^2}\}$, leaving $\{d_{xz}, d_{yz}\}$ decoupled from the other d -orbital groups. Therefore, in the low-energy regime, it is suitable to describe 2D TMD monolayers within the d -orbital basis given by $\{d_{z^2}, d_{xy}, d_{x^2-y^2}\}$, and by only considering metal d - d hoppings in the lattice (i.e., a triangular lattice of metal atoms, as explained later).

The 3OTB model preserves the lattice symmetries and has been proved to reliably describe TMDs flakes and ribbons in diverse situations [101, 102, 103, 104]. The 3OTB model also has been used to depict twin grain boundaries in MoSe₂ 2D monolayers [105] and combined systems such as lateral [106] or vertical [36] heterostructures in real space.

2.3 Transition Metal Dichalcogenide Tight-Binding Hamiltonians

The 3OTB Hamiltonian originally is represented in continuous momentum space up to first neighbors as

$$H_0(\mathbf{k}) = \begin{pmatrix} h_0 & h_1 & h_2 \\ h_1^* & h_{11} & h_{12} \\ h_2^* & h_{12}^* & h_{22} \end{pmatrix}, \quad (2.4)$$

with basis $\{|d_{z^2}\rangle, |d_{xy}\rangle, |d_{x^2-y^2}\rangle\}$, and matrix Hamiltonian elements of the form

$$h_0 = 2t_0 (\cos 2\alpha + 2 \cos \alpha \cos \beta) + \epsilon_1, \quad (2.5a)$$

$$h_1 = -2\sqrt{3}t_2 \sin \alpha \sin \beta + 2it_1 (\sin 2\alpha + \sin \alpha \cos \beta), \quad (2.5b)$$

$$h_2 = 2t_2 (\cos 2\alpha - \cos \alpha \cos \beta) + 2\sqrt{3}it_1 \cos \alpha \sin \beta, \quad (2.5c)$$

$$h_{11} = 2t_{11} \cos 2\alpha + (t_{11} + 3t_{22}) \cos \alpha \cos \beta + \epsilon_2, \quad (2.5d)$$

$$h_{22} = 2t_{22} \cos 2\alpha + (3t_{11} + t_{22}) \cos \alpha \cos \beta + \epsilon_2, \quad (2.5e)$$

$$h_{12} = \sqrt{3} (t_{22} - t_{11}) \sin \alpha \sin \beta + 4it_{12} \sin \alpha (\cos \alpha - \cos \beta), \quad (2.5f)$$

where $\alpha = k_x a/2$ and $\beta = \sqrt{3}k_y a/2$, ϵ_1 and ϵ_2 are the onsite energies for d_{z^2} , and $(d_{xy}, d_{x^2-y^2})$ orbitals, respectively. $t_0, t_1, t_2, t_{11}, t_{22}$ and t_{12} are the symmetry based d - d metal hopping integrals. With this minimal set of parameters (eight in total), and then by fitting with DFT band structure calculations, the values for the parameters can be obtained, which are listed in Table II of Ref. [60] for all 2D TMD monolayers of group-VIB. The 3OTB model up to first neighbors in Eq. 2.4 is sufficient to describe the physics of conduction and valence bands around the valleys. Inclusion of next nearest-neighbor d - d hoppings for M atoms improves the agreement for momenta away from the valleys, especially near the Γ and M points in the valence band [60]. Note that by using Taylor expansion for the 3OTB Hamiltonian of Eq. 2.4 in the vicinity of a given wave vector (K or K') up to first order in momentum \mathbf{k} , the $k \cdot p$ model in Eq. 2.2 can be obtained, giving the expected close relation between both approaches for 2D TMD monolayers.

Spin-orbit coupling in monolayers MX_2 is due to the heavy transition metal M atoms. Within the 3OTB model, SOC is approximated by considering only the onsite contribution from the M atoms as $H_{\text{SOC}} = \lambda_v L_z S_z$, where λ_v characterizes the strength of the SOC at the valence band, L_z and S_z are the z components of the orbital and spin angular momentum, respectively.

Using the basis $\{|d_{z^2}, \uparrow\rangle, |d_{xy}, \uparrow\rangle, |d_{x^2-y^2}, \uparrow\rangle, |d_{z^2}, \downarrow\rangle, |d_{xy}, \downarrow\rangle, |d_{x^2-y^2}, \downarrow\rangle\}$ with spin

2.3 Transition Metal Dichalcogenide Tight-Binding Hamiltonians

$s_z = \uparrow, \downarrow$, the SOC contribution to the Hamiltonian is

$$H_{\text{SOC}} = \frac{\lambda_v}{2} \begin{pmatrix} L_z & 0 \\ 0 & -L_z \end{pmatrix}, \quad \text{in which} \quad L_z = \begin{pmatrix} 0 & 0 & 0 \\ 0 & 0 & 2i \\ 0 & -2i & 0 \end{pmatrix}. \quad (2.6)$$

Then, the full 3OTB Hamiltonian is written as

$$H(\mathbf{k}) = I_2 \otimes H_0(\mathbf{k}) + H_{\text{SOC}} = \begin{pmatrix} H_0(\mathbf{k}) + \frac{\lambda_v}{2} L_z & 0 \\ 0 & H_0(\mathbf{k}) - \frac{\lambda_v}{2} L_z \end{pmatrix}, \quad (2.7)$$

where I_2 is the 2×2 identity matrix. Note that the full 3OTB is block diagonal, therefore the spin z component is not mixed by the SOC. At the K, K' points in Eq. 2.7, the SOC interaction splits the valence band maximum (VBM) by $\Delta_{\text{SOC}}^v = 2\lambda_v$. The spin splitting (Δ_{SOC}^v) can be numerically fitted with DFT band structures, and the SOC coupling (λ_v) can be analytically obtained by second-order perturbation theory. Both parameters are listed in Table IV of Ref. [60] for all TMD monolayers of group-VIB.

As an instructive and useful example as we will use later in this work, we solve the 3OTB for molybdenum ditelluride MoTe_2 monolayer. By diagonalizing Eq. 2.7 and taking the MoTe_2 parameters, the band structure for the 2D MoTe_2 monolayer with SOC is obtained along high symmetry points in the first BZ, as shown in Fig. 2.6(a). Clearly, the two valleys K and K' are time-reversal related, the gap opens at the valleys and the spin splitting is seen for the valence bands due to SOC. Therefore, the 3OTB Hamiltonian is a suitable model to reproduce the low-energy spectra around the valleys in TMD monolayers as in comparison to density functional calculations [60].

2.3.1.1 Three Orbital Tight Binding Hamiltonian in Real Space

The 3OTB model also allows for a description in real space. The hexagonal lattice in the monolayer can be effectively modeled as a triangular metal M lattice, where the hoppings are only between metal atoms with multiple d -orbitals due to the symmetry of the structure. The metal atoms are connected through lattice vectors \mathbf{R} , as shown by the red arrows in Fig. 2.3(a). Up to first neighbors, the 3OTB Hamiltonian for the pristine TMD lattice in real space is

$$H_{3\text{OTB}} = H_o + H_t(\mathbf{R}_j) + H_{\text{SOC}}. \quad (2.8)$$

2.3 Transition Metal Dichalcogenide Tight-Binding Hamiltonians

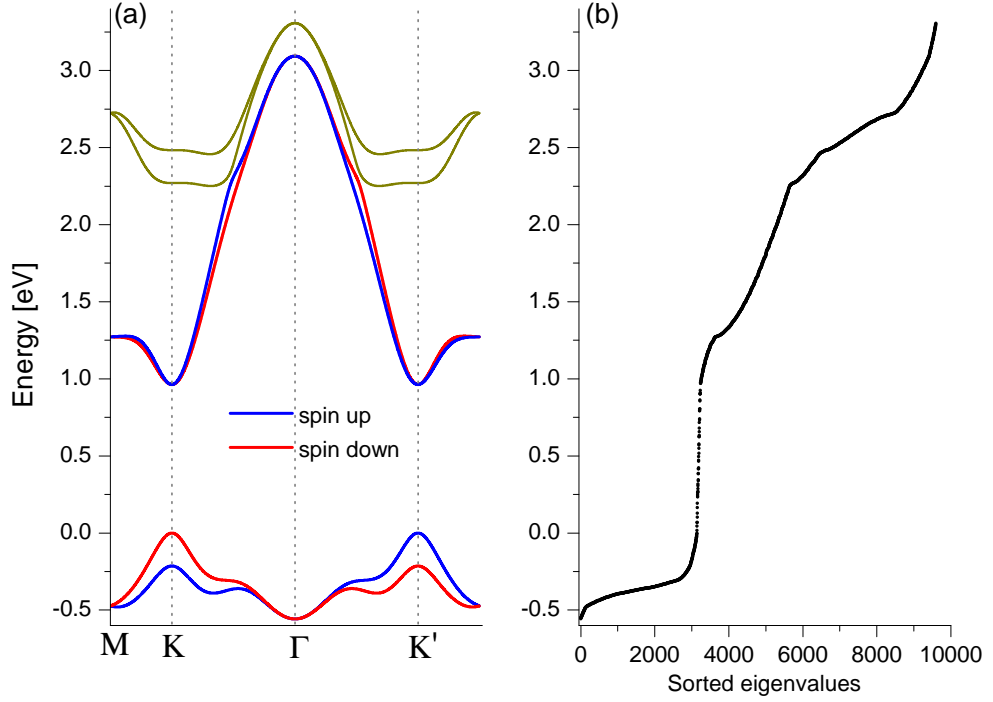


Figure 2.6: (a) Band structure within the 3OTB model for MoTe₂ 2D monolayer with SOC given by Eq. 2.7. Blue (red) colors correspond to spin up (down) conduction and valence bands, green color stand for conduction bands with higher energy. The MoTe₂ gap at the valleys is $\simeq 1$ eV, while the SOC splitting of the valence band is $\Delta_{\text{SOC}} = 0.215$ eV. The VBM is set to zero energy. (b) Discrete energy levels for a MoTe₂ square ribbon with $N_{\text{sites}} = 1600$ Mo sites, modeled with Eq. 2.8. The discrete spectrum as black dots shows midgap states with metallic character. The midgap levels are 1D-like extended states localized at the sample edges. Note that here we show the sorted eigenenergies, with the horizontal axis just listing the increasing electronic states.

The onsite TB Hamiltonian H_o can be written as

$$H_o = \sum_{\mathbf{l}}^{N_{\text{sites}}} \sum_{s_z=\uparrow,\downarrow} \sum_{\alpha,\alpha'} \epsilon_{\alpha\alpha',s_z} d_{\alpha,\mathbf{l},s_z}^\dagger d_{\alpha',\mathbf{l},s_z}, \quad (2.9)$$

where $\epsilon_{\alpha\alpha',s}$ are the onsite energies and $d_{\alpha,\mathbf{l},s_z}$ ($d_{\alpha,\mathbf{l},s_z}^\dagger$) annihilates (creates) an electron with spin- s_z in orbital $\alpha \in \{d_{z^2}, d_{xy}, d_{x^2-y^2}\}$ on site $\mathbf{l} = l_1\mathbf{R}_1 + l_2\mathbf{R}_2$, with l_1 and l_2 integers. $\mathbf{R}_1 = a(1,0)$, $\mathbf{R}_2 = a(1/2, \sqrt{3}/2)$ are lattice vectors of the triangular M lattice, with a the TMD lattice constant. In a matrix form, the onsite Hamiltonian for each metal atom (or site) is diagonal $H_o = (\epsilon_1, \epsilon_2, \epsilon_2)$.

2.3 Transition Metal Dichalcogenide Tight-Binding Hamiltonians

The NN hopping Hamiltonian H_t is given by

$$H_t(\mathbf{R}_j) = \sum_{\mathbf{l}, \mathbf{R}_j} \sum_{s_z=\uparrow, \downarrow} \sum_{\alpha, \alpha'} t_{\alpha\alpha'}^{(\mathbf{R}_j)} d_{\alpha, \mathbf{l}, s}^\dagger d_{\alpha', \mathbf{l}+\mathbf{R}_j, s} + \text{H.c.}, \quad (2.10)$$

where $t_{\alpha\alpha'}^{(\mathbf{R}_j)}$ are hopping parameters in three different directions, \mathbf{R}_j , $j = 1, 2, 3$, with $\mathbf{R}_3 = \mathbf{R}_2 - \mathbf{R}_1$. Starting along the \mathbf{R}_1 direction [see Fig. 2.3(a)], there are nine allowed hoppings, which are written in a 3×3 matrix form as

$$H_t(\mathbf{R}_1) = \begin{pmatrix} t_0 & t_1 & t_2 \\ -t_1 & t_{11} & t_{12} \\ t_2 & -t_{12} & t_{22} \end{pmatrix} = H_t(\mathbf{R}_4)^T. \quad (2.11)$$

Along direction \mathbf{R}_5 , the hopping Hamiltonian is constructed by considering the rotation by $2\pi/3$ around the z axis as

$$H_t(\mathbf{R}_5) = \begin{pmatrix} t_0 & \frac{1}{2}t_1 + \frac{\sqrt{3}}{2}t_2 & \frac{\sqrt{3}}{2}t_1 - \frac{1}{2}t_2 \\ -\frac{1}{2}t_1 + \frac{\sqrt{3}}{2}t_2 & \frac{1}{4}t_{11} + \frac{3}{4}t_{22} & \frac{\sqrt{3}}{4}t_{11} - t_{12} - \frac{\sqrt{3}}{4}t_{22} \\ -\frac{\sqrt{3}}{2}t_1 - \frac{1}{2}t_2 & \frac{\sqrt{3}}{4}t_{11} + t_{12} - \frac{\sqrt{3}}{4}t_{22} & \frac{3}{4}t_{11} + \frac{1}{4}t_{22} \end{pmatrix} = H_t(\mathbf{R}_2)^T, \quad (2.12)$$

and in a similar way for the \mathbf{R}_3 (and \mathbf{R}_6) direction (see e.g., Eqs. (4-6) from Ref. [101]). The SOC Hamiltonian H_{SOC} is the same as the one described in Eq. 2.6. Then, due to the symmetry of the system, the total amount of parameters is reduced to two onsite energies and six hoppings for the TMD monolayers, which can be taken from Ref. [60].

The 3OTB model in real space described above also allows for finite size systems description through appropriate treatment of periodic boundary conditions (PBC) along the symmetry directions of the structures, by modelling e.g., periodic nanoribbons. As we described in Subsection 2.1.2, when a 2D monolayer is cut into finite structures, it can show regular or irregular edges, the regular edges are usually along two high symmetry directions, the zigzag and the armchair. Figure 2.3(a) shows a 2D monolayer where the zigzag edges are along the x direction, while the armchair edges are along the y direction. Taking a MoTe₂ ribbon with zigzag edges as an example, their energy spectrum is shown in Fig. 2.6(b). Here the eigenenergies are fully discrete, exhibiting both bulk- and edge-like states. Comparing the continuous and discrete electronic spectrum in panels (a) and (b) of Fig. 2.6, one can see that the edge-like states lie in the MoTe₂ 2D bulk gap, between zero and $\simeq 1$ eV, signaling 1D-like extended states localized near the borders of the sample. These midgap states have metallic character and are strongly localized along the zigzag edges of the ribbon [69, 9].

Later in Chapters 4 and 5, we construct TMD nanoribbons with zigzag and armchair terminations when they are placed onto FM and AFM substrates, by augmenting the pristine TMD 3OTB Hamiltonian in Eq. 2.8 by exchange and Rashba fields. The edge states are expected to have a deep impact on the properties of the magnetic proximitized nanoribbons, especially for the electron spin DoF.

2.4 Rashba Spin Orbit Coupling in a 2D Electron Gas

In our work, we deal with two kinds of Rashba interactions, where each one of them has different origin and meaning. Then, it becomes necessary to elucidate the different physical meaning of: (i) the Rashba-type SOC (with strength α), coming from broken lattice symmetry in the crystal, e.g., at the zigzag edges of TMD ribbons [69, 107], and (ii) the extrinsic Rashba field (with strength λ_R) coming from an interface field generated by the proximity interaction with a substrate, for example [108, 109, 110, 59, 35, 111, 36]. We will start by defining the Rashba-type SOC α in a 2D electron gas (2DEG), then for a 1D electron gas (1DEG) Rashba systems, which applies for the zigzag edges of TMD ribbons. Then, we will apply the analysis to the extrinsic Rashba field λ_R .

The basic requirements for Rashba systems are uniaxial symmetry and absence of inversion symmetry [112]. Whenever these conditions are fulfilled, Rashba-type SOC contributes to the electron Hamiltonian as $H_R = \alpha(\mathbf{s} \times \mathbf{k}) \cdot \hat{\mathbf{e}}_z$, where $\mathbf{s} = (s_x, s_y, s_z)$ are the Pauli matrices associated with the real spin and $\hat{\mathbf{e}}_z$ is a unit vector along the symmetry axis, associated with an electric field perpendicular to the 2D momentum $\mathbf{k} = (k_x, k_y)$ [113, 114, 109]. The Rashba term in 2D homogeneous lattices locks electron spin \mathbf{s} to momentum \mathbf{k} [109, 112], and can be written as a Bychkov-Rashba Hamiltonian of the form [113, 112, 33, 115]

$$H_R = \alpha(s_x k_y - s_y k_x). \quad (2.13)$$

The effective single-particle Hamiltonian for 2D electrons with the Rashba term (Eq. 2.13) is then

$$H_R^{2D} = \frac{\hbar^2 \mathbf{k}^2}{2m^*} \otimes \mathbf{I}_s + \alpha(s_x k_y - s_y k_x), \quad (2.14)$$

where \hbar is the Planck's constant, \otimes denotes the tensor product of two operators acting in the orbital (H_O)– and spin Hilbert space (H_s). \mathbf{I}_s is the unit operator in the spin space ($s_z = \uparrow, \downarrow$), and m^* is the effective electron mass. This Hamiltonian commutes with the momentum operator $\hat{\mathbf{p}}$ and time-reversal operator (\hat{T}) [114]. Its eigenenergies

2.4 Rashba Spin Orbit Coupling in a 2D Electron Gas

are $E_\lambda(\mathbf{k}) = \hbar^2 \mathbf{k}^2 / 2m^* \pm \alpha |\mathbf{k}|$, which are labeled by the 2D momentum \mathbf{k} and the chirality eigenvalues $\lambda = \pm 1$. Because \mathbf{k} enters into H_R linearly, in a lower order than into the kinetic energy $\hbar^2 \mathbf{k}^2 / 2m^*$, the topology of the energy spectrum changes. There appear two $E(\mathbf{k})$ parabolic surfaces with a self-crossing conical (Dirac) point at $\mathbf{k} = 0$, as shown in Fig. 2.7(a) [112]. The corresponding eigenstates for the Rashba Hamiltonian in Eq. 2.14 are

$$\psi_{\mathbf{k},\pm} = \frac{1}{\sqrt{2}} \begin{pmatrix} 1 \\ \mp i e^{i\theta} \end{pmatrix}, \quad (2.15)$$

where θ is defined as $\theta = \tan^{-1} \left(\frac{k_y}{k_x} \right)$. Due to TRS invariance $[\hat{H}, \hat{T}] = 0$, the two eigenstates of opposite momenta and spins are degenerate. The expectation value of the spin operator $\mathbf{S} = \hbar \mathbf{s} / 2$ projected in the eigenstates Eq. 2.15 are

$$\langle \psi_{\mathbf{k},\pm} | s_x | \psi_{\mathbf{k},\pm} \rangle = \pm \frac{k_y}{|\mathbf{k}|}, \quad (2.16a)$$

$$\langle \psi_{\mathbf{k},\pm} | s_y | \psi_{\mathbf{k},\pm} \rangle = \mp \frac{k_x}{|\mathbf{k}|}, \quad (2.16b)$$

$$\langle \psi_{\mathbf{k},\pm} | s_z | \psi_{\mathbf{k},\pm} \rangle = 0, \quad (2.16c)$$

which can be written in a compact form as

$$\langle \psi_{\mathbf{k},\pm} | \mathbf{s} | \psi_{\mathbf{k},\pm} \rangle = \pm \frac{k_y}{|\mathbf{k}|} \hat{\mathbf{x}} \mp \frac{k_x}{|\mathbf{k}|} \hat{\mathbf{y}}, \quad (2.17)$$

where $\hat{\mathbf{x}}$ and $\hat{\mathbf{y}}$ are the unit vectors within the xy -plane of the 2D crystal. Equation 2.17 demonstrates that no common spin quantization axis can be found for all eigenstates of a 2D Rashba system.

2.4.1 Rashba Spin Orbit Coupling in a 1D Electron Gas

In a 1D Rashba system with unit vector $\hat{\mathbf{e}}_z$, the Rashba Hamiltonian in Eq. 2.14 reduces to

$$H_R^{1D}(k_x) = \frac{\hbar^2 k_x^2}{2m^*} - \alpha k_x s_y. \quad (2.18)$$

Its eigenvalues, which define the 1D energy-momentum dispersion are $E_\lambda(k_x) = \hbar^2 k^2 / 2m^* \pm \alpha |k_x|$, with the corresponding eigenvectors

$$\psi_{k_x,\pm} = \frac{1}{\sqrt{2}} \begin{pmatrix} 1 \\ \mp i \frac{k_x}{|k_x|} \end{pmatrix}. \quad (2.19)$$

2.4 Rashba Spin Orbit Coupling in a 2D Electron Gas

As in the 2D case, the eigenstates in 1D Rashba systems are labeled by the momentum operator eigenvalue $\hbar k_x$ and the chirality operator eigenvalue $\lambda = \pm 1$. The expectation value of the spin operator is then,

$$\langle \psi_{k_x, \pm} | s_y | \psi_{k_x, \pm} \rangle = \mp \frac{k_x}{|k_x|}. \quad (2.20)$$

From Eq. 2.20 we see that the y -component of spin in the eigenstate $|\psi_{k_x, \lambda}\rangle$ is \uparrow for $\lambda = 1$ and $k_x < 0$, and is \downarrow for $\lambda = 1$ and $k_x > 0$; the opposite is true for the other branch $[E_{\lambda=-1}(k_x)]$, as is shown in Fig. 2.7(d). Equation 2.20 means that each spin-split parabolic subband has a well-defined spin. Thus, the eigenvalues of spin s_y are good quantum numbers because in 1D, s_y commutes with the Hamiltonian in Eq. 2.18 $[H_R^{1D}, s_y] = 0$. Following the analysis above, it is straightforward to understand the relative spin orientations of the states along each of the dispersions branches for Rashba systems, where a SO induced-Rashba spin splitting arises [113, 116, 117, 114].

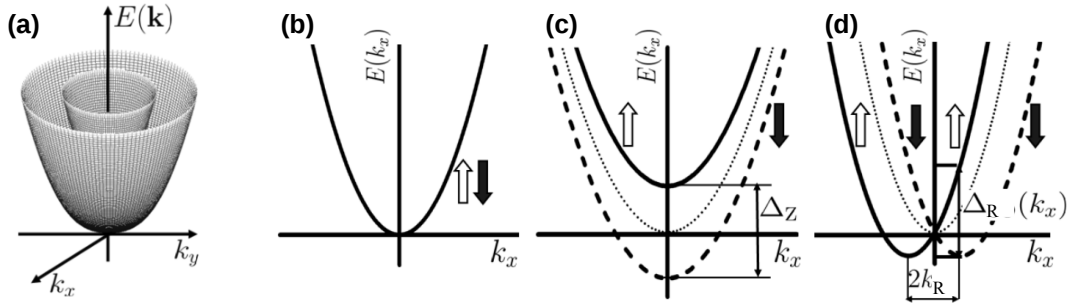


Figure 2.7: (a) The energy-momentum dispersion $E(k_x, k_y)$ of the Rashba spin-split 2DEG. The states at the Fermi level lie on two concentric Fermi circles, $E_+(\mathbf{k}) = E_F$ for the inner circle and $E_-(\mathbf{k}) = E_F$ for the outer circle. The 1D energy-momentum dispersion for: (b) infinite clean 1DEG, (c) 1DEG in magnetic field with Zeeman splitting Δ_Z , and (d) 1DEG with Rashba-type SOC. The SO-induced spin splitting in (d) is significant by the energy separation Δ_R at a given k_x , k_R is the Rashba momentum associated to the Rashba-type SOC [114].

It is important to note the difference between the familiar Zeeman spin-splitting (Δ_Z) [Fig. 2.7(c)] and the Rashba-type spin-splitting (Δ_R) [Fig. 2.7(d)] in 1DEG systems. In the case of Zeeman splitting –when a magnetic field is present in the system– the spin- \uparrow and spin- \downarrow subbands are shifted vertically with respect to each other by a Zeeman energy $\Delta_Z \propto \mu_B B$, with μ_B the Bohr magneton and B the momentum-independent magnetic field. As one can infer from the single-particle energies in 1D Rashba systems $E_\lambda(k_x) = \hbar^2 k^2 / 2m^* \pm \alpha |k_x|$, the Rashba spin-splitting depends linearly

on momentum as

$$\Delta_{\text{R}}(k_x) = E_+(k_x) - E_-(k_x) = 2\alpha|k_x|, \quad (2.21)$$

then, when the energy dispersion is projected along a single momentum direction (k_x in this case), the branches $E_+(k_x)$ and $E_-(k_x)$ are shifted horizontally along the momentum axis rather than along the energy axis (as in the Zeeman case). Diverse experiments such as angle-resolved photoemission [118, 109, 119] and optical spectroscopy [120] probe either, Δ_{R} or the Rashba SO momentum associated k_{R} .

2.4.2 Extrinsic Rashba field

If the inversion symmetry is explicitly broken in 2D monolayers, by the interaction with a substrate for example, then an extrinsic Rashba field λ_{R} , arise [108, 109, 110, 59, 35]. The Hamiltonian term manifesting the extrinsic Rashba field has been written in a modified Bychkov-Rashba [113] form

$$H_{\text{R}} = \lambda_{\text{R}}(\tau\sigma_x s_y - \sigma_y s_x), \quad (2.22)$$

here τ is the valley index, σ_{β} and s_{β} ($\beta = 0, x, y, z$) are the Pauli matrices acting on the orbital space and real spin space, respectively. Contrary to the conventional Rashba-type SOC observed in materials with absence of inversion symmetry and uniaxial symmetry (see Eq. 2.13), the extrinsic Rashba field can be considered as a modified Rashba term in the low-energy Hamiltonians, accounting for the valley DoF seen in hexagonal 2D monolayers with broken lattice symmetry. Diverse works which include the extrinsic Rashba field in their models are based on proximity-induced interactions effects coming from substrates or vertically stacked structures. If the materials break inversion symmetry, a Rashba field of the form Eq. 2.22 effectively can arise [108, 35, 111, 36]. The possibility of positioning crystals in very close proximity to one another allows for the study of additional electronic effects such as the Rashba field. In general terms, the Rashba field can produce canted spin projections when acting on 2D hexagonal materials. The canted spins projections can be manifested in magnetic proximitized systems, as we show in Chapter 4 and 5 for MoTe₂ ribbons deposited on FM and AFM substrates.

2.5 Magnetic Proximity Effects

The proximity effect refers to the influence that an ordered state (i.e., superconductivity or magnetism) has on a nearby material [121]. Lately, the proximity effect term has

been applied to also include proximity-induced SOC and/or topological properties in vertical heterostructures. For instance, a TMD monolayer can effectively transfer SOC to a graphene monolayer [122] and bilayer [104]. Protected edge states in graphene flakes with defined edges on TMDs are seen in the energy spectrum, which carries *pure spin currents* [111].

In the case of the magnetic proximity effect, a magnetization from a ferromagnet penetrates a neighboring nonmagnetic region, effectively inducing magnetism. Nowadays, 2D layers of vdW materials are widely used as the nonmagnetic region due to the successful combination with magnetic substrates, forming vertical heterostructures [123, 124, 125, 17, 37, 39, 40]. This has opened interesting possibilities to exploit material properties and create novel functionalities [32, 126].

Interactions between spins in a non-magnetic material and those from a FM or AFM crystal in close proximity have expanded spintronics research [127]. The interactions may be due to non-vanishing wave-function overlap of localized moments in the magnetic crystal with electrons in a 2D layer [128, 129, 130]. The first 2D obvious candidate for study magnetic proximity-induced interactions was graphene, where a spin splitting of 5 meV was predicted when graphene was deposited on an insulating FM EuO substrate [129, 131], motivating the successful epitaxial growth of EuO on graphene [123, 132]. Experiments with different FM substrates have reported magnetic exchange fields (MEF) induced on graphene of ~ 14 T (when on EuS) [124], and ~ 0.2 T (on YIG) [125]. Magnetic-proximitized interactions clearly allow for the effective control of the spin DoF in 2D materials, a fundamental element in spintronic devices.

Contrary to graphene, semiconducting TMDs possess a sizable band gap and intrinsic spin valley coupling due to SOC and broken inversion symmetry, allowing extra couplings when TMDs are in proximity to other materials. TMD valleytronics applications require the lifting of valley degeneracy, which has been achieved only by the application of large magnetic fields [121], so that magnetic proximity effects may provide more practical alternatives [17, 37]. Indeed, proximity effects on TMD monolayers when on a FM insulator substrate [35, 133, 134, 89, 135, 130, 38] are predicted to lift valley degeneracy due to broken time reversal symmetry and exchange fields [35, 44, 134]. Experiments found a few meV valley splitting in a WSe₂ monolayer on a EuS FM substrate [17]. WSe₂ on another FM substrate, CrI₃, [37, 38] was found to exhibit a slightly larger valley splitting ($\simeq 3.5$ meV). A giant splitting of 300 meV, equivalent to a magnetic field of 3000 T was predicted for a MoTe₂ monolayer on EuO [35, 44], together with a sizable Rashba field ($\lesssim 100$ meV). Moreover, the manipulation of excitons has been proposed in the same heterostructure by rotating the magnetization of

the substrate [90].

Magnetic proximity interactions from AFM crystals have been less explored than the FM case. Only a few theoretical works report proximity effects considering AFM substrates and TMDs [135, 130, 136]. However, it is predicted that Mn-based compounds such as manganese chalcogenophosphates MnPX_3 ($X = \text{S}, \text{Se}$) may have an AFM order commensurate with their hexagonal unit cell in the monolayer limit, which couples to the valley DoF [137]. This is an important fact because AFM order would be active in the monolayer limit, allowing AFM proximity effects in vdW heterostructures with honeycomb lattices.

A nearly unexplored field is related with the behavior for electrons in magnetic proximitized finite-size samples with defined edges in the nonmagnetic region, as those experimentally available and described in Section 2.1.2. The results we will describe in Chapter 4 reveal electrons acquires out-of-plane as well as in-plane spin polarization when a MoTe_2 zigzag ribbon is in proximity to a EuO substrate. The electronic states lie in the 2D bulk energy gap and they are extended along the zigzag edges of the finite-size system. By turning on an electrostatic gate in the combined system, tunable spin-polarized edge currents are predicted to occur due to the proximity to the EuO substrate. Additionally, different and intriguing effects such as augmented Rashba parameters and *pseudohelical* edge states that carry pure spin currents are predicted in zigzag and armchair-terminated MoTe_2 -AFM hybrids, respectively, as we will explain in Chapter 5.

2.6 Spin Currents

The flow and control of electron spin rather than the electron charge was first proposed by the seminal Datta and Das spin field-effect transistor (SFET) in narrow-gap semiconductors, arguing that a current modulation arises from spin precession due to SOC in the structure [138]. The SFET of Datta and Das consist of FM electrodes as spin injector and spin detector, source and drain respectively, and a narrow-gap semiconductor as the central channel, where the spins precess due to SOC. The SOC-induced spin precession is of the form of the Rashba Hamiltonian term in 2D systems [Eq. 2.13], which can come from intrinsic sources, such as broken inversion symmetry, as explained in Section 2.4. Interestingly, the spin-dependent device (SFET) operations do not depend on external magnetic fields, but on an electrode (gate bias), which control the spin precession rate [32].

Spintronic devices promise enhanced performance over conventional electronics by

simultaneously exploiting the flow of electric charge and the magnetic moment (spin) in a material [139, 140]. Spin-based electronic devices such as transistors (SFET for example) require spin currents, just as conventional electronic devices require charge currents [139]. Spin currents have the advantage that they can be *pure*, that is, the flow of spin angular momentum is not accompanied by any net charge transport, allowing more efficient transfer information, as schematically shown in Fig. 2.8(c). In traditional electronic circuits, electrons propagate with an equal number of spin up and spin down along the same direction, so that the total charge current in that direction $I = I^\uparrow + I^\downarrow$ is spin unpolarized, as shown in Fig. 2.8(a). Spin currents are substantially different from the more familiar charge currents because spin currents transport a vector quantity. On the other hand, spin-polarized charge currents also are different from pure spin currents because they transport charge and can be accompanied by a net spin current, as shown in Fig. 2.8(b) [114]. Generating spin currents have converted in an emergent topic in

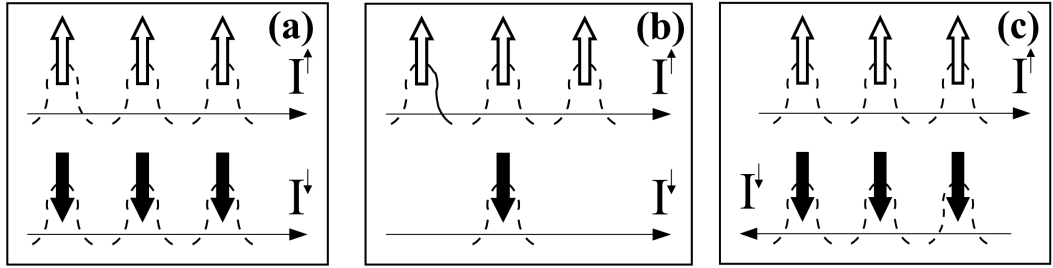


Figure 2.8: The classification of spin I^S and charge I currents in metal and semiconductor spintronic systems corresponding to spatial propagation of spin up (white arrows) and spin down (black arrows) electronic wave packets carrying spin-resolved currents I^\uparrow and I^\downarrow : (a) conventional charge current $I = I^\uparrow + I^\downarrow \neq 0$ is spin-unpolarized $I^S = \frac{\hbar}{2e}(I^\uparrow - I^\downarrow) \equiv 0$; (b) spin-polarized charge current $I \neq 0$ is accompanied also by spin current $I^S \neq 0$; and (c) *pure* spin current $I^S = \frac{\hbar}{2e}(I^\uparrow - I^\downarrow) \neq 0$ arising when spin up electrons move in one direction, while an equal number of spin down electrons move in the opposite direction, so that total charge current is $I \equiv 0$ [114].

spintronics field since the prediction of dissipationless spin currents in 2004 [33]. In a 2D system with substantial Rashba-type SOC due to structure inversion asymmetry, spin currents are intrinsic and always accompany charge currents [141, 33].

The novel spin currents we will describe in Chapter 4 follow the Bloch equation of spin-1/2 particle for eigenstates in a Rashba-type SOC system [33], such as zigzag-terminated TMD ribbons. The spin currents along the zigzag edges of a TMD ribbon (MoTe_2) acquire external Rashba and exchange fields from a FM substrate (EuO) due

to the induced MEF, and they are polarized both, in-plane as well as out-of-plane, where the former case is due to the extrinsic Rashba field as in Eq. 2.22, and the latter is due to the competition of intrinsic SOC and exchange field. Our finite-size MoTe₂-EuO combined system complements recent spin current experiments on devices containing EuO and/or 2D materials [142, 143, 144], bringing TMDs to this exciting area.

Chapter 3

Stacking Change in MoS₂ Bilayers Induced by Interstitial Molybdenum Impurities

Summary

In this Chapter, we use the vdW-DF approach to reveal the electronic and structural properties of molybdenum impurities between MoS₂ bilayers. We find that interstitial Mo impurities are able to reverse the well-known stability order of the pristine bilayer, because the most stable form of stacking changes from AA' (undoped) into AB' (doped). The occurrence of Mo impurities in different positions shows their split electronic levels in the energy gap, following octahedral and tetrahedral crystal fields. The energy stability is related to the accommodation of Mo impurities compacted in hollow sites between layers. Other less stable configurations for Mo dopants have larger interlayer distances and band gaps than those for the most stable stacking. Our findings suggest possible applications such as exciton trapping in layers around impurities and the control of bilayer stacking by Mo impurities in the growth process.

This part of the work was done in collaboration with Dr. Jhon González and Dr. Andrés Ayuela from Donostia International Physics Center (DIPC), San Sebastián, Spain. A report of these results is published in Ref. [77].

3.1 MoS₂ bilayers with Mo Impurities

The MoS₂ bilayer systems are described by using density functional of vdW (vdW-DF) calculations within the SIESTA method [81]. To include impurities, the structures of the MoS₂ bilayers were extended to a 3×3 MoS₂ supercell, using PBC. We are dealing with a diluted regime corresponding to one impurity every 54 atoms in the unit cell, around 2% doping reasonable in experimental setups [23]. Further technical details are included in Appendix A.

Our results for the stability order of the pristine bilayers show that the stacking AB is the most stable nearly degenerated with the AA' stacking at a total energy of 0.7 meV per atom, followed by the AB' stacking with 3.3 meV per atom. Note that depending on the details of different calculations the ground energy stacking can exchanging between AB and AA' [145], and the AB' stacking remains as the third state in stability. [145, 30, 87, 76].

We then include Mo atoms as intrinsic impurities within the interlayer region for MoS₂ bilayers at different inequivalent positions, as shown in Fig. 2.4. The Mo impurity is labeled as Mo_{imp}. The initial absorption sites for Mo_{imp} within the MoS₂ bilayer are assumed to follow Mo absorption sites as in MoS₂ monolayers [146, 147]. The Mo impurity position is then labeled relative to the bottom layer in B (bridge), H (hollow), T (top over Mo) and T' (top over S). The MoS₂ bilayer structures with the impurity in the interlayer region are fully relaxed, to allow the optimized lattice parameters and atomic coordinates to be obtained. More detailed information on the relaxed geometries is included in Appendix A. The binding energy can then be calculated using $E_{\text{binding}} = E_{\text{Total}} - E_{\text{bilayer}} - E_{\text{imp}}$, where E_{Total} is the total energy of the MoS₂ bilayer with the impurity, E_{bilayer} is the energy of the corresponding final pristine MoS₂ bilayer (either AA' or AB'), and E_{imp} is the energy for the isolated Mo_{imp} atom.

3.1.1 Energy and Geometry

Because the most stable configuration with Mo_{imp} belongs to the 2H-phase, here we discuss the impurity properties between bilayers focusing on the AA' and AB' stacking. The discussion on the 3R-phase is in Appendix A.

Figure 3.1 shows the total and binding energies for the different 2H stacking and impurity positions. The binding energies are negative, which indicates that the Mo impurity atoms are indeed adsorbed in the interlayer region of the MoS₂ bilayer. The binding and total energies exhibit the same trend in terms of stability. The results in increasing order of stability shows that in the presence of the interlayer Mo_{imp}, the

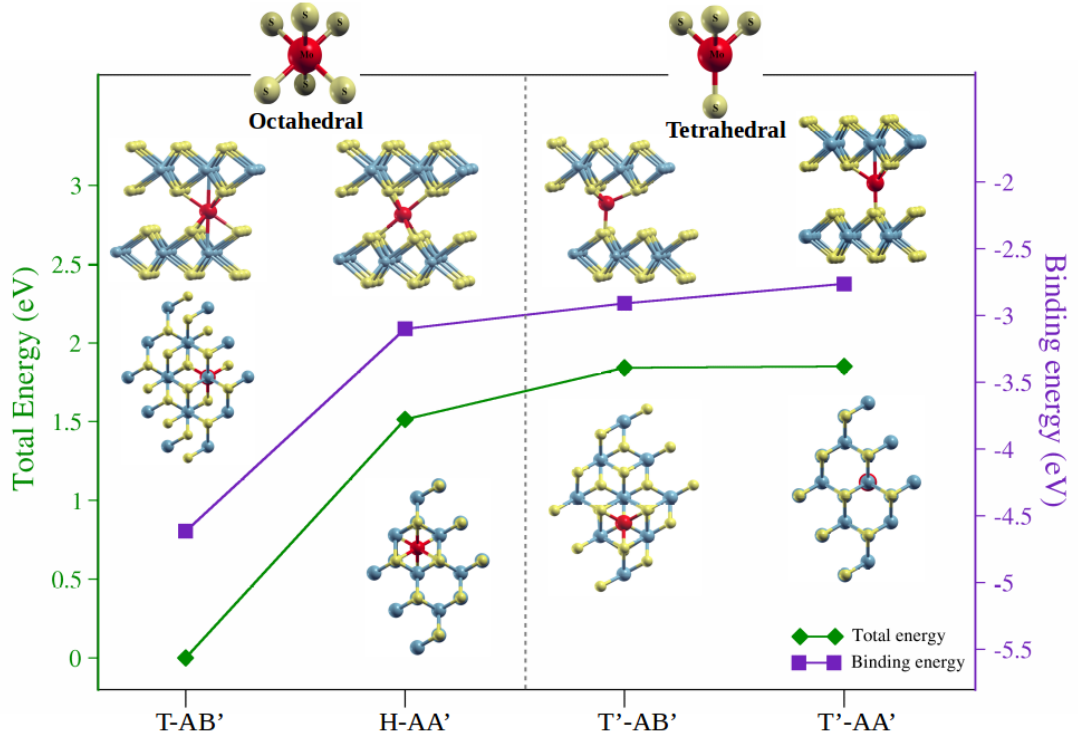


Figure 3.1: Total and binding energy as a function of the structural configurations of Mo impurities within the MoS₂ bilayer. The red spheres indicate the Mo impurity in each configuration. The relaxed structures are included, grouped in octahedral (T-AB' and H-AA') and tetrahedral (T'-AB' and T'-AA') structures of sulfur atoms around Mo impurities. The zero energy point is set for the most energetically favorable structure, namely, the T-AB' configuration. The top insets show the octahedral and tetrahedral configurations for the Mo_{imp} atom, and the relaxed side and top views structures are given for each configuration.

T-AB' bilayer configuration is the most energetically favorable. This configuration has AB' stacking with the Mo_{imp} superposed with two Mo atoms as seen from above. Note that the T-AB' configuration is reached from the input that has the Mo_{imp} placed at the bridge (B) position in the AA' stacking.

The next most favorable configuration is H-AA', with the Mo_{imp} in the hollow position, in which the bilayer structure maintains the AA' stacking. The H-AA' case is less stable than T-AB' by about 1.5 eV. On the right hand side, the configurations labeled T'-AB' for AB' stacking and T'-AA' for AA' stacking are energetically close, and the least stable.

We classify the relaxed configurations according to how the Mo_{imp} is related struc-

turally to its neighboring sulfur atoms [148, 149]. The T-AB' and H-AA' configurations form octahedral sites around the Mo_{imp}. These configurations have a coordination number of six, corresponding to the six neighboring sulfur atoms. The T'-AA' and T'-AB' configurations for the Mo_{imp} form a tetrahedral structure with a coordination number of four, then, the sulfur atoms in the top and bottom layers form a tetrahedral site for the Mo_{imp}. These octahedral and tetrahedral environments are shown schematically at the top of Fig. 3.1. It is noteworthy that regardless of the final stacking, octahedral configurations are the most stable.

3.1.2 Electronic Properties

Results showing the band structures and the local density of states (LDOS) projected in real space for some of the considered configurations are presented in Fig. 3.2. We focus on the impurity in-gap states near the Fermi energy introduced by the Mo_{imp} atom, indicated by the areas enclosed by orange rectangles. The band structures of the most stable configurations show three distinctive in-gap states, joined in two groups, labeled as regions **1** and **2** with degeneracies of one and two, respectively. Although the Mo_{imp} in these two configurations presents an octahedral sulfur environment, the in-gap bands present slightly different dispersive behavior. In region **1**, the band for the T-AB' case is more dispersive than the corresponding band for the H-AA' configuration, which is almost flat. The states in region **1** mainly have d_{z^2} orbital character, as shown in the LDOS of panels (d) and (e). Note that in region **1**, the surrounding region of the impurity for the T-AB' case has some hybridization with bilayer orbitals, which is not observed for the H-AA' case. In region **2** of the T-AB' case, there are two energy bands which are mainly non-bonding Mo_{imp} d orbitals with the neighboring sulfur atoms, as shown in the LDOS in panels (d) and (e). By comparing the T-AB' and H-AA' configurations, the stability order can be associated with the widening of the bands in regions **1** and **2** and to the displacement of the bands in region **2** to lower energies in the T-AB' configuration. The band structures in the T-AB' and H-AA' configurations are spin-compensated and related to the impurity in an octahedral sulfur environment. We now focus on the T'-AA' and T'-AB' cases. These two configurations have similar energy band structures and are found to have close energies. Both systems exhibit spin polarized behavior with a total magnetic moment of $2\mu_B$, which is determined by a similar Mo_{imp} tetrahedral environment. In particular for the T'-AA' configuration, the spin up and spin down components of the spatial resolved LDOS are shown in Fig. 3.2 panel (f). The state in region **1** has a d_{z^2} orbital character; however, it is above the Fermi level. The LDOS of the lower impurity states, the up states in region **3**

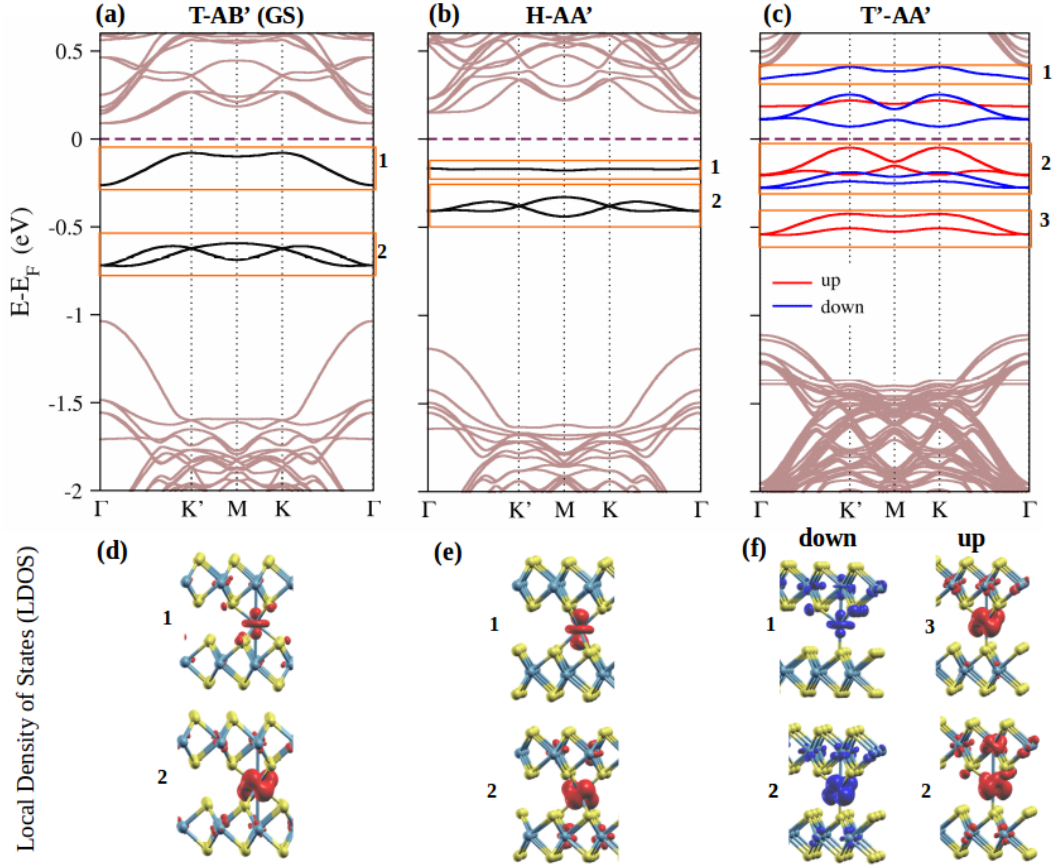


Figure 3.2: (a-c) Band structures for the given configurations. GS in T-AB' configuration indicates the ground state. The Fermi energy is set to 0 eV. Orange rectangles enclose the Mo_{imp} bands separated into several different energy regions, labeled as **1**, **2** and **3**. (d-f) Local density of states (LDOS) projected in space for the Mo_{imp} bands in the band gap region of the MoS₂ bilayer.

and the spin down component in region **2** are nearly equal, depleting the LDOS in the Mo_{imp}-S bond direction as in the T-AB' case. However, the states responsible for the spin polarization in the T'-AB' and T'-AA' configurations are the spin up *d*-orbitals in region **2**, which are along the Mo_{imp}-S bonds.

We also find that the LDOS is localized not only on the Mo_{imp}, but also on one of the MoS₂ layers. This layer asymmetry indicates that doping by electrons or holes could spatially differentiate between the two layers in the MoS₂ bilayer, a finding that could be of use in optoelectronic applications [150, 85].

The electronic structure for the impurity level states is best understood using crystal field theory. We analyze the ligand field splitting for the Mo_{imp} *d*-orbitals produced by

the interactions with the sulfur ligands for the octahedral and tetrahedral sites. The bonding and non-bonding interactions of d -orbitals for octahedral and tetrahedral sites are in agreement with the energy level scheme shown in Fig. 3.3. We consider the z -axis perpendicular to the layers and the x and y axes in the in-plane layer. In the octahedral environment for the T-AB' and H-AA' configurations, the sulfur ligands overlap less with the in-plane d_{xy} and $d_{x^2-y^2}$ orbitals, these orbitals are therefore non-bonding and have the lowest energy. The d_{z^2} orbital remains non-bonding at an intermediate energy, interacting less with the sulfur atoms. We next find that the d_{xz} and d_{yz} orbitals are more strongly directed and interact with the sulfur atoms along Mo_{imp}-S bonds, lying at higher energies, as is showed in Fig. 3.3(a). In the case of tetrahedral environment for T'-AB' and T'-AA', shown in Fig. 3.3(b), the d_{xy} and $d_{x^2-y^2}$ orbitals behave similarly to the octahedral structure; however, the d_{xz} and d_{yz} orbitals exchange roles with the d_{z^2} orbital. Thus, the d_{z^2} orbital in the tetrahedral environment interacts more with the sulfur ligands increasing its energy, as shown for region **1** of Fig. 3.2(c) and (f) in the T'-AA' case. The level filling help to explain why the tetrahedral cases have spin polarization, and a total magnetization of $2\mu_B$, as shown by the arrow counting.

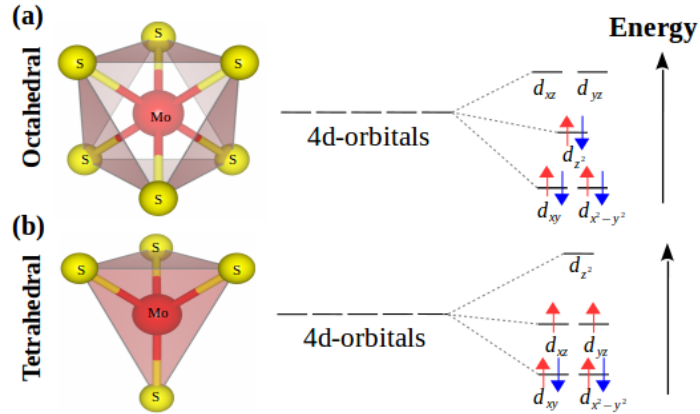


Figure 3.3: Ligand field splitting for Mo_{imp} d -orbitals produced by the neighboring sulfur atoms in (a) octahedral and (b) tetrahedral environments.

The main effect in our calculations is the interaction of the Mo impurity with the MoS₂ layers in the order of electron volts. The effect of SOC in the stacking stability is expected to be minimal although it would split bands near the Fermi level [26, 86]. Since the SOC is particularly noticeable in materials without inversion symmetry [151], we can expect the following effects. On the one hand, the pristine bilayers in the 2H-phase present point-center inversion symmetry, and the band structure remains spin degenerate even in the presence of SOC [51, 82]. SOC can change the pristine

bilayer bands in the 3R-phase because the lack of inversion symmetry would break the spin degeneracy and could lead to valley dependent spin polarization [152]. On the other hand, we can expect a splitting of the Mo_{imp}-bands due to the presence of spin-orbit and the lack of inversion symmetry in the tetrahedral configurations [see Fig. 3.3(b)]. However, the impurity in the tetrahedral arrangement is not the most stable configuration by an energy difference of 1.7 eV, much larger than values typically associated to the SOC energies in TMD structures.

We now consider the gap changes in the bulk bands, shown in light-color in Fig. 3.2, and induced by the Mo_{imp}. It is important to mention that the indirect gap along $\Gamma - K$ direction of 1×1 unit cell becomes a direct band gap at the Γ -point due to the k -space folding of large 3×3 unit cell. The calculated pristine band structure with 1×1 unit cell for the MoS₂ bilayers and diverse stackings are shown in Subsection 2.1.3. It is well known that band gaps calculated using both, GGA and LDA underestimate the values produced in experiments, so we discuss differences in magnitude gaps. The layer-gap is indicated by the energy difference between the valence bulk band maximum and the conduction bulk band minimum at the Γ -point. The bulk energy gaps of the pristine MoS₂ layers are correlated with the interlayer distances. In Table 3.1 we present the interlayer distances and layer-gaps for pristine and Mo_{imp} MoS₂ bilayer configurations. We check that the gap and distances for the AB' pristine stacking are $\simeq 0.1$ eV smaller and 0.03 \AA shorter than the values for the AA' pristine case. The layer-gaps and the interlayer separation including Mo_{imp} show larger values in comparison with the pristine cases. Among the Mo doped systems, the most stable T-AB' case has the smaller layer-gap and the shortest interlayer separation. The layer-gap is $\simeq 0.2$ eV above the AB'-pristine, and the interlayer separation is 0.03 \AA larger than that of AB'-pristine. The layer-gap values for the H-AA' and the T'-AB' (T'-AA') increase from the T-AB' case by $\simeq 0.2$ eV and by 0.3 (0.42) eV respectively. These gap differences are somewhat correlated with the difference between MoS₂ layer-layer distances, $\sim 0.56 \text{ \AA}$, between the T-AB' and H-AA' case, a value that increases up to $\simeq 0.4$ ($\simeq 0.75$) \AA for the T'-AB' (T'-AA') configurations. The increase in the layer-bandgap with interlayer distance is explained by a weaker interlayer coupling.

The interlayer distances in the proximity of the impurity are larger than those far from it, which indicates the role of local strain. Furthermore, experiments prove that the band gap can be controlled by strain [153, 154, 155]. We propose that the electronic and structural modifications around the impurity could be used in a similar way to electronic confinement for embedded quantum dots. Current experimental techniques employing cross-sectional scanning transmission electron microscope anal-

3.1 MoS₂ bilayers with Mo Impurities

Configuration	Δ_z (Å)	Layer-gap (eV)
Pristine AB	6.02	0.88
Pristine AA'	6.07	1.02
Pristine AB'	6.04	0.93
T-AB'	6.07*	1.12
H-AA'	6.63*	1.34
T'-AB'	6.45*	1.42
T'-AA'	6.83*	1.54

Table 3.1: Relaxed parameters for MoS₂ pristine bilayers and Mo_{imp} bilayers, given in the order of stability. The interlayer Mo-Mo distance is given by Δ_z . For doped configurations, (*) indicates distances measured near the Mo_{imp}. Layer-gap is defined by the energy difference between the valence bulk band maximum and the conduction bulk band minimum at the Γ point.

ysis in encapsulated TMD materials can provide evidence of impurity species being trapped in the interstitial region [156, 24]. This effect thus has potential applications for optoelectronic devices as exciton traps around Mo-doped bilayers. A number of different experimental techniques can be used to corroborate our theoretical predictions, for instance angle-resolved photoemission spectroscopy and cross-sectional scanning transmission electron microscope analysis [157, 156]. Interestingly, the interlayer distance increase and the bandgap changes in realistic MoS₂ bilayer samples when MoS₂ nanoparticles are trapped in the interlayer region [31].

3.1.3 Stacking Change

Another possible implication of our results is that transition metal ions could be used to engineer the stacking between TMD bilayers and to tune their electronic properties. In the T-AB' and H-AA' configurations, the Mo_{imp} is located within sulfur ligands forming octahedral sites. In these two configurations, the Mo_{imp} presents structural differences in the relative position respect to the nearest Mo atoms, belonging to the top and bottom MoS₂ layers. The Mo_{imp} bonding produces a stacking change in T-AB' related to the total energy decrease. The interlayer Mo-Mo distance around the impurity is smaller around 0.1 Å than the interlayer distance away from the impurity. The shorter distance promotes the hybridization of the impurity states with the layer states increasing the dispersion of the in-gap impurity states.

A scheme for the stacking change it is shown in Figure 3.4. Starting from the AB' stacking, the AA' stacking is found by shifting a layer in the armchair direction. The maximum sliding coordinate correspond to the distance of the Mo-atom to the

center of the hexagon, $a_0 \approx 1.86$ Å. The energy profile along the sliding coordinate is calculated shifting the top layer, then fixing the in-plane coordinates for the Mo_{imp} and a MoS₂ unit far from the impurity and relaxing. Figure 3.4(a) shows the total energy along the above discussed sliding route. Away from the T-AB' configuration the energy increases smoothly passing through an energy maximum before reaching the final T'-AA' configuration. The maximum energy is found for a displacement of 1.76 Å ($\approx 0.95 a_0$) being 5 meV above the T'-AA' value. It is noteworthy that the total energy as a function the sliding coordinate shows an inflexion point corresponding to the point where the slip force is maximum. That point corresponds to a displacement of 0.69 Å ($\approx 0.37 a_0$) in the armchair direction. The slipping force calculated as the derivative of the total energy as a function of displacement shows a maximum force around 2.1 eV/Å, similar to the forces calculated with DFT. The Mo-Mo interlayer

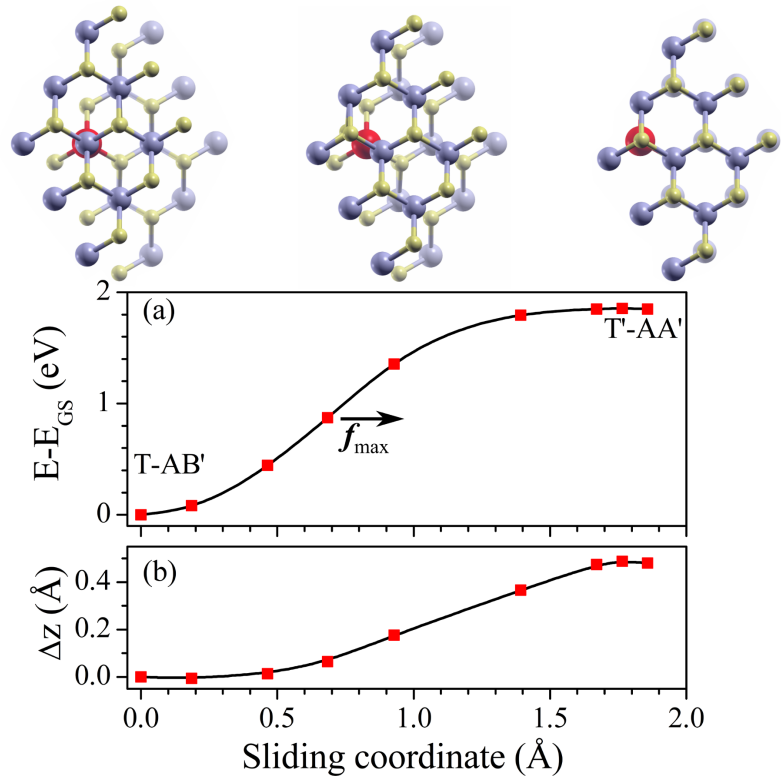


Figure 3.4: (a) Energy profile and (b) interlayer distance (Δ_z) by sliding between the 2H stackings. The sliding coordinate goes along the armchair direction. Full lines are just guiding to the eyes. Energies and distances shown are referenced with respect to the most stable configuration, that is, the T-AB'.

distance denoted as Δ_z [Fig. 3.4(a)] follows a similar trend as the total energy. For

the T'-AA' configuration, the interlayer distance is 0.48 Å larger than the value for the most stable configuration T-AB'. The maximum Δ_z is found for a displacement of 1.76 Å $\approx 0.95 a_0$ where the separation Δ_z is 10 mÅ higher than in T'-AA'.

3.2 Final Remarks

We have studied the structural and electronic properties of MoS₂ bilayers with Mo impurities in the interlayer region. We find that the most stable configuration is T-AB', with an energy gain above the vdW interaction because the Mo impurity levels strongly hybridize with the nearest atoms. A change in the stacking stability order from AA' to AB' is observed to be induced by Mo impurities, with the corresponding variation in energy gap. Thus, it is possible to engineer the stacking between TMD bilayers during the growth process, enabling their electronic properties to be fine-tuned.

Chapter 4

Tunable Spin-Polarized Edge Currents in Proximitized Transition Metal Dichalcogenides

Summary

Motivated by the successful combination of 2D materials with magnetic insulator substrates [123, 124, 125, 17, 37, 38, 39, 40], and the prediction of a giant splitting (300 meV) and a sizable Rashba field ($\lesssim 100$ meV) due to the induced magnetism when a MoTe₂ monolayer is deposited on a EuO substrate [35, 44], here we provide the missing piece on how TMD edges are affected by proximitized magnetism.

In this chapter we explore proximity-induced ferromagnetism on TMDs, focusing on MoTe₂ ribbons with zigzag edges deposited on FM EuO. A *magnetized* 3OTB model incorporates exchange and Rashba fields induced by proximity to EuO or similar substrates, allowing us to explore the electronic eigenstates and associated spin-polarized currents in the proximitized MoTe₂ ribbon. The *magnetized* 3OTB Hamiltonian uses first principles and experimental parameters as input, allowing us to model realistic systems where effective Rashba and exchange fields are transfer onto the TMD. We find that for in-gap Fermi levels, electronic modes in the nanoribbon are localized along the edges, acting as 1D conducting channels that carry tunable out-of-plane as well as in-plane spin-polarized edge currents.

The Chapter is organized in the following way: first, we briefly introduce pristine MoTe₂ zigzag ribbons. Here, note that the edge modes are in close relation with 1D Rashba systems as described in Subsection 2.4.1. Then in Section 4.2 we introduce our

magnetized 3OTB model in order to account for the proximity effects on the ribbon. The magnetized 3OTB allows us to obtain the spin projections, as explained in Section 4.3. With the magnetized Hamiltonian and spin projections in hand, we calculate both, pristine and defective edge spin currents. As we will see in Subsection 4.4.2, we report that although vacancies (the most common type of defects in MoTe₂ flakes) do indeed affect the spin currents in the MoTe₂-EuO system, they do so strongly only at high defect concentration. Our calculations show that reasonable defect concentrations (less than about 3% on-edge) reduce the spin currents by at most a factor of two, and do not totally suppress them until higher concentrations.

This part of the work has been done in collaboration with Dr. O. Ávalos-Ovando and Dr. S. E. Ulloa from Ohio University, Athens, Ohio, USA. A report of these results is published in Ref. [36].

4.1 Pristine MoTe₂ Zigzag Ribbons

The hexagonal lattice in TMDs allows clean edges to be labeled as zigzag or armchair-terminated (as in graphene), with the first being much more common and stable in the laboratory [67, 9, 158, 20, 10, 159]. Zigzag-terminated TMD structures reveal rich 1D behavior, such as metallic edge modes [68, 160, 69, 161, 9], and helical states that host Majorana bound states at the ends of a ribbon [69]. Twin boundaries have also been shown to host 1D charge density waves [58]. Non-magnetic 1D edge states have also been reported recently in topological superconductors [162], graphene superlattices [163], and for graphene on TMDs [111].

The intrinsic lack of inversion symmetry in the pristine 2D MoTe₂ monolayer yields two different terminations of zigzag edges, with outer Mo or Te atoms [69], as shown in Fig. 4.1(a). The zigzag-terminated MoTe₂ ribbons are constructed in such a way that PBC are along the x direction (both armchair edges are stitched together), hence the zigzag terminated PBC ribbon is acquired; at $y = 0$ we obtain the Mo-zigzag edge, while at $y = H$ the Te edge is obtained [106]. This intrinsic edge asymmetry produces different edge state dispersions and allows Rashba-type SOC along the edges of the ribbons [69].

We first model pristine MoTe₂ zigzag ribbons with dimensions of $N = 40$ and $H = 40$, that is $N_{sites} = N \times H = 1600$ Mo sites, equivalent to a ribbon with width of ~ 125 Å, and length of ~ 144 Å. After numerically diagonalization of the pristine 3OTB Hamiltonian in Eq. 2.8 and Fourier transform the states to extract the respective discrete momenta along the ribbon length, we obtain the energy spectrum for the

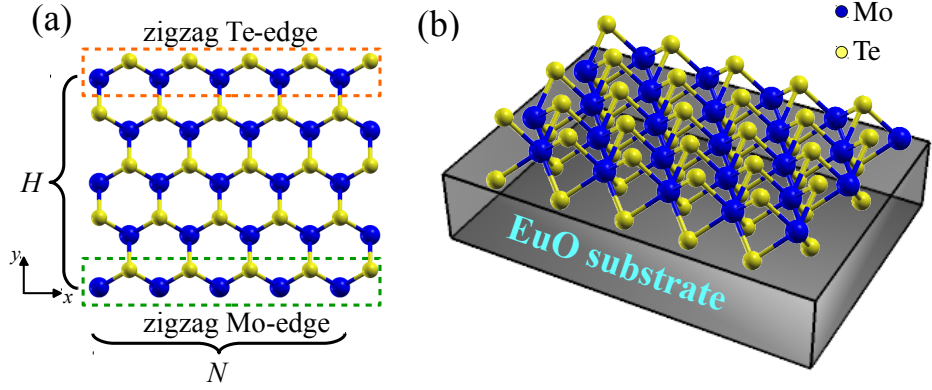


Figure 4.1: (a) Top view of a free-standing pristine MoTe_2 ribbon with zigzag Te and Mo-edges. N is the length and H is the width of the ribbon. For this example, $N = 5$ and $H = 5$, so that the ribbon have $N_{\text{sites}} = N \times H = 25$ Mo sites. (b) Schematic representation of the MoTe_2 ribbon in proximity to a FM substrate such as EuO. Eu atoms are hidden directly below the Mo atoms (blue spheres).

pristine ribbon in Fig. 4.2(a). Here, the K and K' valleys are located at $k_x = -2\pi/3a$ and $k'_x = 2\pi/3a$, respectively, where a is the MoTe_2 lattice constant. K and K' points are indicated as dashed gray lines in Fig. 4.2. Note that both, the valence bulk maxima and the conduction bulk minima are located at the K valleys and related each other by TRS as in the 2D MoTe_2 monolayer showed in Fig. 2.6(a). Due to the finite size structure and the asymmetry at the edges, two Rashba-type spin-polarized edge modes appear lying in the bulk gap, the Mo edge mode and the Te edge mode, which have metallic character. The Mo mode has positive mass and resides at the Mo edge, while the Te mode has negative mass residing at the Te edge, as is verified through the projected wave functions in the ribbon real space [see Fig. B.1 of Appendix B]. For any in-gap Fermi level and around $k_x = 0$, the edge modes have opposite group velocity and spin polarization because TRS and Rashba-type SOC [69].

As we show below, the energy dispersion is modified when the MoTe_2 zigzag ribbon is on the EuO substrate, specially for the edge modes, which are affected by proximity-induced magnetism. For that, we introduce our *magnetized* 3OTB model accounting for proximity interactions induced by the FM substrate, which is commensurate with the 2D MoTe_2 lattice.

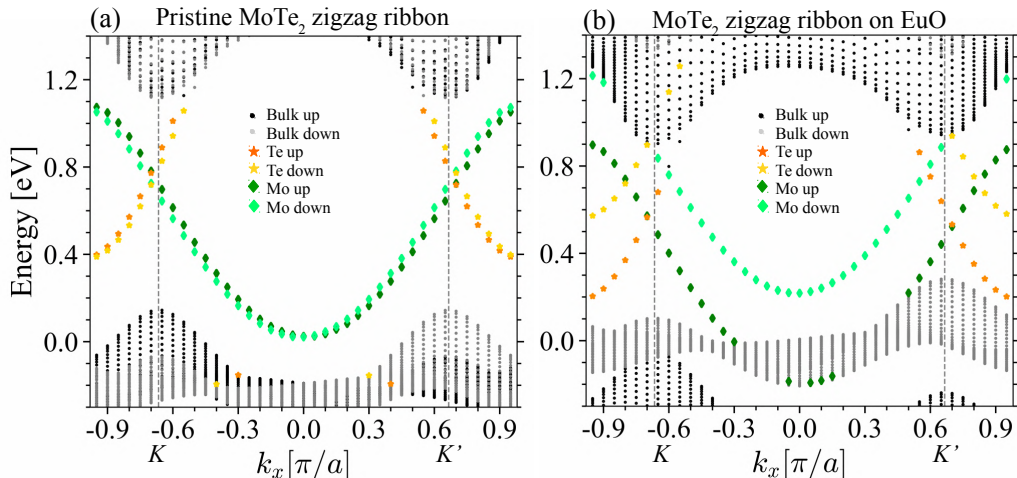


Figure 4.2: Energy spectrum for the MoTe₂ zigzag-terminated ribbon projected with spin $s_z = \uparrow, \downarrow$, of size $N = 40$, $H = 40$ (1600 Mo sites) for the pristine case in panel (a), when the MoTe₂ ribbon is on the EuO substrate in panel (b). In both cases, the Mo edge modes are shown as green symbols, while orange symbols stand for the Te edge modes (see insets). Black (gray) dots characterize the bulk energy dispersion for spin up (down). In (a), the Mo and Te edge modes as well as the valence and conduction bulk states are TRS related. In (b), the spectrum shows TRS breaking, associated with a valley splitting in the valence bulk bands, as well as to strongly spin-polarized edge modes in the bulk gap. The pristine in (a), and the magnetic-proximitized in (b) dispersions correspond to systems schematically shown in Fig. 4.1(a) and (b) respectively.

4.2 Magnetized 3OTB Hamiltonian

To describe the low-energy spectrum of a commensurate FM-TMD heterostructure over the entire Brillouin zone, as well as to model it in real space, we generalize the symmetry based low-energy effective $k \cdot p$ Hamiltonian (LEH) of Ref. [35] (which includes exchange and Rashba fields), into a successful *magnetized* 3OTB model, by including the proximity-induced exchange and Rashba terms into the pristine 3OTB Hamiltonian, which was described in Subsection 2.3.1.

The nearly commensuration of the MoTe₂-EuO heterostructure [35, 44], as the EuO (111) surface and TMD lattice have only a 2.7% mismatch, incorporates the substrate effects into the pristine MoTe₂ as onsite magnetic exchange and Rashba fields, as

$$\mathcal{H}_{\text{MoTe}_2-\text{EuO}} = \mathcal{H}_{\text{MoTe}_2} + \mathcal{H}_{\text{ex}} + \mathcal{H}_{\text{R}}. \quad (4.1)$$

Here, $\mathcal{H}_{\text{MoTe}_2}$ is the pristine TMD Hamiltonian given in Eq. 2.8, which is written in the

3O basis $\{|d_{z^2}, s\rangle, |d_{xy}, s\rangle, |d_{x^2-y^2}, s\rangle\}$, with spin index $s = \uparrow, \downarrow$ [60]. The *magnetized* terms, the exchange (\mathcal{H}_{ex}) and the Rashba Hamiltonian (\mathcal{H}_{R}) are obtained under a basis transformation from the LEH. Note that the electronic basis for the LEH is $\{|d_0, s\rangle, |d_{\pm 2}, s\rangle\}$, the same as the effective $k \cdot p$ model described in Eq. 2.2 with

$$d_0 = d_{z^2} \quad \text{and} \quad d_{\pm 2} = \frac{1}{\sqrt{2}}(d_{x^2-y^2} \pm id_{xy}). \quad (4.2)$$

The exchange term in this basis is given by

$$H_{\text{ex}} = -s_z(B_c\sigma_+ + B_v\sigma_-), \quad (4.3)$$

while the Rashba term is given by Eq. 2.22, which is

$$H_{\text{R}} = \lambda_{\text{R}}(\tau\sigma_x s_y - \sigma_y s_x).$$

$\sigma_{\pm} = \frac{1}{2}(\sigma_0 \pm \sigma_z)$. $\sigma_{\beta}, s_{\beta}$ ($\beta = 0, x, y, z$) are the Pauli matrices acting in the orbital and real spin space, respectively, $B_c = 206$ meV and $B_v = 170$ meV are the effective exchange fields experienced in the conduction and valence band of the MoTe₂ monolayer, respectively, $\lambda_{\text{R}} = 72$ meV is the Rashba field parameter and τ is the valley index. The exchange Hamiltonian is diagonal in spin representation, with matrix elements

$$\langle d_0, s | H_{\text{ex}} | d_0, s \rangle = -sB_c \quad \text{and} \quad \langle d_{\pm 2}, s | H_{\text{ex}} | d_{\pm 2}, s \rangle = -sB_v. \quad (4.4)$$

The Rashba field mixes spin and orbital components, with matrix elements

$$\langle d_0, \uparrow | H_{\text{R}} | d_{\pm 2}, \downarrow \rangle = \langle d_{\pm 2}, \downarrow | H_{\text{R}} | d_0, \uparrow \rangle^{\dagger} = -i\lambda_{\text{R}}(\tau - 1), \quad (4.5a)$$

$$\langle d_0, \downarrow | H_{\text{R}} | d_{\pm 2}, \uparrow \rangle = \langle d_{\pm 2}, \uparrow | H_{\text{R}} | d_0, \downarrow \rangle^{\dagger} = i\lambda_{\text{R}}(\tau + 1). \quad (4.5b)$$

In order to construct the *magnetized* 3OTB Hamiltonian, we unfold the electronic states from Eq. 4.2 as

$$|d_0, s\rangle = |d_{z^2}, s\rangle, \quad (4.6a)$$

$$|d_{xy}, s\rangle = \frac{-i}{\sqrt{2}}(|d_{+2}, s\rangle - |d_{-2}, s\rangle), \quad (4.6b)$$

$$|d_{x^2-y^2}, s\rangle = \frac{1}{\sqrt{2}}(|d_{+2}, s\rangle + |d_{-2}, s\rangle). \quad (4.6c)$$

Then, with Eqs. 4.4, 4.5, and 4.6, we construct the exchange $\langle \phi_{\mu}, s | \mathcal{H}_{\text{ex}} | \phi_{\mu}, s \rangle$ and Rashba $\langle \phi_{\mu}, s | \mathcal{H}_{\text{R}} | \phi_{\mu'}, s' \rangle$ ($\mu, \mu' = 1, 2, 3$) matrix elements in the 3O basis, where $\phi_1 =$

d_{z^2} , $\phi_2 = d_{xy}$ and $\phi_3 = d_{x^2-y^2}$. Finally, the exchange and Rashba fields represented in the 3O basis are

$$\mathcal{H}_{\text{ex},\uparrow\uparrow} = -\mathcal{H}_{\text{ex},\downarrow\downarrow} = \begin{bmatrix} -B_c & 0 & 0 \\ 0 & -B_v & 0 \\ 0 & 0 & -B_v \end{bmatrix} \text{ and } \mathcal{H}_{R,\uparrow\downarrow} = \mathcal{H}_{R,\downarrow\uparrow}^\dagger = \sqrt{2}\lambda_R \begin{bmatrix} 0 & -1 & i \\ 1 & 0 & 0 \\ -i & 0 & 0 \end{bmatrix}. \quad (4.7)$$

Figure 4.3 shows the continuous energy dispersion for the 2D MoTe₂ monolayer on

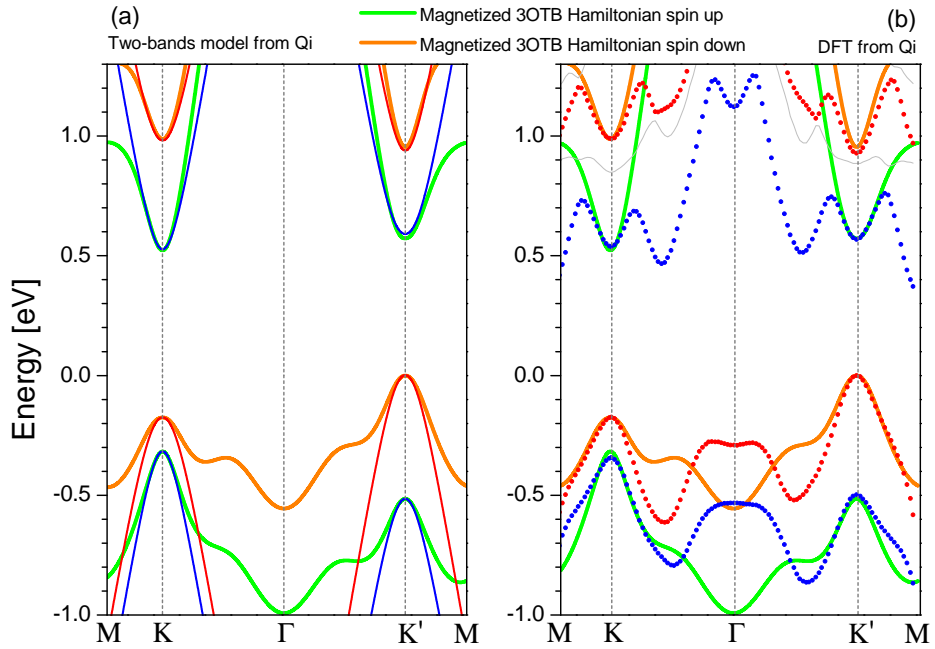


Figure 4.3: Band structure along high symmetry points of the BZ for the 2D MoTe₂ monolayer on EuO. Blue and red bands stand for spin up and spin down, respectively. In panel (a), they are obtained from the LEH near the K and K' valleys, that fits well DFT band structure results in (b) [35]. Green (orange) solid lines indicates the band structure obtained from the *magnetized* 3OTB model [Eq. 4.1] for spin up in blue and spin down in red, which take into account the *magnetized* terms from Eqs. 4.7.

EuO, as blue (spin up) and red (spin down) colors, in panel (a) from the LEH, in panel (b) from DFT calculations of Ref. [35]. Our *magnetized* 3OTB model (green and orange solid lines) is in excellent agreement near the K and K' valleys with respect to the LEH and DFT models for both, the valence and conduction bands. Inclusion of second NN hoppings for Mo atoms from Ref. [60], improves the agreement for momenta away from the valleys (especially near the Γ point), but in the valleys the fitting does not change. Our *magnetized* 3OTB model provides excellent description for energies \sim

300 meV from the valence band edge, corresponding to hole doping levels of the order of 10^{12} cm^{-2} , similar to experimental doping values [164]. Notice that this 3OTB exchange field Hamiltonian, with the right choice of TMD-substrate parameters and appropriate boundaries, could be used to study other heterostructures of interest, such as WSe₂-CrI₃ and WS₂-MnO [37, 135]. This provides an efficient and reliable approach to study different properties and behavior of the proximity-induced magnetism.

The magnetic proximitized vertical heterostructure we model here with the *magnetized* 3OTB Hamiltonian include a MoTe₂ zigzag ribbon with 1600 Mo-sites [the same size as the free-standing pristine case presented in Fig. 4.2(a)], although different sizes do not qualitatively change results or main conclusions here. The combined finite size MoTe₂-EuO system is schematically shown in Fig. 4.1(b). The discrete energy-momentum spectrum for the MoTe₂-EuO finite size system near the bulk bandgap, projected along the ribbon zigzag edge, is shown in Fig. 4.2(b). Clear differences are seen to appear in the energy dispersion with respect to the free-standing case [compare Fig. 4.2(a) and (b)] as we describe in detail in the next Sections.

4.3 Spin Projections

The *magnetized* 3OTB Hamiltonian in Eq. 4.1 allows us to obtain the spin projections for the MoTe₂-EuO finite size system, for then to obtain the edge spin currents. For states written as $|\Psi\rangle = \sum_{\mathbf{l},\alpha} c_{\mathbf{l},\alpha,\uparrow} |\psi_{\mathbf{l},\alpha,\uparrow}\rangle + c_{\mathbf{l},\alpha,\downarrow} |\psi_{\mathbf{l},\alpha,\downarrow}\rangle$, the sum includes all metal \mathbf{l} sites in the ribbon, as well as the three orbitals $\alpha \in \{d_{z^2}, d_{xy}, d_{x^2-y^2}\}$; the spin projections $\langle S_l \rangle = \langle \Psi | S_l | \Psi \rangle$ with $S_l = \frac{\hbar}{2} s_l$ ($l = X, Y, Z$), are given by

$$\langle S_X \rangle = \sum_{\mathbf{l},\alpha} c_{\mathbf{l},\alpha,\uparrow}^* c_{\mathbf{l},\alpha,\downarrow} + c_{\mathbf{l},\alpha,\downarrow}^* c_{\mathbf{l},\alpha,\uparrow}, \quad (4.8a)$$

$$\langle S_Y \rangle = \sum_{\mathbf{l},\alpha} i(c_{\mathbf{l},\alpha,\downarrow}^* c_{\mathbf{l},\alpha,\uparrow} - c_{\mathbf{l},\alpha,\uparrow}^* c_{\mathbf{l},\alpha,\downarrow}), \quad (4.8b)$$

$$\langle S_Z \rangle = \sum_{\mathbf{l},\alpha} |c_{\mathbf{l},\alpha,\uparrow}|^2 - |c_{\mathbf{l},\alpha,\downarrow}|^2. \quad (4.8c)$$

Figure 4.4 shows the spin projections of energy spectrum near bulk gap along the zigzag edges of the MoTe₂ ribbon on EuO. The large intrinsic SOC in MoTe₂ competes with the proximity exchange field from the FM substrate, and leads to giant valley polarization in the 2D bulk [35], as well as to strongly spin polarized edge-modes in the finite ribbon. The spectrum shows broken TRS due to exchange fields both in bulk bands, as well as on edge states dispersing through the midgap and hybridizing with bulk bands.

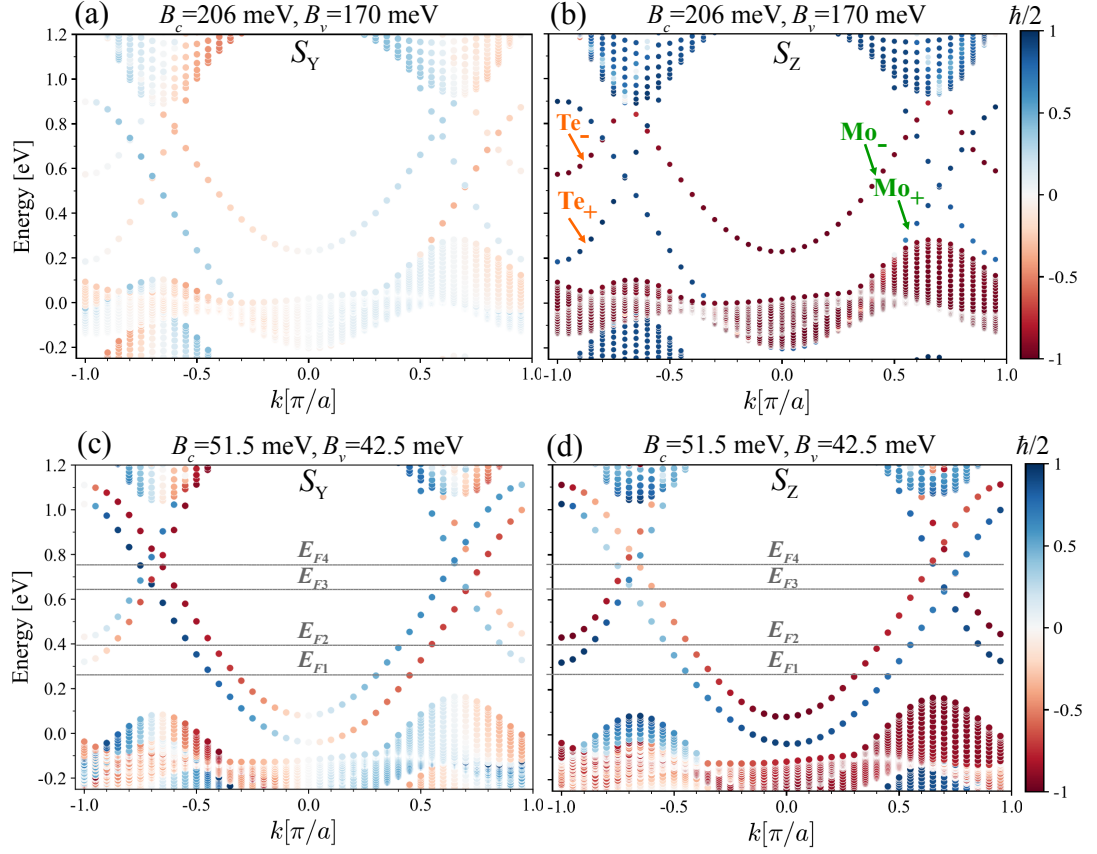


Figure 4.4: Spin projections of energy spectrum near bulk gap along the zigzag edges of a MoTe_2 ribbon on EuO. In (a)-(b) the exchange fields for EuO B_v and B_c are 100%. (a) Shows spin projections along the Y direction (S_Y); (b) along the Z direction (S_Z). In (b) Te_\pm , Mo_\pm label in-gap 1D edge modes located on the Te and Mo-edges termination, respectively. (c)-(d) Spectrum and S_Y , S_Z for weaker exchange fields as shown; notice smaller (larger) S_Z (S_Y) projection amplitudes than in (a) and (b). Gray lines indicate selected midgap Fermi levels used in Fig. 4.5. Color bar indicates positive (negative) spin projection as blue (red) gradient.

Panels 4.4(a)-(b) show the spin component content along S_Y and S_Z , respectively, for EuO exchange fields. For comparison, panels (c)-(d) show the S_Y - S_Z projection of the spectrum for weaker exchange fields (set to 25% of the EuO values). Different exchange fields could be achieved by different substrate surfaces, biaxial strains, and/or van der Waals engineering of FM heterostructures [37, 130]. For exchange fields shown, there are clear edge modes with dispersion in the bulk bandgap, and residing on either the Te-edge (labeled Te_\pm) or the Mo-edge (labeled Mo_\pm), where the subindex sign labels

helicity, and states appear with significant S_Y projection, canting away from S_Z . This Rashba field mixes the spin components in the MoTe₂ ribbon, which provides overall canting of spins, especially for the edge states. For the EuO full MEF, Fig. 4.4(a)-(b) show that the Mo₊ mode is non-degenerate and hybridized with the bulk valence band for small k , an effect not present for weaker exchange fields [Fig. 4.4(c)-(d)] when the Mo-edge modes are fully decoupled from the bulk and located midgap. In contrast, Te-modes are always hybridized to the bulk conduction bands for $|k| \simeq 0.5 \pi/a$, regardless of the exchange field strength. Notice the opposite group velocity of the different Mo- or Te-termination edge states at given k values.

The EuO substrate breaks inversion symmetry, allowing an external Rashba field [\mathcal{H}_R in Eq. 4.1] that generates spin mixing and canted spins for the edge states [59]. Here, the Rashba field is along the y -axis, confining the spin dynamics to the YZ plane [165, 33]. It is clear that weaker exchange fields result in reduced S_Z polarization, as evident in Fig. 4.4(b)-(d), with larger S_Y projection as the ratio of λ_R/B_v increases. As λ_R is in principle tunable via gate fields for a given substrate-specific exchange field B_v , it is reasonable to anticipate that the overall spin projection (or canting) could be tunable in a given structure at specific Fermi energy.

Essential elements in spintronics include being able to inject, manipulate or detect spin polarization [32, 166]. The Te- and Mo-edge modes are strongly spin-polarized along S_Z —see Fig. 4.4. Te_± and Mo_± modes with opposite momentum ($k \rightarrow -k$) propagate in opposite directions with the same S_Z projection, while the S_Y component reverses for opposite momentum, as in Fig. 4.4(a)-(c). This behavior is unchanged for larger λ_R/B_v ratios, although with larger S_Y projection, as the Rashba field is effectively stronger [see Fig. 4.4(c)].

As we discuss next, edge spin currents are predicted to appear for Fermi levels in the bulk energy gap of the magnetic proximitized finite size MoTe₂-EuO system.

4.4 Edge Spin Currents

Our spin current calculations follow the approach described by Sinova *et al.* [33, 115], which considers a Hamiltonian with substantial intrinsic Rashba-type SOC (as described in Section 2.4) and effective Zeeman terms, similar to our case. They show that an effective torque produced by electric fields in the \hat{x} direction tilts the spins along the \hat{y} direction when moving with momentum \vec{p} , creating a spin current in the y direction given by

$$j_y^{\text{spin}} = \int_{\text{annulus}} \frac{d^2 p}{(2\pi\hbar)^2} \frac{\hbar}{2} n_{z,\vec{p}} \frac{p_y}{m}, \quad (4.9)$$

where $n_{z,\vec{p}}$ is the z component of the spin for an electron in a state with momentum \vec{p} , and m is the electron effective mass. The integration is performed over the annulus of momentum states contributing to the spin current.

In our case, where extrinsic Rashba and exchange fields from the EuO substrate affect the midgap states near the Fermi level of interest, the spin current along the l spin projection [Eqs. 4.8] can be rewritten as,

$$j_l^{\text{spin}} = \sum_{\substack{\text{states in} \\ E_F \pm \frac{\delta}{2}}} \langle \Psi | S_l v_x | \Psi \rangle, \quad (4.10)$$

where $\hbar v_x = \partial \varepsilon(k) / \partial k = \hbar k_x / m(k)$ is the group velocity, and the summation is over an energy window δ around the Fermi level E_F for right movers (positive momentum k_x , i.e., the direction of the charge current).

In the following, we discuss how to use this expression for calculating spin currents for midgap electronic states in the MoTe₂-EuO finite-size system, in both, the pristine case and when defects such as vacancies are present in the combined structure.

4.4.1 Pristine Spin Currents

For pristine MoTe₂ ribbons on EuO, the full spin current expression in Eq. 4.10 reduces to $j_l^{\text{spin}} = k S_l \hbar / m$, ($l = Y, Z$), as each wave function has well-defined k momentum along the edge [see Fig. B.1 in Appendix B], and effective mass $m(k)$ at the corresponding Fermi level.

To characterize the propagation along the 1D Te- and Mo-edges, we select different in-gap Fermi levels to calculate the spin currents. The Fermi level can be shifted by an overall gate field perpendicular to the TMD layer, allowing for tunable spin current values and polarizations [167, 168].

Figure 4.5 shows spin currents for the MoTe₂ ribbon with Fermi levels in Fig. 4.4(c)-(d), with $j_l = m j_l^{\text{spin}} / \hbar = k S_l$. Given that the bulk current vanishes for in-gap Fermi levels, the non-vanishing spin currents for such levels are contributed by only the Mo- and Te-edge states and propagate along the edges of the ribbon. A 1D spin current along the Mo-edge is shown for right-movers ($k > 0$) at E_{F1} in Fig. 4.5(a). At this Fermi level, both spin-split Mo-modes contribute to the spin current with j_Y and j_Z pointing to negative and positive directions, respectively—notice no Te-modes contribute yet at this level. As higher Fermi levels are reached, as in the case of E_{F2} and E_{F3} , the spin-polarized Te-modes are turned on, and contribute to the spin currents, as shown in Fig. 4.5(b)-(c).

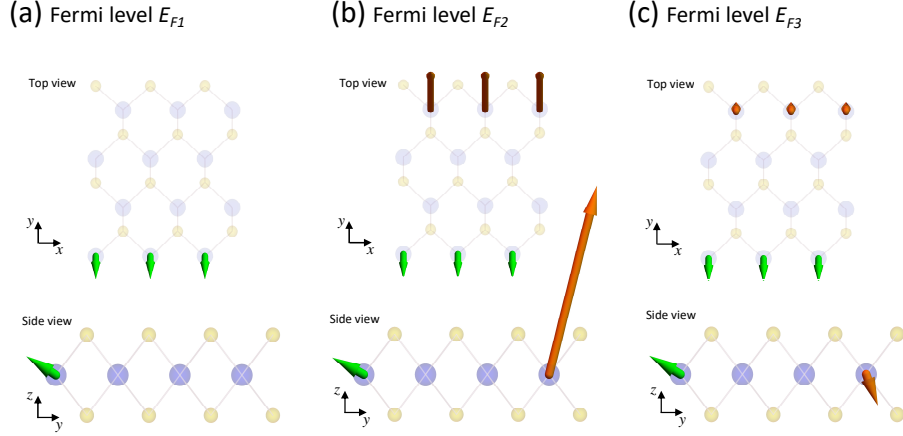


Figure 4.5: Spin currents $\mathbf{j} = (j_Y, j_Z) = m\mathbf{j}^{\text{spin}}/\hbar$ for system in Fig. 4.4(c)-(d), for both Mo (green arrows) and Te (orange arrows) ribbon edges. Results for different Fermi levels, E_{F1} (a), E_{F2} (b) and E_{F3} (c). The spin current is along the zigzag direction ($k > 0$). The arrow's size (direction) indicates the magnitude (orientation) of the spin current. The magnetic substrate is not shown and the ribbon size is only schematic. E_{F4} yields similar results to E_{F3} (not shown).

The spin currents along the Mo-edge are small in magnitude, and have nearly the same polarization for all chosen Fermi levels, as shown by the green arrows in Fig. 4.5, because the spin projections for both spin-split Mo modes nearly cancel each other. The current orientation and magnitude do not significantly change for any midgap Fermi level. This suggests that the effect of the EuO substrate on pristine Mo-edges (as those experimentally available [9, 158, 20]) might indeed result in strong spin current measurements/devices. The spin currents along the Te-edge vary drastically with Fermi level, orange arrows in Fig. 4.5. The spin current for E_{F2} has a large j_Z component and non-vanishing j_Y , as only the Te_+ mode contributes. However, the Te-edge spin current becomes small and with reverse polarization for E_{F3} (or E_{F4}), as both Te_\pm modes contribute with nearly the same magnitude and opposite polarization. The orientation and magnitude difference of these two regimes is clearly seen in Fig. 4.5(b) and (c), where the spin current flip is evident, showing spin currents that are canting away from the MoTe_2 ribbon. All these regimes give a great deal of tunability for possible spin current devices on both edges. Accordingly, one could modulate the spin-polarized currents along the Mo-edge, or simultaneously along the Te-edge of the zigzag ribbon, by tuning the Fermi level across the structure [167, 168]. Similar spin-polarization in graphene nanoribbons has been proposed as spin injector device [131, 121], with

perhaps some practical advantages in the current TMD-based structure.

As we describe above, the bulk current vanishes for in-gap Fermi levels, where 1D spin currents for such levels are found, which are contributed by only the Mo- and Te-edge states and propagate along the edges of the ribbon. Therefore, we have constructed an effective 1D Hamiltonian accounting for the edge spin currents.

4.4.1.1 Effective 1D Model

The effective 1D Hamiltonian for the hybrid MoTe₂-EuO edges is

$$\begin{aligned} \mathcal{H}_{\text{eff}}^{\alpha}(k) &= \varepsilon^{\alpha} - \alpha[\hat{\sigma}_z + 1]t_{\uparrow}^{\alpha} \cos k + \alpha[\hat{\sigma}_z - 1]t_{\downarrow}^{\alpha} \cos k \\ &\quad + \hat{\sigma}_z(t_{SO}^{\alpha} \sin k + b^{\alpha}) - \hat{\sigma}_y t_R^{\alpha} \sin k, \end{aligned} \quad (4.11)$$

$$\begin{aligned} \mathcal{H}_{\text{eff}}^{\beta}(k) &= \varepsilon^{\beta} - \beta[\hat{\sigma}_z + 1]t_{\uparrow}^{\beta} \cos k + \beta[\hat{\sigma}_z - 1]t_{\downarrow}^{\beta} \cos k \\ &\quad + \hat{\sigma}_z(t_{SO}^{\beta} \sin k + b) - \hat{\sigma}_y t_R \sin k + \alpha_R k \hat{\sigma}_z \end{aligned} \quad (4.12)$$

or in matrix form as

$$\mathcal{H}_{\text{eff}}^{\alpha} = \begin{bmatrix} \varepsilon^{\alpha} - \alpha 2t_{\uparrow}^{\alpha} \cos k + \alpha t_{SO}^{\alpha} \sin k + \alpha b^{\alpha} & i t_R^{\alpha} \sin k \\ -i t_R^{\alpha} \sin k & \varepsilon^{\alpha} - \alpha 2t_{\downarrow}^{\alpha} \cos k - \alpha t_{SO}^{\alpha} \sin k - \alpha b^{\alpha} \end{bmatrix}, \quad (4.13)$$

where α indicates Mo ($\alpha = 1$) or Te ($\alpha = -1$) edges, in terms of onsite energies ε^{α} , effective bandwidths for the spin up/down $t_{\uparrow/\downarrow}^{\alpha}$ bands, as well as Rashba t_R^{α} , and diagonal SOC t_{SO}^{α} and exchange fields b^{α} . The edge dispersion calculated from Eq. 4.12 is shown in Fig. 4.6(a). There is excellent agreement between numerical results (symbols) and the fitted model (lines)¹ for all Mo- and Te-modes. This Hamiltonian captures the spin content of the edge state dispersions and allows one to easily obtain the spin currents for the system. Spin currents for Mo and Te modes, shown in Fig. 4.6(b)-(c), are sizable for Fermi levels in the bulk gap region. Notice the Mo₊ mode is never singly-populated, as bulk states in the valence band are also reached before Mo₋ is populated, for $E_F \lesssim 0.1$ eV. For $E_F \sim 0.15$ to 0.3 eV, both Mo-edge modes are populated, and the spin current remains nearly constant and only present on that edge throughout that E_F -window. As the Te₊ mode is reached only one spin branch at the Te-edge is populated for $E_F \sim 0.3$ to 0.45 eV, with a correspondingly large spin current

¹We obtain $\varepsilon^{\text{Mo}} = 550$, $t_{\uparrow}^{\text{Mo}} = 263$, $t_{\downarrow}^{\text{Mo}} = 254$, $t_{SO}^{\text{Mo}} = 16$, $t_R^{\text{Mo}} = 72$ and $b^{\text{Mo}} = 51$ for the Mo modes, and $\varepsilon^{\text{Te}} = 1150$, $t_{\uparrow}^{\text{Te}} = 407$, $t_{\downarrow}^{\text{Te}} = 347$, $t_{SO}^{\text{Te}} = 51$, $t_R^{\text{Te}} = 72$ and $b^{\text{Te}} = 51$ for the Te modes, all in meV.

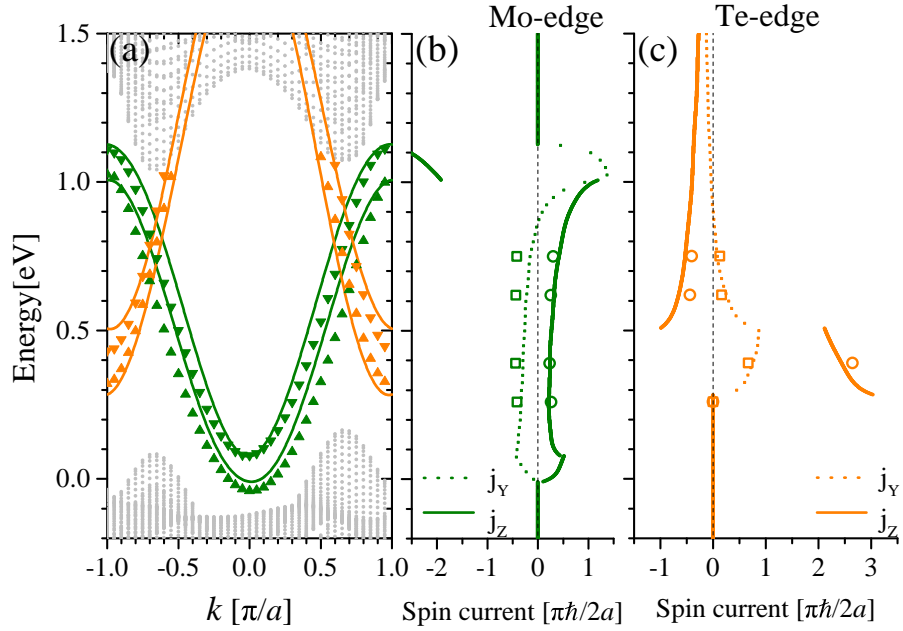


Figure 4.6: (a) Analytical bands for Mo-edge (green lines) and Te-edge (orange lines) from Eq. (4.12) and TB bands (gray dots and color triangles); $\text{Mo}_{+,-}$ and $\text{Te}_{+,-}$ bands highlighted as up/down color arrows, for system in Fig. 4.4(c)-(d). (b) Spin current components j_Z (solid) and j_Y (dotted) obtained from analytical model for Mo-edge, and (c) for Te-edge, for $k > 0$. Symbols in (b) and (c) are numerical values as seen in Fig. 4.5. The 1D effective analytical model captures the dispersions, wave functions and the spin currents of the TB results.

on that border. The current drops when the Te_- mode is reached for $E_F \gtrsim 0.5$ eV. The spin current varies slowly, decreasing as the Fermi level reaches the conduction band.

4.4.2 Defective Spin Currents

Although nearly-perfect sections of both Te- and Mo-edges are found in experiments [9, 158, 20], we have also studied the role of structural defects on the spin currents. We find the spin currents fall with increasing defect concentration, but persist over realistic ranges in experimental samples.

When the system contains defects such as vacancies (the most common type of defects in MoTe_2) along the edges (a detailed description for MoTe_2 ribbons with defects is in Appendix B), the associated midgap state wave functions exhibit oscillatory behavior in space, produced by vacancy-induced backscattering. Consequently, momentum is no longer a good quantum number, and each energy eigenstate can be written as

$|\Psi'\rangle = \sum_{\mathbf{l}, \alpha, k, s}^{N_{sites}} c_{\mathbf{l}, \alpha, k, s} |\psi_{\mathbf{l}, \alpha, k, s}\rangle$, such that the spin current can now be calculated as

$$j_l = \sum_{\substack{\text{states in} \\ E_F \pm \frac{\delta}{2}}} \langle \Psi' | S_l \hat{k}_x | \Psi' \rangle, \quad (4.14)$$

where \hat{k}_x is the momentum operator. In systems with defects, $|\Psi'\rangle$ for midgap states is characterized through the properly normalized fast Fourier transform (FFT) complex amplitudes for states obtained from the 3OTB model.

We have studied different vacancy configurations (number and location) at both edges, including 1, 2, or 5 vacancies at either edge, corresponding to 2.5%, 5%, and 12.5% of vacancy concentration on the edge. We expect 2.5% to be a realistic upper bound for the on-edge vacancy, as concentrations larger than 3% may seed crystalline phase transitions [169, 170], not seen in stable ribbons/flakes. Two kinds of vacancies are possible, from either the metal or chalcogen missing atom. When any edge vacancy is present, the spin current along the opposite edge remains unaffected, since the projected orbital component (POC) of the defective edge is entirely decoupled from the opposite ribbon edge. Similarly, when the vacancies are deep in the bulk, the edge spin currents are not affected. Hence, in the following we only show results for defective edges. As we will see, we find that at low concentration ($\lesssim 2.5\%$) on either edge, the spin current is smaller in magnitude but still sizable. Higher defect concentration, of course, further suppressed the spin (and charge) currents associated with the midgap states.

When analyzed in detail, we see that the presence of vacancies affects the j_z and j_y values the most at low energies, likely due to the high density of states there, and the appearance of highly localized states in that energy range ($E_F \simeq 0.1-0.2$ eV). For 2.5% of either Mo_v or Te_v present in the Mo-edge [Fig. 4.7(b)], we see that the magnitude of j_y decreases nearly by half, while in the Te-edge [Fig. 4.8(b)] remains nearly the same as in the pristine edge. On the other hand, j_z remains qualitatively the same on the Mo-edge for $E \gtrsim 0.5$ eV [Fig. 4.7(c)], while on the Te-edge [Figs. 4.8(c)] it is only sizable at energies when only the Te_+ branch contributes to the DOS ($\approx 0.3-0.5$ eV), and then drops to zero for higher energies.

When more impurities are present (5% and 12.5% on edge), Figs. 4.7 and 4.8 show that the spin currents are strongly suppressed, as one would expect. We see that as more vacancies are present on the edge, the spin currents exhibit stronger fluctuations through the midgap. Ensemble averaging would be expected to yield strongly suppressed spin currents, with perhaps large variations with Fermi energy, depending on

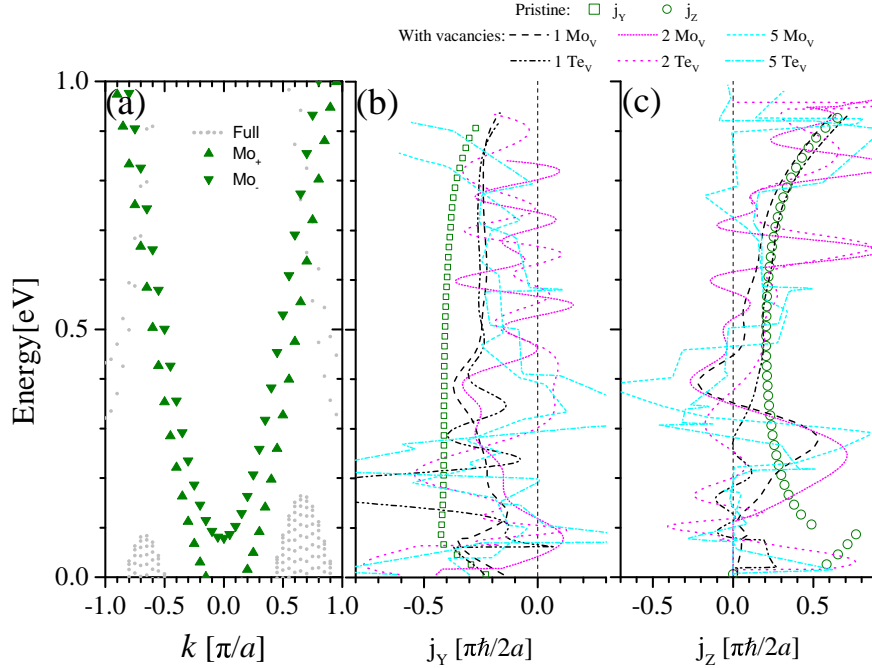


Figure 4.7: Results for vacancies on the Mo-edge. (a) Pristine dispersion, (b) spin current j_Y , and (c) j_Z for midgap states obtained from magnetized 3OTB model calculations. In (b) and (c), the spin currents for pristine edges are shown as empty symbols, while cases for different molybdenum (Mo_v) or tellurium (Te_v) vacancy concentrations are shown as indicated by different lines (1: 2.5%, 2: 5%, and 5: 12.5% on edge).

sample and current probe location in nanoscale systems.

We can further analyze the spin current decay as a function of vacancy concentration. Considering Mo_v on the Mo-edge as a representative example, the spin current is averaged over the energy window 0.6-0.8 eV. We find that the spin current drop with increasing defect concentration c_{Mo_v} and can be fit well with an exponential function,

$$j_l(\text{Mo}_v) = A_l + B_l e^{-c_{\text{Mo}_v}/t_l}, \quad (4.15)$$

with $l = Y, Z$, and $A_Y = -0.0177$, $B_Y = -0.19952$, $t_Y = 3.6\%$, $A_Z = 0.02927$, $B_Z = 0.10397$, and $t_Z = 2.1\%$. This shows that the spin currents are relatively robust for up to 2% (for j_Z) or 3.5% (for j_Y) of on-edge vacancy concentrations. Similar numbers are obtained for other vacancies and ribbon edges.

Figure 4.9 shows the numerical averaged spin current magnitudes (symbols) between Fermi levels E_{F3} and E_{F4} —this is, in a energy range which is not subject to sudden discontinuities—and fitted results for Eq. 4.15. One can see excellent agreement between

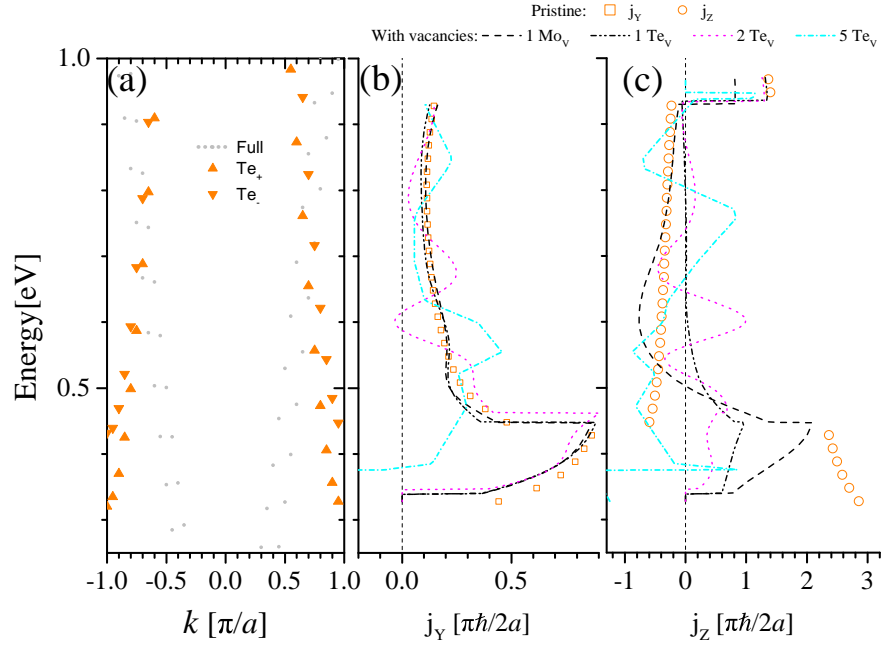


Figure 4.8: Results for vacancies on the Te-edge. (a) Pristine dispersion, (b) spin current j_Y , and (c) j_Z in midgap region, as obtained from magnetized 3OTB calculations. In (b) and (c), spin currents for pristine edges are shown as empty symbols. Different molybdenum (Mo_v) or tellurium (Te_v) vacancy concentrations are shown as indicated by different lines (1: 2.5%, 2: 5%, and 5: 12.5% on edge).

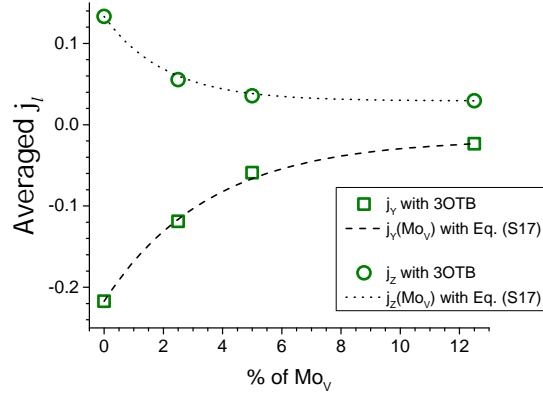


Figure 4.9: Spin current along Mo-edge vs concentration of Mo_v on the Mo-edge. Symbols are 3OTB averaged between 0.6 and 0.8 eV ($\simeq E_{F3}$ and E_{F4}), and lines are exponential fits, Eq. 4.15, with $l = Y, Z$ as indicated.

numerical and analytical results. Spin current j_Y is seen to decrease nearly twice faster than j_Z , suggesting that as the concentration on Mo_v increases the spin current canting

would be less appreciable as the vacancy concentration gets closer to 12.5% compared to the spin flipping provided, until eventually the spin current is destroyed for very irregular edges.

Further details depend on both the amount and the location of the vacancies. For a large number of impurities is expected that the spin current will vanish, since backscattering will play a larger role allowing no current to flow. All in all, we find that for pristine edges or vacancy concentrations $\lesssim 3\%$, strong and sizable spin currents are found in the band gap so any Fermi level selection would account for a measurable spin current. When more vacancies are present, the selection of the Fermi level would need to be more careful in order to find a desired spin current magnitude/orientation. These conclusion suggest that the effect of the spin current creation because of the EuO on the MoTe₂ ribbons, is a strong and measurable effect.

4.5 Final Remarks

The magnetized 3OTB Hamiltonian and the effective 1D description are able to incorporate the effects of magnetic proximity from a FM substrate onto the spin-polarized states and currents at the zigzag edges of TMD monolayer ribbons. The broken inversion and TR symmetries in a proximitized TMD ribbon lying on a FM substrate splits the electronic edge modes residing in the bulk midgap and produce effective 1D conducting channels with spin-polarized currents. Competition between the effective exchange and Rashba fields generates canting of the spin orientation of the spin currents. The spin current polarization and onset could be modulated by tuning the Fermi level [167, 168], and/or the effective exchange field by van der Waals engineering of heterostructures [37], or through biaxial strain [130], even when defects ($< 3\%$) such as vacancies are present in the system. The ready availability of samples and the flexibility of this effect suggests that such proximitized TMD ribbons could be effectively used as robust 1D spin injectors [121]. We also look forward to studies of electronic interactions in these 1D channels, involving strong spin-orbit coupling and broken symmetry.

Chapter 5

MoTe₂ Ribbons Proximitized to Antiferromagnetic Substrates

Summary

In this Chapter we complement the FM proximity study based on MoTe₂ ribbons with AFM proximity, and show the main and unique results for the combined AFM heterostructures. In Section 5.1 we describe commensurate finite-size MoTe₂-AFM vertical heterostructures with zigzag and armchair edges, where we consider two different magnetic ordering in the AFM substrates, taking into account the zero net magnetic moment condition that must have the AFM order. In Section 5.2 we model these vertical heterostructures within the magnetized 3OTB model, by means an adapted exchange field Hamiltonian term. In Section 5.3 we present the results for MoTe₂-AFM heterostructures with zigzag edges. Here we find that the Rashba intrinsic parameters such as the spin-splitting and the Rashba strength (present along the edge modes in free-standing TMD zigzag-terminated ribbons), respond to the external Rashba field coming from one type of AFM order. On the other hand, our main results for armchair-terminated ribbons on AFM substrates in Section 5.4, show that in-gap edge modes are either, gapless or gapped, which depend on the parity of the ribbon width. These are novel and intriguing results, which we expect may expand the study based on proximity-induced AFM interactions.

This part of the work is done in collaboration with Dr. O. Ávalos-Ovando and Dr. S. E. Ulloa from Ohio University, Athens, Ohio, USA. It is still ongoing work.

5.1 System

We study vertical heterostructures formed by monolayer MoTe₂ ribbons in close proximity to AFM substrates. The selection of AFM materials should meet two criteria. The AFM candidate materials have to be (i) semiconducting or insulating, with a bandgap ~ 1 eV in order to avoid extra electronic states in the bulk gap region; and (ii), the lattice mismatch for the heterostructure, the substrate AFM surface and the MoTe₂ ribbon should be small ($< 3\%$). Possible AFM candidates could be the manganese chalcogenophosphates compounds with formula MnPX₃ ($X = \text{S, Se}$), which have hexagonal lattice and are semiconducting [137]. Other AFM candidates could be manganese oxide (MnO) [135] or cobalt oxide (CoO) [136]. Although MnO and CoO substrates have been studied when in proximity to 2D TMD monolayers, the study of finite dimensionality structures such as edges and boundaries is still lacking.

Here we focus on AFM substrates (or AFM surfaces) satisfying both conditions above. We have considered two types of AFM order for the substrates, which are exactly below the TMD monolayer, labeled as either AFM1 and AFM2, as shown in Fig. 5.1(a) and (b) respectively. The magnetic moments within each AFM lattice surface are considered in such a way that the net magnetic moment in both AFM systems is zero. The magnetic moments of the prototype AFM substrates are projected on each Mo atom of the MoTe₂ ribbons, schematically shown in Fig. 5.1 as blue (up moments) and red (down moments) arrows. In the MoTe₂-AFM1 combined system, the up and down moments alternate between them inside each row along the x direction; in the MoTe₂-AFM2 system, adjacent rows alternate between up moments and down moments. Both configurations are also shown in Fig. 5.1. Our proximitized MoTe₂ ribbons have zigzag edges along the x direction and armchair edges along the y direction. Note that the choice of x and y directions along the ribbons is totally arbitrary. As we saw in Chapter 4, the zigzag edges have two different terminations, with outer Mo and Te atoms due to the lack of intrinsic inversion symmetry in the MoTe₂ 2D monolayer [26, 60, 69]. Armchair edges are combinations of Mo and Te atoms along the y direction [see Fig. 5.1].

The ribbon size in both systems MoTe₂-AFM1 and MoTe₂-AFM2, is an important parameter to consider in order to satisfy the net zero magnetic moment condition and the PBC in the ribbons. N has to be even in order to avoid creating pairs of parallel moments (net magnetic moment \neq zero) when a zigzag-terminated ribbon is constructed on the AFM1 substrate. If N is even on the AFM1 substrate, there is no restriction for the armchair-ribbon construction because H can be both even or odd

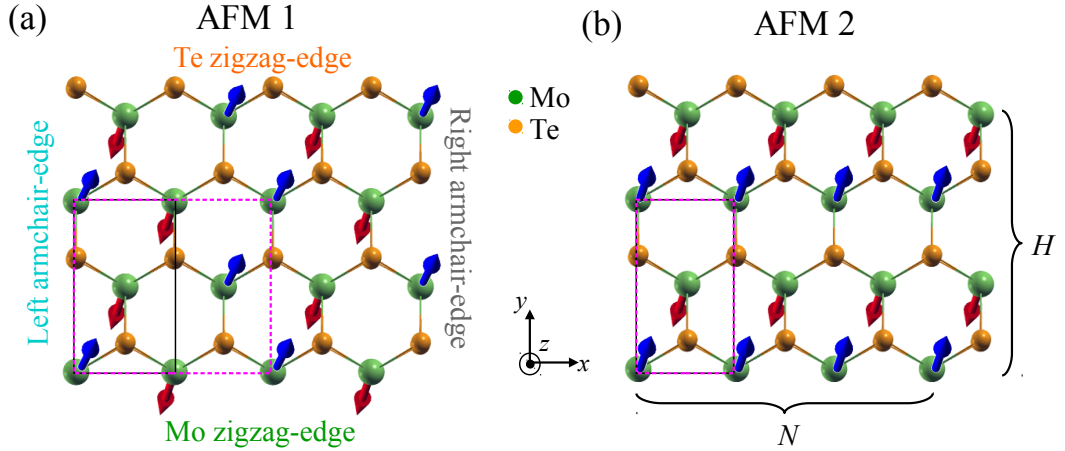


Figure 5.1: Schematic representation of MoTe_2 ribbons when in proximity to AFM substrates with different magnetic ordering, AFM1 in (a), AFM2 in (b). The AFM substrates are not shown, the ribbon size and shape is only schematic. The zigzag edges are along x direction (N), armchair edges are along y direction (H). At $y = 0$ we obtain the Mo-zigzag edge, while at $y = H$ the Te edge is obtained. Conversely, at $x = 0$ we obtain the left-armchair edge, while at $x = N$ we obtain the right-armchair edge. For this example, both MoTe_2 -AFM systems have dimension $N = 4$ and $H = 4$, then $N_{\text{sites}} = 16$ Mo sites. The top views in (a)-(b) are slightly tilted for a better visualization of the projected moments on the Mo atoms, shown as blue: up moment and red: down moment arrows, where equal amount of red and blue arrows identifies a net zero magnetic moment in either AFM system. Magenta (black) rectangles stand for the magnetic (geometric) unit cells in the ribbon. In (a) the magnetic cell is twice the geometric cell along the zigzag direction, in (b) both cells are the same.

[see Fig. 5.1(a)]. As show Fig. 5.1(b), the only restriction in the size of both zigzag and armchair-terminated ribbons on the AFM2 substrate is that H must to be even in order to satisfy the net magnetic moment zero condition; there is no restriction for N if the even- H condition is fulfilled.

5.2 Tight-Binding Description

In a similar way as MoTe_2 ribbons on FM substrates in Chapter 4, here in the AFM case we augmented the pristine 3OTB Hamiltonian to account for the AFM substrates as

$$\mathcal{H}_{\text{MoTe}_2\text{-AFM}} = \mathcal{H}_0 + \mathcal{H}_{\text{ex},s} + \mathcal{H}_R. \quad (5.1)$$

\mathcal{H}_0 describes the pristine TMD lattice, which considers onsite energies, hoppings between transition metal atoms up to first neighbors and SOC, as described in Eq. 2.8. The AFM substrate effects are incorporated into the pristine MoTe₂ lattice as onsite magnetic exchange and Rashba fields as $\mathcal{H}_{\text{ex},s} + \mathcal{H}_R$, with $s = \uparrow, \downarrow$ the spin index. The induced AFM exchange field $\mathcal{H}_{\text{ex},s}$ is spin diagonal and onsite dependent, for AFM magnetized upward can be written as

$$\mathcal{H}_{\text{ex},\uparrow} = \begin{bmatrix} \mathcal{H}_{\text{ex},\uparrow\uparrow} & 0 \\ 0 & \mathcal{H}_{\text{ex},\downarrow\downarrow} \end{bmatrix}, \quad \mathcal{H}_{\text{ex},\downarrow} = \begin{bmatrix} \mathcal{H}_{\text{ex},\downarrow\downarrow} & 0 \\ 0 & \mathcal{H}_{\text{ex},\uparrow\uparrow} \end{bmatrix}. \quad (5.2)$$

Note that the exchange matrices elements $\mathcal{H}_{\text{ex},\uparrow\uparrow}$ and $\mathcal{H}_{\text{ex},\downarrow\downarrow}$ are given in Eq. 4.7. Unlike a FM substrate in proximity to a MoTe₂ lattice, where the MEF on the Mo atoms has the same contribution because all the moments are parallel between them [35, 44, 36], here for the MoTe₂-AFM systems, the exchange field in Eq. 5.1 is onsite dependent; the exchange field for Mo atoms with up moments is $\mathcal{H}_{\text{ex},\uparrow}$, while the exchange field for Mo atoms with down moments is $\mathcal{H}_{\text{ex},\downarrow}$, as indicated in Eq. 5.2. As in the FM case, here we also consider the Rashba field arising from the broken symmetry generated by the substrate in the TMD lattice, we use the 3O Rashba coupling as in Eq. 4.7. All the parameters have been obtained from DFT calculations from a FM substrate [35], which in principle should be similar for a AFM substrate.

5.3 Zigzag-terminated Ribbons

We study zigzag-terminated MoTe₂ ribbons with 1600 Mo sites ($N = 40$ and $H = 40$) on the AFM1 substrate in Fig. 5.1. Zigzag ribbons on the AFM2 substrate show very similar behavior with respect to the MoTe₂-FM case showed in Chapter 4, so here we will discard the study of zigzag-terminated MoTe₂-AFM2 heterostructures.

There is an important distinction related with the geometrical and magnetic unit cells. As shown in Fig. 5.1(a) within the MoTe₂-AFM1 system, the magnetic cell accounting for the magnetic order (magenta rectangle) is twice the geometrical unit cell (black rectangle) along the zigzag direction. On the contrary, as shows Fig. 5.1(b), the magnetic and geometrical unit cells for the MoTe₂-AFM2 system are the same. Due to the 2 : 1 unit cells ratio in the MoTe₂-AFM1 system, the k space is folded. Consequently, the high symmetry points K and K' in reciprocal space are located at $k_x = -\pi/3a$ and $k'_x = \pi/3a$, respectively. The folded K and K' points are indicated as vertical dashed gray lines in the energy spectra of Fig. 5.2.

By means DFT calculations, a six-orbital TB model [160, 171] and through the

3OTB model [69], an intrinsic Rashba-type spin-splitting has been obtained along the edge modes of pristine zigzag-terminated ribbons, as is described in Subsection 2.4.1 by Eq. 2.21. Here the AFM1 substrate acting on the zigzag-terminated MoTe₂ ribbon, leads to an augmented Rashba-type spin-splitting $\Delta_R(k_x)$ [114], which is linear around $k_x = 0$. Similar Rashba-type spin-splitting has been obtained from a graphene layer on a Ni(111) substrate, seen by angle-resolved photoemission experiments [109]. Rashba-type spin-splittings around $k = 0$ have been theoretically predicted in diverse vertical heterostructures, where one of the constituent materials is a TMD monolayer. For instance, a 2D MoS₂ monolayer on a topological insulator Bi(111) [172]; the semiconductor TMD family on a 2D monolayer of GaX (X = S, Se, Te) [173]. In Janus (or polar) TMD monolayers also a Rashba-type spin-splitting around $k = 0$ is obtained due to the intrinsic electric field generated by the broken symmetry along the out-of-plane axis of the Janus 2D TMD [174, 175].

The Rashba splitting in zigzag-terminated TMDs has been associated to a combined effect of intrinsic symmetry broken at the edges and intrinsic SOC [69]. Under the combination of both effects, the effective 1D Hamiltonian for the chalcogen-edge mode in the energy dispersion can be written as [69]

$$H_{eff}(k') = \frac{k'^2}{2m^*} + \alpha k' s_z + C, \quad (5.3)$$

where $k' = k - \pi/a$, α is the Rashba strength, s_z is the z -Pauli matrix, and C is a constant. Notice that this Hamiltonian has the same linear dependence in momentum k as the Hamiltonian in Eq. 2.18 for 1D Rashba systems, but the second term changes sign, spin component $s_y \rightarrow s_z$, and the constant C here is associated with the eigenenergies from the lateral confinement potential [114]. The difference in the second term is related to the direction of the unit vector (electric field) in 1D Rashba systems. In Eq. 5.3 the unit vector is along the y direction, which is perpendicular to the zigzag direction, while in Eq. 2.18 the unit vector is along the z direction. However, both 1D Rashba Hamiltonians have the same eigenenergies. The low-energy spectra for the zigzag-terminated pristine TMD ribbons is symmetric around momentum $k = 0$ because of TRS [see Fig. 4.2(a)]. For the MoTe₂-AFM1 system we study here, augmented effective Rashba strength α and Rashba-type spin-splitting Δ_R along the edge modes, both associated with the extrinsic Rashba field (λ_R) from the AFM1 substrate on the ribbon are obtained, an effect not seen in the MoTe₂-AFM2 system, as will be discussed below.

In Fig. 5.2 we present the energy spectra for the MoTe₂-AFM1 zigzag heterostruc-

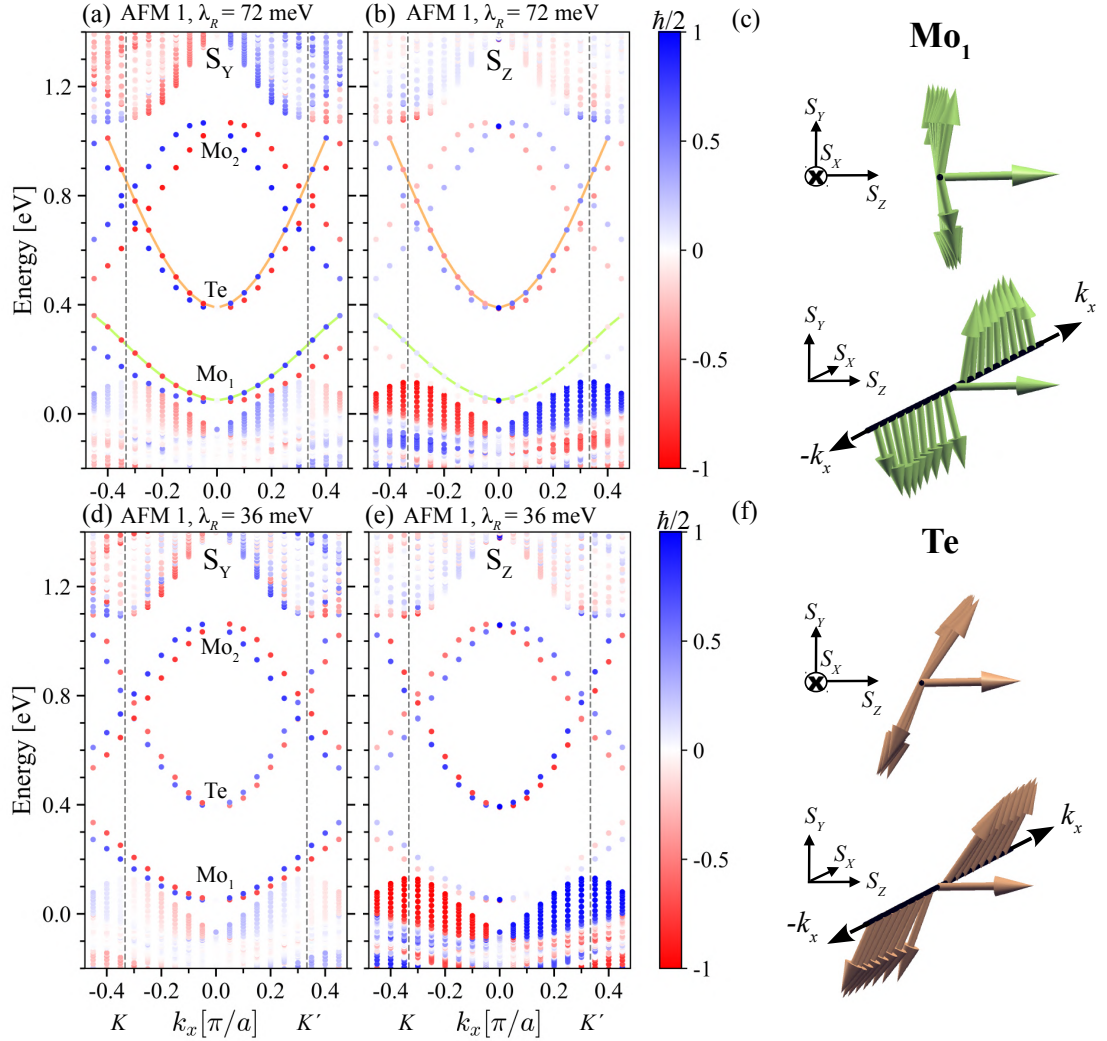


Figure 5.2: Spin projections of the energy spectrum for the zigzag-terminated ribbon in the MoTe₂-AFM1 system in Fig. 5.1(a). In (a) and (b) the extrinsic Rashba field λ_R is 100%, (d) and (e) the Rashba field is set to 50%. (a) and (d) stand for S_Y projection, (b) and (e) stand for the S_Z projection. Note that S_X projection vanishes due to the Rashba symmetry of the system. Mo_1 , Mo_2 and Te indicates the Rashba-type edge modes in the bulk midgap. Green (orange) solid lines indicate Mo_1 (Te) higher energy bands $E_+^{Mo_1}$ (E_+^{Te}), respectively. (c) and (f) are the spin expectation values (or spin projections) along the k_x momentum for the $E_+^{Mo_1}$ band (c) and E_+^{Te} band (f), indicated with solid lines in panels (a)-(b). Color bar indicates positive (negative) spin projection as blue (red) gradient.

ture, with two different values for the external Rashba field λ_R . Contrary to zigzag-

terminated ribbons on FM substrates, where the large intrinsic SOC competes with the exchange field from the FM substrate, leading to TRS breaking in the whole dispersion, and the exchange field conduct to a giant valley polarization in the 2D bulk [35], as well as to strongly spin-polarized edge modes [36], here the AFM exchange field leads to a zero valley polarization in the bulk, preserving TRS for the bulk as well as for the edges modes in the MoTe₂-AFM1 system. Clearly in the energy dispersion of Fig. 5.2 when the zigzag-terminated ribbon is in proximity to the AFM1 substrate, the whole dispersion is symmetric around $k_x = 0$ due to TRS.

When the AFM1 substrate enters into the Hamiltonian in Eq. 5.1, the exchange field at the edges has an effective vanishing net magnetic moment because the moments are antiparallel along the zigzag edges [see Fig. 5.1(a)]. As a result, the exchange field effectively induces a vanishing contribution to the edge dispersion, while the induced Rashba field modifies the Rashba splitting in the electronic dispersion, especially along the edge modes, as shown in the energy spectrum of Fig. 5.2. Here, three distinctive edge modes appear in the bulk midgap: Mo₁, Mo₂ and Te. Note that Mo₁ and Te edge modes have positive effective mass, while the Mo₂ edge mode has negative effective mass around $k_x = 0$. These edge modes correspond to states that are highly localized along the ribbon edges in real space, that is, the Mo₁ and Mo₂ edge modes reside on the Mo edge, while the Te edge mode reside on the Te edge. The electrons propagate along both, the Mo and the Te zigzag edges with momentum k_x and characteristic spin projection S_l ($l = X, Y, Z$). Each edge mode has two branches, $E_\lambda^{\text{Mo}_1}$ and $E_\lambda^{\text{Mo}_2}$ for the Mo edge, and E_λ^{Te} for the Te edge, where $\lambda = \pm 1$ labels chirality [114]. Around momentum $k_x = 0$, the E_+ (E_-) band for each edge mode correspond to the higher (lower) energy spin split band. We can see a linear tendency for the Rashba splitting $\Delta_R(k_x) = E_+(k_x) - E_-(k_x)$ at each edge mode along the momentum $|k_x|$. Note that the edge modes in this system (MoTe₂-AFM1) can be associated with 1D Rashba systems, as is described in Section 2.4.1 and by Eq. 5.3.

In panels (a) and (b) of Fig. 5.2 the energy spectra are show for the full Rashba field $\lambda_R = 72$ meV; in panels (d) and (e) we adjust the Rashba field to $\lambda_R = 36$ meV to study the tunability of the Rashba field. Different Rashba fields could be achieved through different surfaces of AFM substrates, or via gate fields for a given substrate-specific exchange field B_v [129, 121]. Because the edge modes in the MoTe₂-AFM1 system have a similar behavior as the edge modes in pristine zigzag-terminated MoTe₂ ribbons¹, we have calculated the effective Rashba parameters for the MoTe₂-AFM1 system

¹We have artificially folded the k_x -space in the free-standing zigzag-terminated MoTe₂ ribbon in Fig. 4.2(a) in order to compare the energy dispersions to the MoTe₂-AFM1 zigzag system.

with both Rashba fields $\lambda_R = 36$ meV and $\lambda_R = 72$ meV, as well as for the freestanding case, as shown in Table 5.1. The effective Rashba strength parameter α is obtained as $\Delta_R(k_x)/2k_x = \alpha$, we also calculated the effective Rashba splitting around the K' point for the Mo₁ and Te edge modes. We find that α for the Te edge mode agrees well with other chalcogen bands when the TMD ribbon is freestanding with zigzag-terminated edges [69]. We find α and $\Delta_R(k_x)/2$ increase with respect to the freestanding case because of the induced Rashba field λ_R from the AFM1 substrate, they have the same values for both edge modes when the Rashba field is $\lambda_R = 72$ meV. Interestingly, when $\lambda_R = 72$ meV, both α and $\Delta_R/2$ increase approximately 3 (3/2) times along the Mo₁ (Te) edge mode in relation to the freestanding case. On the other hand, when $\lambda_R = 36$ meV, both α and $\Delta/2$ increase approximately 3/2 times along the Mo₁ edge mode in relation to the Mo₁ edge mode of freestanding zigzag-terminated ribbon.

Accordingly to the Rashba effect and exchange interactions in proximitized vertical heterostructures where a linear Rashba-type spin-splitting in the energy dispersion around $k = 0$ is demonstrated [109], here we also find a linear behavior for the Rashba splitting around $k_x = 0$, most importantly, the Rashba splitting and the Rashba strength along the edge modes respond to the extrinsic Rashba field λ_R .

	α [eV Å/ π]		$\Delta_R/2$ [eV]	
	Mo ₁	Te	Mo ₁	Te
Free-standing, $\lambda_R = 0$	0.089	0.17	0.031	0.060
AFM1, $\lambda_R = 36$ meV	0.14	0.19	0.048	0.067
AFM1, $\lambda_R = 72$ meV	0.27	0.27	0.095	0.095

Table 5.1: Calculated effective Rashba parameters α and spin-splitting $\Delta_R(k_x)/2$ for momentum $k_x = 0.35 \pi/a$ (around the K' point) for the Mo₁ and Te edge modes projected along the MoTe₂ zigzag edges. The parameters are calculated for three cases, the freestanding MoTe₂ ribbon with $\lambda_R = 0$, and the MoTe₂-AFM1 system when $\lambda_R = 36$ meV and $\lambda_R = 72$ meV. α is obtained through a linear fitting in the curve $\Delta_R(k_x)/2k_x = \alpha$ in Fig. 5.2(a)-(b).

The spins play a crucial role in Rashba systems because they are linearly coupled to the momentum [113, 109], or effectively coupled to the sublattice pseudospin [108, 110, 111] (as is graphene) or orbital pseudospin [59, 35, 36] (as in TMDs). When the Rashba systems are coupled to the orbital pseudospin (as in the present case), small in-plane spin projection content arise when the 2D MoTe₂ monolayer is in proximity to a FM substrate [35], but considerable canted spins projections are found when the

energy dispersion is projected along the 1D zigzag edges [36]. In the AFM systems here, we also find electrons propagating with momentum k_x and significant projection along S_Y , as well as spin projection along S_Z along the zigzag edges.

The energy spectra in Fig. 5.2 shows the spin components content S_Y and S_Z (indicated by the blue-red gradient) for both $\lambda_R = 72$ meV and $\lambda_R = 36$ meV Rashba systems. We find a vanishing S_X component for both systems along the Mo and Te edge modes because here the Rashba field is along the y -direction of the ribbon. Figure 5.2(a)-(d) shows a significant S_Y projection due to the Rashba field is effectively stronger along the y -direction. We also note that S_Z projection increases in the valence bulk states in both systems, indicating that S_Z projection in the valence bulk states are less affected by the induced Rashba field λ_R , as shown in Fig. 5.2 panel (b) and (e). S_Z along the Mo₁ edge mode is nearly vanishing, while is significant along S_Y , independently of the Rashba field value, as shown in Fig. 5.2 panel (a) and (d). Along the Te edge mode, the S_Y projection increases and reduces along S_Z when $\lambda_R = 72$ meV, as it is clear in Fig. 5.2 panel (a) and (b). We can note slightly majority S_Z projection along the Te edge mode when $\lambda_R = 36$ meV. Along the Mo₂ edge mode, the S_Y projection increases, and reduces along S_Z when $\lambda_R = 36$ meV and $\lambda_R = 72$ meV.

To elucidate how the spins are projected along the momentum in these 1D Rashba systems, we have plotted the spin projections along k_x in the full Rashba field system ($\lambda_R = 72$ meV), $E_+^{\text{Mo}_1}$ band of the Mo₁ edge mode in Fig. 5.2(c) and E_+^{Te} band for the Te edge mode in Fig. 5.2(f). $E_+^{\text{Mo}_1}$ (E_+^{Te}) bands are indicated by green (orange) solid lines in Fig. 5.2 panel (a)-(b). The spin projection associated with the $E_+^{\text{Mo}_1}$ band are shown in panel (c) as green arrows. These spin projection are mostly S_Y polarized when $k_x \neq 0$ [notice the vanishing S_Z projection at $k_x = 0$ for all edge modes in panel (a)]. For right movers ($k_x > 0$), the spins along S_Y projection have $\simeq +\hbar/2$ expectation value, while for left movers, the spins along S_Y projection have $\simeq -\hbar/2$ expectation value. The opposite is true for the $E_-^{\text{Mo}_1}$ band. At $k_x = 0$ the full spin projection is along S_Z because the spin degeneracy due to SOC [69]. Higher in energy is the E_+^{Te} band, where the spin projections are shown in panel (f) as orange arrows. The spin projections along momentum $|k_x| \neq 0$ are polarized along both S_Y and S_Z , with $S_Y > S_Z$. For right movers, along S_Y , the expectation value are $\simeq +0.8 \hbar/2$, while for S_Z the expectation value is $\simeq +0.5 \hbar/2$. For left movers, along S_Y , the expectation value are $\simeq -0.8 \hbar/2$, while for S_Z are $\simeq -0.5 \hbar/2$. The opposite is true for the E_-^{Te} band. As the $E_{\pm}^{\text{Mo}_1}$ bands, the projection along S_Y vanishes at $k_x = 0$ for the E_{\pm}^{Te} band. If the Fermi level lies in the bulk midgap, the edge modes have equal number of left- and right-moving modes (two left- and two right-moving modes for each edge mode), with

opposite group velocity and opposite S_Y and S_Z projection around $k_x = 0$. The way of electrons propagate along the edge modes here, is similar to the bands obtained in the energy dispersion of graphene monolayer on Ni(111) [109], 2D monolayers of Janus TMDs [174, 175], MoS₂ 2D monolayer on Bi(111) [172], among others [173], where in all those works specially attention is given to the electron spin DoF.

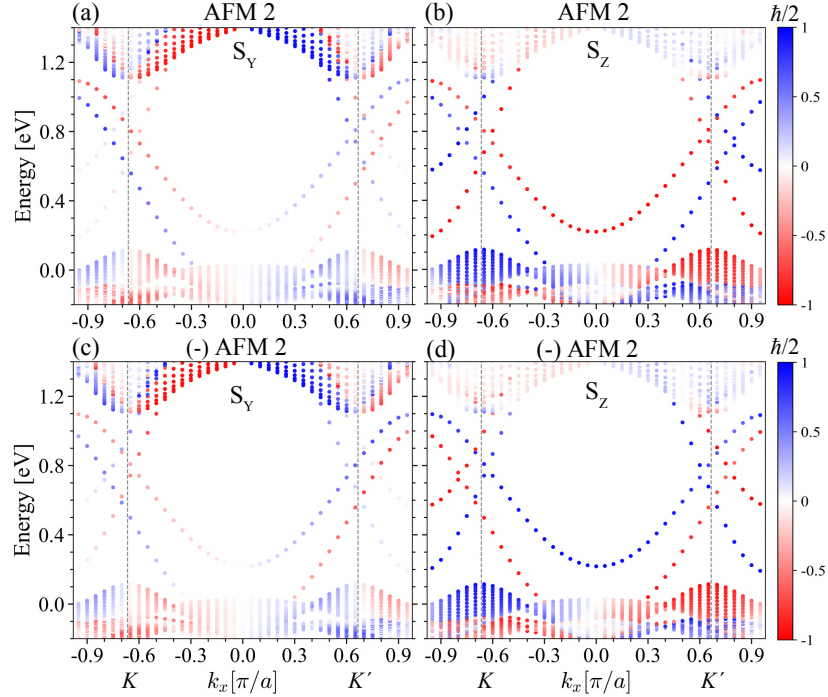


Figure 5.3: Spin projections of the energy spectrum for the zigzag-terminated ribbon in the MoTe₂-AFM2 system in Fig. 5.1(b). Panels (a)-(b) indicate S_Y - S_Z projections when the zigzag-terminated MoTe₂ ribbon is on the AFM2 substrate. The zigzag-terminated MoTe₂ ribbon is on the AFM2 substrate with the exchange field reversed in panels (c) and (d), which is indicated by the symbol (-).

5.4 Armchair-terminated Ribbons

Although TMD ribbons with zigzag terminations are mostly studied, it is demonstrated that experimentally realistic samples with armchair edges and interfaces in 2D TMD materials can be obtained [11, 12]. Diverse theoretical works which consider TMD ribbons with armchair edges have been done so far by means DFT, multiple-orbital TB models, and the 3OTB model [176, 177, 178, 68, 160, 161, 171, 179, 106, 180]. For instance, hydrogen [177, 178] and chalcogen passivation [178], the application of external

electric fields along the transverse direction of the armchair edges [178], lateral TMD heterostructures with armchair edges and interfaces [106, 180], and adatoms [179], generate diverse electronic effects in the energy dispersion of the ribbons. Most of these studies consider free-standing armchair ribbons, and only a few analyze the electronic effects in magnetic-proximitized structures with armchair edges of TMD semiconductors [171]. Here we describe the electronic properties of vertical heterostructures with armchair-terminated MoTe₂ ribbons in proximity to AFM substrates. The AFM substrates must fulfill the conditions depicted in Section 5.1.

To study armchair ribbons on AFM substrates we have considered two different ribbon sizes, noting the condition of net magnetic moment zero in the whole structure, the systems size are: (i) $N = 40$, $H = 42$ (1680 Mo sites), which we call $N40H42$ hereafter; (ii) $N = 41$, $H = 42$ (1722 Mo sites) is $N41H42$ hereafter; N (H) is the direction along the x (y)-axis, which is the width (length) of the armchair ribbon with PBC along y -axis, as schematically shown in Fig. 5.1.

Figure 5.1 shows the magnetization of the AFM substrates alternates between up and down along the armchair direction, as shown by blue (up) and red (down) arrows. In pristine armchair MoTe₂, as for the entire TMD armchair ribbon family, it is not possible to distinguish one edge from the other, because both edges have a combination of transition metal atoms and chalcogens. The armchair edges cannot be distinguished either when on a FM substrate, because all the moments are parallel between them. Here conversely, the armchair edges can be distinguished because the periodicity from the AFM substrate can be the same or different at opposite armchair edges, which depends on the ribbon width (N) [see Fig. 5.1]. The momentum space does not change when the armchair ribbons are on both AFM substrates because the geometric and magnetic unit cells have the same size along the y -axis. As we describe below, the energy-momentum dispersion shows N -dependent behavior when the armchair ribbon is on the AFM1 substrate and not on the AFM2 substrate. This effect is similar to parity laws studied in graphitic ribbons [181]. We first describe the case for the armchair ribbon $N40H42$ on the AFM2 substrate in Fig. 5.4 panels (c) and (f), because the energy spectrum of this system does not show dependence on the ribbon width.

As in the zigzag case, when the armchair ribbons are on the AFM substrates, the inversion symmetry is broken, allowing a Rashba field [108, 110, 59, 35, 111, 36] along the x -axis due to the symmetry of the structure. The Rashba field is in Eq. 4.7 and here also mixes the spin and orbital components. Figure 5.4 shows the dispersions for the armchair cases $N40H42$ on the AFM1 [panels (a) and (d)], $N41H42$ on AFM1 [panels (b) and (e)], and $N40H42$ on AFM2 [panels (c) and (f)], as well as their respective S_x

5.4 Armchair-terminated Ribbons

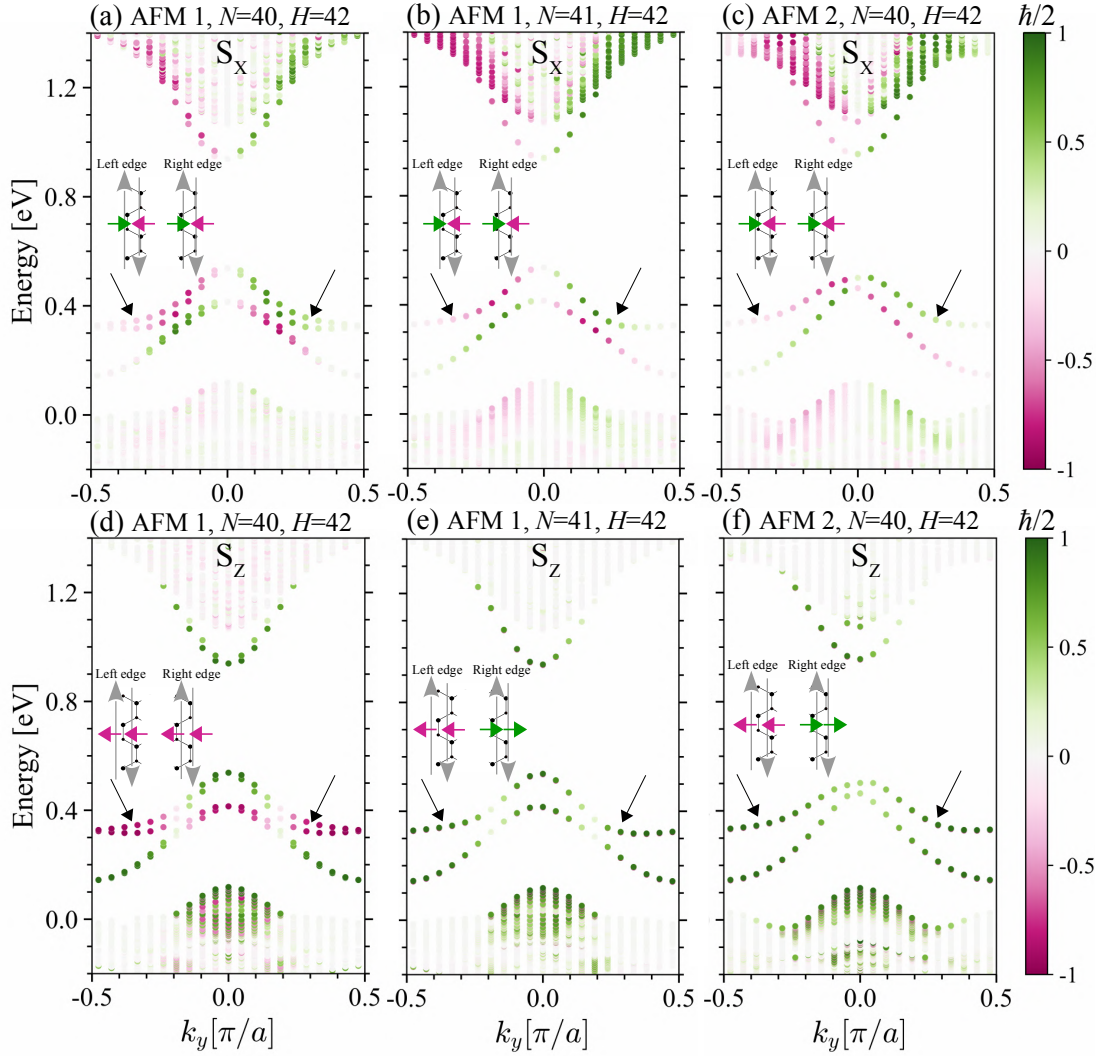


Figure 5.4: Spin projections of the energy spectrum for armchair-terminated ribbons when on the AFM1 and AFM2 substrates as indicated. In panels (a-c) the spin projections are along S_X , in panels (d-f) the spin projections are along S_Z . The inset in each panel schematizes the propagation for the electrons for the higher energy valence edge modes (indicated with black arrows) along both armchair edges, the left and the right (note in panel (d) the inset only shows the propagation for the negative S_Z band). Insets: up (down) vertical gray arrows indicate $+k_y$ ($-k_y$) momentum; green (magenta) arrows indicate positive (negative) S_X and S_Z spin projections on the armchair edges. Color bar indicates positive (negative) spin projection as green (magenta) gradient.

and S_Z spin components content, where green (magenta) refers to positive (negative) spin projection. For all the cases, there are in-gap edge modes, two of them close to

the valence bulk states, while other two with higher energy around the conduction bulk states. The spin projection is mainly along S_X in the conduction bulk states, while the valence bulk shows more S_Z projection content around $k_y = 0$, indicating the Rashba field is effectively weaker in the valence bulk states.

When the armchair ribbon is on the AFM2 substrate ($N40H42$ -AFM2 system), in panels (c) and (f), there are two pairs of edge modes lying in the bulk gap and non hybridized to the valence bulk states, creating a gap between them, other pair is hybridized to the conduction bulk states for momentum $|k_y| > 0.3 \pi/a$, and other pair is completely hybridized to the conduction bulk states. The eigenenergies of each pair of edge modes are degenerate, behind each edge mode there is other with the same S_X projection in panel (c). On the contrary, behind each edge mode there is another with opposite S_Z polarization in panel (f). By inspecting the wave functions projected in the ribbon real space, these edge modes are not mixed and propagate along the armchair edges with momentum k_y and characteristic spin as seen by the spin projections. The AFM substrate also breaks the energy degeneracy seen along the valence edge modes in free-standing armchair ribbons [a complete description for free-standing TMD armchair ribbons is in Appendix C].

In order to characterize the spins and the propagation direction seen in the energy spectrum, we have schematized the electron propagation along the left and the right armchair edges for in-gap valence edge modes with higher energy, as is indicated by black arrows in Fig. 5.4. In the insets, one can visualize the propagation direction for the electrons as up (down) gray arrows, which indicates $+k_y$ ($-k_y$) momentum; the spins are represented as green (magenta) shorter arrows, indicating positive (negative) spin projection. In panel (c), when the spins are along S_X , the electrons propagate with the same spin on opposite edges along the same direction. The opposite is true for the other pair of valence edge modes with lower energy along S_X . Similar behavior for the edge states is seen in a proximitized graphene ribbon when on a TMD substrate [122, 111]. In Ref. [111] the edge modes with this behavior are called *pseudohelical* states, which leads to a pure spin current (with zero charge current). Along S_Z , the propagation is different as electrons propagate with different projection on opposite edges along the same direction. This electron propagation polarizes the S_Z spins along the edges, namely, $+S_Z$ on the right-armchair edge and $-S_Z$ on the left-armchair edge for AFM2.

In panels (b) and (e) of Fig. 5.4 we show the S_X and S_Z spin projections for the armchair ribbon with size $N41H42$ when on the AFM1 substrate ($N41H42$ -AFM1 system). The energy dispersion exhibits similar behavior as the $N40H42$ -AFM2 system

[panels (c) and (f)]. Notice this is an intriguing behavior because the $N41H42$ -AFM1 system has one more Mo site along the x direction (width) of the ribbon; furthermore, the armchair ribbons are on different AFM substrates with different magnetic periodicity. However, both systems have the same periodicity along the armchair edges when the ribbon on AFM1 has odd number of Mo sites, as in the $N41H42$ -AFM1 case. The main difference between both systems is the energy dispersion around $k_y = 0$ for the valence edge modes. In panels (b) and (e) a larger gap between the valence edge modes around $k_y = 0$ is seen for the $N41H42$ -AFM1 system (odd) with respect to the $N40H42$ -AFM2 system (even) –notice that even and odd refers to the number of Mo sites across the width of the ribbon, regardless of the AFM substrate. In panel (e), another evident difference takes place around $|k_y| \simeq 0.2 \pi/a$, where S_Z projection is nearly vanishing and S_X is significant as shown in panel (b); this behavior is not apparent in the even system, panels (c) and (f). The electron propagation and spin projections along both armchair edges for the higher valence edge mode in panel (b) and (e) are of the same nature as the even system in panels (c) and (f), which would indicate a parity property associated with the even-odd number of Mo sites across the width of the armchair ribbon.

We have calculated the energy dispersion for the even case when the ribbon is on the AFM1 substrate ($N40H42$ -AFM1) in panels (a) and (d). Clearly here, the spin degeneracy is broken along the valence and conduction edge modes. The edge modes are non-degenerate (gapped for $|k_y| \simeq 0.3 \pi/a$) along S_X and S_Z and are in contrast to their odd counterpart ($N41H42$ -AFM1) in panels (b) and (e), where the edge modes are gapless. We also note an even-odd relation when the armchair ribbon is on the AFM1 substrate, here associated with the ribbon width and the magnetic periodicity along the armchair edges. We have checked that even-odd properties from the AFM2 substrates are not present. We tested armchair ribbons with odd number of Mo sites across the width on the AFM2 substrate ($N41H42$ -AFM2, not shown). The energy dispersion does not show appreciable differences with respect to even Mo sites in panels (c) and (f), especially for the edge modes that remain degenerate.

The propagation with S_X projection on the armchair edges for $N40H42$ -AFM1 (even) in panel (a) has the same nature as the $N41H42$ -AFM1 system (odd) in panel (b), but the projection along S_Z is different. However, as we mention above, the edge modes in the even (odd) system are gapped (gapless) when the armchair ribbon is on the AFM1 substrate. At $k_y = 0$, the wave functions projected in the ribbon real space show that the armchair edges are mixed. We also note the mixing for the edges around $|k_y| \simeq 0.3 \pi/a$, and $|k_y| \simeq 0.45 \pi/a$ as in the free-standing case. We have checked that

the edge mixing is only present in the even system ($N40H42$ -AFM1), and not in the odd systems when the ribbon is on either the AFM1 or AFM2 substrates. The electron propagation for the negative S_Z spin-projection band (as magenta color in the energy dispersion) is shown in the inset of panel (d). Here the electrons propagate with the same spins on opposite edges along the same (and opposite) direction, meaning that at this energy range, the electrons have degenerate copies with spin $-S_Z$ along both armchair edges.

5.5 Final Remarks

In this Chapter we have calculated the energy dispersion for zigzag and armchair MoTe_2 ribbons when they are deposited on AFM substrates. Both, zigzag and armchair magnetic proximitized ribbons have unique behavior as seen in the electronic spectrum when in comparison to their freestanding and/or FM proximitized counterpart. When the proximitized ribbons have zigzag edges, the Rashba-type spin-splitting Δ_R and the Rashba SOC strength α are three times augmented for the edge modes—which lies in the midgap region, associated with the external Rashba field from the AFM magnetic order of the substrate. Most importantly, these Rashba characteristics can be modified with the external Rashba field.

The electronic behavior along the edge modes when the proximitized ribbons have armchair edges is unusual. There are pseudohelical edge modes with S_X projection propagating along the armchair edges, which are decoupled from the bulk states. The electrons in these edge modes propagate with opposite S_X projection on opposite edges along opposite direction, carrying pure spin currents. On the other hand, electrons propagate with opposite S_Z projection on opposite edges along the same direction, giving rise to spin-polarized armchair edges states in AFM2. Another intriguing characteristic is found in AFM1-armchair edges, here the energy dispersion for the edge modes depends on the ribbon width. We find gapped edge modes when the ribbon width has even number of Mo sites, on the contrary, gapless edge modes are seen for odd number of Mo sites across the ribbon width. Within this unusual behavior we would expect a relation with parity laws seen in graphitic ribbons [181], and the edge states could be associated to topological states [182], which may be of relevant importance in the spintronics field.

Chapter 6

Conclusions

The availability of transition metal dichalcogenides samples nowadays appeal to efficient and reliable theoretical models to describe it and to predict functionalities. In this thesis, we theoretically have studied the electronic structure and magnetic proximity properties in functional vertically stacked TMD systems, as a fingerprint for charge and spin degrees of freedom behavior. A complete description of TMD materials and associated concepts, as well as the theoretical models used as a seed in our work are explained in Chapter 2.

In Chapter 3, we obtained the band structures for MoS₂ bilayers when molybdenum impurities are trapped in the interlayer region in diverse positions. The calculations are based on density functional theory, by including van der Waals interactions through the SIESTA method [81], as explained in Appendix A. The results show that Mo impurities are capable to modify the stable stacking seen in the pristine MoS₂ bilayer to another stacking type (within the same 2H phase), which accommodates the Mo impurities in hollow sites between the MoS₂ layers with high wave function weight around it. The stacking change is related to low energy midgap states arising from the Mo impurity bonding. A hybridization occurs for the impurity states with the MoS₂ layer states due to a small MoS₂-Mo_{imp}-MoS₂ distance in the bilayer. Furthermore, our results show larger interlayer distances, as well as larger bulk band gaps for other Mo-doped bilayers in comparison to the pristine case. Both effects can be associated with weaker interlayer coupling as seen in experiments, in which MoS₂ nanoparticles are located in the interlayer region of MoS₂ bilayers [31].

The generic existence of TMD edge states and ferromagnetic substrates that can be accessed in the laboratory suggest that they could provide exciting systems to explore proximity magnetism. In Chapter 4, we combined MoTe₂ zigzag-terminated nanoribbons with a FM substrate such as EuO. We model the combined structure with a

suitable magnetized three-orbital tight-binding model, which accounts for the induced magnetism from EuO.

The EuO substrate induces two different fields: magnetic exchange and Rashba, both directly related to the spin DoF. The MEF comes from the proximity-induced magnetic interactions, as described in Section 2.5, while the Rashba field is from the broken inversion symmetry that generates the EuO substrate on the MoTe₂ ribbons, as explained in Section 2.4.2. The effects of these fields, as well as the finite size effects of the ribbon, are manifested in the band structure responses of the MoTe₂-EuO hybrid system. The strong SOC from MoTe₂ competes with the exchange field, giving rise to in-gap spin-polarized edge modes with metallic character, while the bulk remains insulating. On the other hand, the Rashba field competes with the exchange field, providing an important figure of merit that determines the behavior of such systems. This means that depending on the strength of both induced fields, the whole electronic structure can be modified, most importantly, the spin-polarized edge modes are also affected. If the Fermi level lies in the midgap energy region of the bulk (by gating for example), the spin-polarized edge modes are localized along the one-dimensional zigzag edges of the ribbon, which carry spin information acquired by the proximity to the magnetic substrate and act as 1D conducting channels with tunable spin-polarized currents. The resulting edge spin currents can be canted at tunable directions, even in the presence of moderate concentration of defects, which can be an attractive property for experimentalists in the finite-sized/spintronics field. Current experiments in the area consider 2D TMD monolayers (without defined edges) as the nonmagnetic material in proximity to FM substrates and focusing in the valley DoF [17, 37, 38, 39, 40]. Here with our work, we can expect these hybrid finite-size FM structures could be used as robust tunable spin filters for use in diverse applications.

The magnetic proximity effect can also appear in antiferromagnetic combined systems [121]. In Chapter 5 we complement the FM study with MoTe₂ nanoribbons deposited on AFM substrates (with AFM1 and AFM2 labeling different magnetic orders), forming several vertical heterostructures of the type MoTe₂-AFM. We model the systems by considering an adapted-magnetized 3OTB model, where the exchange Hamiltonian term is adapted by alternating the direction of the magnetic moments between individual sites, while the Rashba field is the same as in the FM case, as described in Section 5.2.

Our results reveal remarkable differences depending on: the AFM order in the substrate together with the edge-termination (zigzag/armchair), and the width for armchair ribbons on AFM substrates. The band structure for zigzag-terminated MoTe₂

ribbons on the AFM1 substrate is similar to the free-standing TMD zigzag ribbon case—as both systems are time-reversal invariant and the edge modes possess Rashba SOC—, but the former exhibiting enhanced parameters such as Rashba-type SOC and spin-splitting along the edge modes, while the bulk remains insulating. More interestingly, the Rashba-type parameters respond to the interfacial Rashba field from the AFM substrate. We have characterized the propagation for some edge modes in the midgap region, where we see specific spin polarization direction (mostly perpendicular to the propagation direction) for right movers, while reversing for left movers. This behavior is typical for Rashba systems, as explained in Sections 2.4 and 2.4.1 and Chapter 5. We note our findings for zigzag MoTe₂ ribbons on AFM substrates are in close relation with other 2D vertical heterostructures forming Rashba systems, such as in the experiment of graphene-Ni(111) [109], and theoretically seen in MoS₂-Bi(111) [172] and GaX-MX₂ (M=Mo, W; X=S, Se, Te) [173].

Armchair nanoribbons on AFM substrates are of special interest because the AFM substrates break the spin degeneracy seen in pristine armchair TMD ribbons (as those described in Appendix C); and the edge modes exhibit width dependence, both effects are manifested along the edge modes of the band structure. When the armchair ribbons are on the AFM1 substrate with even number of metal sites across the length, there arise gapped edge modes. On the contrary, when the number of metal sites is odd, there are gapless edge modes. The propagation characterization shows the edge modes carry pure spin currents (with zero charge currents) with S_X spin projection along the armchair edges, independently of the AFM substrate and the ribbon width. Along S_Z , the propagation varies with both, the AFM substrate and the ribbon width. All these unusual behaviors are probably related to parity laws, as seen in graphitic ribbons [181] and to topological states [182].

The proposed systems we study in this thesis would bring new functionalities and versatile applications in low-dimensional solid-state systems, apart from providing interesting scenarios to explore spin-polarized vertical structures, proximity magnetism, and the role of electronic interactions in 1D systems with complex spin texture. We conclude our vertically stacked TMD-based structures lie on reliable and realistic modelling, which could be used as building blocks in the construction of novel devices with diverse applications in electronics and spintronics fields. [183], [184], [185] [186] [187] [188] [189]

References

- [1] A. H. Castro Neto and K. S. Novoselov, “Two-dimensional crystals: beyond graphene,” *Mater. Express*, vol. 1, no. 1, pp. 10–17, 2011.
- [2] K. S. Novoselov, A. K. Geim, S. V. Morozov, D. Jiang, Y. Zhang, S. V. Dubonos, I. V. Grigorieva, and A. A. Firsov, “Electric field effect in atomically thin carbon films,” *Science*, vol. 306, no. 5696, pp. 666–669, 2004.
- [3] K. S. Novoselov, D. Jiang, F. Schedin, T. J. Booth, V. V. Khotkevich, S. V. Morozov, and A. K. Geim, “Two-dimensional atomic crystals,” *Proc. Natl. Acad. Sci. U.S.A.*, vol. 102, no. 30, pp. 10451–10453, 2005.
- [4] B. Radisavljevic, A. Radenovic, J. Brivio, V. Giacometti, and A. Kis, “Single-layer MoS₂ transistors,” *Nat. Nanotechnol.*, vol. 6, no. 3, pp. 147–50, 2011.
- [5] B. W. Baugher, H. O. Churchill, Y. Yang, and P. Jarillo-Herrero, “Intrinsic electronic transport properties of high-quality monolayer and bilayer MoS₂,” *Nano Lett.*, vol. 13, no. 9, pp. 4212–4216, 2013.
- [6] D. Sarkar, X. Xie, W. Liu, W. Cao, J. Kang, Y. Gong, S. Kraemer, P. M. Ajayan, and K. Banerjee, “A subthermionic tunnel field-effect transistor with an atomically thin channel,” *Nature*, vol. 526, no. 7571, p. 91, 2015.
- [7] M. Chhowalla, H. S. Shin, G. Eda, L.-J. Li, K. P. Loh, and H. Zhang, “The chemistry of two-dimensional layered transition metal dichalcogenide nanosheets,” *Nat. Chem.*, vol. 5, no. 4, pp. 263–275, 2013.
- [8] K. Liu, L. Zhang, T. Cao, C. Jin, D. Qiu, Q. Zhou, A. Zettl, P. Yang, S. G. Louie, and F. Wang, “Evolution of interlayer coupling in twisted molybdenum disulfide bilayers,” *Nat. Commun.*, vol. 5, p. 4966, 2014.
- [9] F. Cheng, H. Xu, W. Xu, P. Zhou, J. Martin, and K. P. Loh, “Controlled growth

- of 1D MoSe₂ nanoribbons with spatially modulated edge states,” *Nano Lett.*, vol. 17, no. 2, pp. 1116–1120, 2017.
- [10] Q. Chen, H. Li, W. Xu, S. Wang, H. Sawada, C. S. Allen, A. I. Kirkland, J. C. Grossman, and J. H. Warner, “Atomically flat zigzag edges in monolayer MoS₂ by thermal annealing,” *Nano Lett.*, vol. 17, no. 9, pp. 5502–5507, 2017.
- [11] Y. Gong, J. Lin, X. Wang, G. Shi, S. Lei, Z. Lin, X. Zou, G. Ye, R. Vajtai, B. I. Yakobson, *et al.*, “Vertical and in-plane heterostructures from WS₂/MoS₂ monolayers,” *Nat. Mater.*, vol. 13, no. 12, p. 1135, 2014.
- [12] X.-Q. Zhang, C.-H. Lin, Y.-W. Tseng, K.-H. Huang, and Y.-H. Lee, “Synthesis of lateral heterostructures of semiconducting atomic layers,” *Nano Lett.*, vol. 15, no. 1, pp. 410–415, 2014.
- [13] M. V. Bollinger, J. V. Lauritsen, K. W. Jacobsen, J. K. Nørskov, S. Helveg, and F. Besenbacher, “One-dimensional metallic edge states in MoS₂,” *Phys. Rev. Lett.*, vol. 87, no. 19, p. 196803, 2001.
- [14] L. Liu, Z. Ge, C. Yan, A. D. Moghadam, M. Weinert, and L. Li, “Termination-dependent edge states of MBE-grown WSe₂,” *Phys. Rev. B*, vol. 98, no. 23, p. 235304, 2018.
- [15] J. Huang, H. Liu, B. Jin, M. Liu, Q. Zhang, L. Luo, S. Chu, S. Chu, and R. Peng, “Large-area snow-like MoSe₂ monolayers: synthesis, growth mechanism, and efficient electrocatalyst application,” *Nanotechnology*, vol. 28, no. 27, p. 275704, 2017.
- [16] Y. Yu, G. Wang, Y. Tan, N. Wu, X.-A. Zhang, and S. Qin, “Phase-controlled growth of one-dimensional Mo₆Te₆ nanowires and two-dimensional MoTe₂ ultra-thin films heterostructures,” *Nano Lett.*, vol. 18, no. 2, pp. 675–681, 2017.
- [17] C. Zhao, T. Norden, P. Zhang, P. Zhao, Y. Cheng, F. Sun, J. P. Parry, P. Taheri, J. Wang, Y. Yang, T. Scrace, K. Kang, S. Yang, G.-x. Miao, R. Sabirianov, G. Kioseoglou, W. Huang, A. Petrou, and H. Zeng, “Enhanced valley splitting in monolayer WSe₂ due to magnetic exchange field,” *Nat. Nanotechnol.*, vol. 12, no. 8, p. 757, 2017.
- [18] K. F. Mak, C. Lee, J. Hone, J. Shan, and T. F. Heinz, “Atomically thin MoS₂: A new direct-gap semiconductor,” *Phys. Rev. Lett.*, vol. 105, p. 136805, Sep 2010.

-
- [19] A. Castellanos-Gomez, M. Poot, G. A. Steele, H. S. J. van der Zant, N. Agraït, and G. Rubio-Bollinger, “Elastic properties of freely suspended MoS₂ nanosheets,” *Adv. Mater.*, vol. 24, no. 6, pp. 772–775, 2012.
- [20] X. Zhao, D. Fu, Z. Ding, Y.-Y. Zhang, D. Wan, S. J. R. Tan, Z. Chen, K. Leng, J. Dan, W. Fu, D. Geng, P. Song, Y. Du, T. Venkatesan, S. T. Pantelides, S. J. Pennycook, W. Zhou, and K. P. Loh, “Mo-terminated edge reconstructions in nanoporous molybdenum disulfide film,” *Nano Lett.*, vol. 18, no. 1, pp. 482–490, 2018.
- [21] H. Zhu, Q. Wang, L. Cheng, R. Addou, J. Kim, M. J. Kim, and R. M. Wallace, “Defects and surface structural stability of MoTe₂ under vacuum annealing,” *ACS nano*, vol. 11, no. 11, pp. 11005–11014, 2017.
- [22] M. Precner, T. Polaković, Q. Qiao, D. Trainer, A. Putilov, C. Di Giorgio, I. Cone, Y. Zhu, X. Xi, M. Iavarone, *et al.*, “Evolution of metastable defects and its effect on the electronic properties of MoS₂ films,” *Sci. Rep.*, vol. 8, 2018.
- [23] P. M. Coelho, H.-P. Komsa, H. C. Diaz, Y. Ma, A. V. Krasheninnikov, and M. Batzill, “Post-synthesis modifications of two-dimensional MoSe₂ or MoTe₂ by incorporation of excess metal atoms into the crystal structure,” *ACS Nano*, vol. 12, no. 4, pp. 3975–3984, 2018.
- [24] F. Zhang, Y. Wang, C. Erb, K. Wang, P. Moradifar, V. Crespi, and N. Alem, “Full orientation control of epitaxial MoS₂ on hBN assisted by substrate defects,” *arXiv e-prints*, p. arXiv:1801.00487, Jan 2018.
- [25] A. Splendiani, L. Sun, Y. Zhang, T. Li, J. Kim, C.-Y. Chim, G. Galli, and F. Wang, “Emerging photoluminescence in monolayer MoS₂,” *Nano Lett.*, vol. 10, no. 4, pp. 1271–1275, 2010.
- [26] D. Xiao, G.-B. Liu, W. Feng, X. Xu, and W. Yao, “Coupled spin and valley physics in monolayers of MoS₂ and other group-VI dichalcogenides,” *Phys. Rev. Lett.*, vol. 108, p. 196802, May 2012.
- [27] G.-B. Liu, D. Xiao, Y. Yao, X. Xu, and W. Yao, “Electronic structures and theoretical modelling of two-dimensional group-VIB transition metal dichalcogenides,” *Chem. Soc. Rev.*, vol. 44, no. 9, pp. 2643–2663, 2015.

-
- [28] Z. Gong, G.-B. Liu, H. Yu, D. Xiao, X. Cui, X. Xu, and W. Yao, “Magnetoelectric effects and valley-controlled spin quantum gates in transition metal dichalcogenide bilayers,” *Nat. Commun.*, vol. 4, p. 2053, 2013.
- [29] X. Xu, W. Yao, D. Xiao, and T. F. Heinz, “Spin and pseudospins in layered transition metal dichalcogenides,” *Nat. Phys.*, vol. 10, no. 5, p. 343, 2014.
- [30] J. He, K. Hummer, and C. Franchini, “Stacking effects on the electronic and optical properties of bilayer transition metal dichalcogenides MoS₂, MoSe₂, WS₂, and WSe₂,” *Phys. Rev. B*, vol. 89, no. 7, p. 075409, 2014.
- [31] W. Zhou, C. Yuan, A. Hong, X. Luo, and W. Lei, “Laminated bilayer MoS₂ with weak interlayer coupling,” *Nanoscale*, vol. 10, pp. 1145–1152, 2018.
- [32] I. Žutić, J. Fabian, and S. D. Sarma, “Spintronics: Fundamentals and applications,” *Rev. Mod. Phys.*, vol. 76, no. 2, p. 323, 2004.
- [33] J. Sinova, D. Culcer, Q. Niu, N. A. Sinitsyn, T. Jungwirth, and A. H. MacDonald, “Universal intrinsic spin Hall effect,” *Phys. Rev. Lett.*, vol. 92, no. 12, p. 126603, 2004.
- [34] S. Datta, “How we proposed the spin transistor,” *Nature Electronics*, vol. 1, no. 11, p. 604, 2018.
- [35] J. Qi, X. Li, Q. Niu, J. Feng, *et al.*, “Giant and tunable valley degeneracy splitting in MoTe₂,” *Phys. Rev. B(R)*, vol. 92, no. 12, p. 121403, 2015.
- [36] N. Cortés, O. Ávalos-Ovando, L. Rosales, P. Orellana, and S. Ulloa, “Tunable spin-polarized edge currents in proximitized transition metal dichalcogenides,” *Phys. Rev. Lett.*, vol. 122, no. 8, p. 086401, 2019.
- [37] D. Zhong, K. L. Seyler, X. Linpeng, R. Cheng, N. Sivadas, B. Huang, E. Schmidgall, T. Taniguchi, K. Watanabe, M. A. McGuire, W. Yao, D. Xiao, K.-M. C. Fu, and X. Xu, “Van der waals engineering of ferromagnetic semiconductor heterostructures for spin and valleytronics,” *Sci. Adv.*, vol. 3, no. 5, p. e1603113, 2017.
- [38] K. L. Seyler, D. Zhong, B. Huang, X. Linpeng, N. P. Wilson, T. Taniguchi, K. Watanabe, W. Yao, D. Xiao, M. A. McGuire, K.-M. C. Fu, and X. Xu, “Valley manipulation by optically tuning the magnetic proximity effect in WSe₂/CrI₃ heterostructures,” *Nano Lett.*, vol. 18, no. 6, pp. 3823–3828, 2018.

-
- [39] C. Zou, C. Cong, J. Shang, C. Zhao, M. Eginligil, L. Wu, Y. Chen, H. Zhang, S. Feng, J. Zhang, *et al.*, “Probing magnetic-proximity-effect enlarged valley splitting in monolayer WSe₂ by photoluminescence,” *Nano Res.*, vol. 11, no. 12, pp. 6252–6259, 2018.
- [40] T. Norden, C. Zhao, P. Zhang, R. Sabirianov, A. Petrou, and H. Zeng, “Giant valley splitting in monolayer WS₂ by magnetic proximity effect,” *arXiv preprint arXiv:1902.05910*, 2019.
- [41] G. Aivazian, Z. Gong, A. M. Jones, R.-L. Chu, J. Yan, D. G. Mandrus, C. Zhang, D. Cobden, W. Yao, and X. Xu, “Magnetic control of valley pseudospin in monolayer WSe₂,” *Nat. Phys.*, vol. 11, no. 2, p. 148, 2015.
- [42] A. Srivastava, M. Sidler, A. V. Allain, D. S. Lembke, A. Kis, and A. Imamoglu, “Valley zeeman effect in elementary optical excitations of monolayer WSe₂,” *Nat. Phys.*, vol. 11, no. 2, p. 141, 2015.
- [43] X.-X. Zhang, Y. Lai, E. Dohner, S. Moon, T. Taniguchi, K. Watanabe, D. Smirnov, and T. F. Heinz, “Zeeman-induced valley-sensitive photocurrent in monolayer MoS₂,” *Phys. Rev. Lett.*, vol. 122, no. 12, p. 127401, 2019.
- [44] Q. Zhang, S. A. Yang, W. Mi, Y. Cheng, and U. Schwingenschlögl, “Large spin-valley polarization in monolayer MoTe₂ on top of EuO(111),” *Adv. Mat.*, vol. 28, no. 5, pp. 959–966, 2016.
- [45] Q. H. Wang, K. Kalantar-Zadeh, A. Kis, J. N. Coleman, and M. S. Strano, “Electronics and optoelectronics of two-dimensional transition metal dichalcogenides,” *Nat. Nanotechnol.*, vol. 7, no. 11, p. 699, 2012.
- [46] L. A. Walsh, R. Addou, R. M. Wallace, and C. L. Hinkle, “Molecular beam epitaxy of transition metal dichalcogenides,” in *Molecular Beam Epitaxy*, pp. 515–531, Elsevier, 2018.
- [47] A. C. Neto, “Charge density wave, superconductivity, and anomalous metallic behavior in 2D transition metal dichalcogenides,” *Phys. Rev. Lett.*, vol. 86, no. 19, p. 4382, 2001.
- [48] E. Gibney, “The super materials that could trump graphene,” *Nat. News*, vol. 522, no. 7556, p. 274, 2015.

-
- [49] I. Song, C. Park, and H. C. Choi, “Synthesis and properties of molybdenum disulphide: from bulk to atomic layers,” *RSC Adv.*, vol. 5, no. 10, pp. 7495–7514, 2015.
- [50] M. Samadi, N. Sarikhani, M. Zirak, H. Zhang, H.-L. Zhang, and A. Z. Moshfegh, “Group 6 transition metal dichalcogenide nanomaterials: synthesis, applications and future perspectives,” *Nanoscale Horiz.*, vol. 3, no. 2, pp. 90–204, 2018.
- [51] R. Roldán, J. A. Silva-Guillén, M. P. López-Sancho, F. Guinea, E. Cappelluti, and P. Ordejón, “Electronic properties of single-layer and multilayer transition metal dichalcogenides MX_2 (M=Mo, W and X=S, Se),” *Ann. Phys. (Berlin)*, vol. 526, no. 9-10, pp. 347–357, 2014.
- [52] H. C. Diaz, Y. Ma, R. Chaghi, and M. Batzill, “High density of (pseudo) periodic twin-grain boundaries in molecular beam epitaxy-grown van der waals heterostructure: $\text{MoTe}_2/\text{MoS}_2$,” *Appl. Phys. Lett.*, vol. 108, no. 19, p. 191606, 2016.
- [53] Z. Zhu, Y. Cheng, and U. Schwingenschlögl, “Giant spin-orbit-induced spin splitting in two-dimensional transition-metal dichalcogenide semiconductors,” *Phys. Rev. B*, vol. 84, no. 15, p. 153402, 2011.
- [54] N. Alidoust, G. Bian, S.-Y. Xu, R. Sankar, M. Neupane, C. Liu, I. Belopolski, D.-X. Qu, J. D. Denlinger, F.-C. Chou, *et al.*, “Observation of monolayer valence band spin-orbit effect and induced quantum well states in MoX_2 ,” *Nat. Commun.*, vol. 5, p. 4673, 2014.
- [55] X. Qian, J. Liu, L. Fu, and J. Li, “Quantum spin Hall effect in two-dimensional transition metal dichalcogenides,” *Science*, vol. 346, no. 6215, pp. 1344–1347, 2014.
- [56] S. Tang, C. Zhang, D. Wong, Z. Pedramrazi, H.-Z. Tsai, C. Jia, B. Moritz, M. Claassen, H. Ryu, S. Kahn, J. Jiang, H. Yan, M. Hashimoto, D. Lu, R. G. Moore, C.-C. Hwang, C. Hwang, Z. Hussain, Y. Chen, M. M. Ugeda, Z. Liu, X. Xie, T. P. Devereaux, M. F. Crommie, S.-K. Mo, and Z.-X. Shen, “Quantum spin Hall state in monolayer $1\text{T}'\text{-WTe}_2$,” *Nat. Phys.*, vol. 13, no. 7, p. 683, 2017.
- [57] V. Perebeinos, “Metal dichalcogenides: Two dimensions and one photon,” *Nat. Nanotechnol.*, vol. 10, no. 6, p. 485, 2015.
- [58] S. Barja, S. Wickenburg, Z.-F. Liu, Y. Zhang, H. Ryu, M. M. Ugeda, Z. Hussain, Z.-X. Shen, S.-K. Mo, E. Wong, M. B. Salmeron, F. Wang, M. F. Crommie, D. F.

- Ogletree, J. B. Neaton, and A. Weber-Bargioni, “Charge density wave order in 1D mirror twin boundaries of single-layer MoSe₂,” *Nat. Phys.*, vol. 12, no. 8, pp. 751–756, 2016.
- [59] H. Ochoa and R. Roldán, “Spin-orbit-mediated spin relaxation in monolayer MoS₂,” *Phys. Rev. B*, vol. 87, no. 24, p. 245421, 2013.
- [60] G.-B. Liu, W.-Y. Shan, Y. Yao, W. Yao, and D. Xiao, “Three-band tight-binding model for monolayers of group-VIB transition metal dichalcogenides,” *Phys. Rev. B*, vol. 88, p. 085433, Aug 2013.
- [61] K. F. Mak, D. Xiao, and J. Shan, “Light–valley interactions in 2D semiconductors,” *Nat. Photonics*, vol. 12, no. 8, p. 451, 2018.
- [62] B. T. Zhou, K. Taguchi, Y. Kawaguchi, Y. Tanaka, and K. Law, “Spin-orbit coupling induced valley hall effects in transition-metal dichalcogenides,” *Comm. Phys.*, vol. 2, no. 1, p. 26, 2019.
- [63] C. Safeer, J. Ingla-Aynés, F. Herling, J. H. Garcia, M. Vila, N. Ontoso, M. R. Calvo, S. Roche, L. E. Hueso, and F. Casanova, “Room-temperature spin hall effect in Graphene/MoS₂ van der waals heterostructures,” *Nano Lett.*, vol. 19, no. 2, pp. 1074–1082, 2019.
- [64] K. F. Mak, K. L. McGill, J. Park, and P. L. McEuen, “The valley Hall effect in MoS₂ transistors,” *Science*, vol. 344, no. 6191, pp. 1489–1492, 2014.
- [65] A. M. Van Der Zande, P. Y. Huang, D. A. Chenet, T. C. Berkelbach, Y. You, G.-H. Lee, T. F. Heinz, D. R. Reichman, D. A. Muller, and J. C. Hone, “Grains and grain boundaries in highly crystalline monolayer molybdenum disulphide,” *Nat. Mater.*, vol. 12, no. 6, p. 554, 2013.
- [66] X. Wang, H. Feng, Y. Wu, and L. Jiao, “Controlled synthesis of highly crystalline MoS₂ flakes by chemical vapor deposition,” *J. Am. Chem. Soc.*, vol. 135, no. 14, pp. 5304–5307, 2013.
- [67] K. Vasu, S. S. Yamijala, A. Zak, K. Gopalakrishnan, S. K. Pati, and C. Rao, “Clean WS₂ and MoS₂ nanoribbons generated by laser-induced unzipping of the nanotubes,” *Small*, vol. 11, no. 32, pp. 3916–3920, 2015.
- [68] M. Gibertini and N. Marzari, “Emergence of one-dimensional wires of free carriers in transition-metal-dichalcogenide nanostructures,” *Nano Lett.*, vol. 15, no. 9, pp. 6229–6238, 2015.

-
- [69] R.-L. Chu, G.-B. Liu, W. Yao, X. Xu, D. Xiao, and C. Zhang, “Spin-orbit-coupled quantum wires and majorana fermions on zigzag edges of monolayer transition-metal dichalcogenides,” *Phys. Rev. B*, vol. 89, p. 155317, Apr 2014.
- [70] F. Khoeini, K. Shakouri, and F. M. Peeters, “Peculiar half-metallic state in zigzag nanoribbons of MoS₂: Spin filtering,” *Phys. Rev. B*, vol. 94, no. 12, p. 125412, 2016.
- [71] E. Razzoli, T. Jaouen, M.-L. Mottas, B. Hildebrand, G. Monney, A. Pisoni, S. Muff, M. Fanciulli, N. C. Plumb, V. A. Rogalev, V. N. Strocov, J. Mesot, M. J. Shi, J. H. Dil, H. K. B. Beck, and P. Aebi, “Selective probing of hidden spin-polarized states in inversion-symmetric bulk MoS₂,” *Phys. Rev. Lett.*, vol. 118 8, p. 086402, 2017.
- [72] X. Zhao, S. Ning, W. Fu, S. J. Pennycook, and K. P. Loh, “Differentiating polymorphs in molybdenum disulfide via electron microscopy,” *Adv. Mat.*, vol. 30, no. 47, p. 1802397, 2018.
- [73] S. Wu, J. S. Ross, G.-B. Liu, G. Aivazian, A. Jones, Z. Fei, W. Zhu, D. Xiao, W. Yao, D. Cobden, *et al.*, “Electrical tuning of valley magnetic moment through symmetry control in bilayer MoS₂,” *Nat. Phys.*, vol. 9, no. 3, pp. 149–153, 2013.
- [74] J. Lee, K. F. Mak, and J. Shan, “Electrical control of the valley Hall effect in bilayer MoS₂ transistors,” *Nat. Nanotechnol.*, vol. 11, no. 5, p. 421, 2016.
- [75] W. Jin, P.-C. Yeh, N. Zaki, D. Zhang, J. T. Sadowski, A. Al-Mahboob, A. M. van Der Zande, D. A. Chenet, J. I. Dadap, I. P. Herman, *et al.*, “Direct measurement of the thickness-dependent electronic band structure of MoS₂ using angle-resolved photoemission spectroscopy,” *Phys. Rev. Lett.*, vol. 111, no. 10, p. 106801, 2013.
- [76] S. Yang, J. Kang, Q. Yue, and K. Yao, “Vapor phase growth and imaging stacking order of bilayer molybdenum disulfide,” *J. Phys. Chem. C*, vol. 118, no. 17, pp. 9203–9208, 2014.
- [77] N. Cortés, L. Rosales, P. A. Orellana, A. Ayuela, and J. W. González, “Stacking change in MoS₂ bilayers induced by interstitial Mo impurities,” *Sci. Rep.*, vol. 8, no. 1, p. 2143, 2018.
- [78] T. Cusati, A. Fortunelli, G. Fiori, and G. Iannaccone, “Stacking and interlayer electron transport in MoS₂,” *Phys. Rev. B*, vol. 98, no. 11, p. 115403, 2018.

-
- [79] A. Kormányos, V. Zólyomi, V. I. Fal'ko, and G. Burkard, "Tunable berry curvature and valley and spin hall effect in bilayer MoS₂," *Phys. Rev. B*, vol. 98, no. 3, p. 035408, 2018.
- [80] M. H. Naik and M. Jain, "Ultraflatbands and shear solitons in Moiré patterns of twisted bilayer transition metal dichalcogenides," *Phys. Rev. Lett.*, vol. 121, no. 26, p. 266401, 2018.
- [81] J. M. Soler, E. Artacho, J. D. Gale, A. García, J. Junquera, P. Ordejón, and D. Sánchez-Portal, "The SIESTA method for ab initio order-N materials simulation," *J. Phys.: Condens. Matter*, vol. 14, no. 11, p. 2745, 2002.
- [82] J. Yan, J. Xia, X. Wang, L. Liu, J.-L. Kuo, B. K. Tay, S. Chen, W. Zhou, Z. Liu, and Z. X. Shen, "Stacking-dependent interlayer coupling in trilayer MoS₂ with broken inversion symmetry," *Nano Lett.*, vol. 15, no. 12, pp. 8155–8161, 2015.
- [83] J. Xia, J. Yan, and Z. X. Shen, "Transition metal dichalcogenides: structural, optical and electronic property tuning via thickness and stacking," *FlatChem*, vol. 4, pp. 1–19, 2017.
- [84] J. Xia, Q. Zeng, J. Zhou, W. Zhou, Q. Zhang, J. Yan, Z. Liu, and Z. X. Shen, "Current rectification and asymmetric photoresponse in MoS₂ stacking-induced homojunctions," *2D Materials*, vol. 4, no. 3, p. 035011, 2017.
- [85] K. Kośmider and J. Fernández-Rossier, "Electronic properties of the MoS₂-WS₂ heterojunction," *Phys. Rev. B*, vol. 87, no. 7, p. 075451, 2013.
- [86] K. Kośmider, J. W. González, and J. Fernández-Rossier, "Large spin splitting in the conduction band of transition metal dichalcogenide monolayers," *Phys. Rev. B*, vol. 88, p. 245436, Dec 2013.
- [87] A. Yan, W. Chen, C. Ophus, J. Ciston, Y. Lin, K. Persson, and A. Zettl, "Identifying different stacking sequences in few-layer CVD-grown MoS₂ by low-energy atomic-resolution scanning transmission electron microscopy," *Phys. Rev. B*, vol. 93, no. 4, p. 041420, 2016.
- [88] H. Yuan, Z. Liu, G. Xu, B. Zhou, S. Wu, D. Dumcenco, K. Yan, Y. Zhang, S.-K. Mo, P. Dudin, *et al.*, "Evolution of the valley position in bulk transition-metal chalcogenides and their monolayer limit," *Nano Lett.*, vol. 16, no. 8, pp. 4738–4745, 2016.

-
- [89] T. Habe and M. Koshino, “Anomalous Hall effect in 2H-phase MX_2 transition-metal dichalcogenide monolayers on ferromagnetic substrates ($M = \text{Mo}, \text{W}$, and $X = \text{S}, \text{Se}, \text{Te}$),” *Phys. Rev. B*, vol. 96, p. 085411, Aug 2017.
- [90] B. Scharf, G. Xu, A. Matos-Abiague, and I. Žutić, “Magnetic proximity effects in transition-metal dichalcogenides: Converting excitons,” *Phys. Rev. Lett.*, vol. 119, p. 127403, Sep 2017.
- [91] A. Kormányos, V. Zólyomi, N. D. Drummond, P. Rakya, G. Burkard, and V. I. Fal’ko, “Monolayer MoS_2 : Trigonal warping, the Γ valley, and spin-orbit coupling effects,” *Phys. Rev. B*, vol. 88, p. 045416, Jul 2013.
- [92] H. Rostami, A. G. Moghaddam, and R. Asgari, “Effective lattice Hamiltonian for monolayer MoS_2 : Tailoring electronic structure with perpendicular electric and magnetic fields,” *Phys. Rev. B*, vol. 88, p. 085440, Aug 2013.
- [93] D. Rybkovskiy, I. Gerber, and M. Durnev, “Atomically inspired $k \cdot p$ approach and valley zeeman effect in transition metal dichalcogenide monolayers,” *Phys. Rev. B*, vol. 95, no. 15, p. 155406, 2017.
- [94] A. Kormányos, G. Burkard, M. Gmitra, J. Fabian, V. Zólyomi, N. D. Drummond, and V. Fal’ko, “ $k \cdot p$ theory for two-dimensional transition metal dichalcogenide semiconductors,” *2D Mater.*, vol. 2, no. 2, p. 022001, 2015.
- [95] C. G. Péterfalvi, A. Kormányos, and G. Burkard, “Boundary conditions for transition-metal dichalcogenide monolayers in the continuum model,” *Phys. Rev. B*, vol. 92, p. 245443, Dec 2015.
- [96] E. Cappelluti, R. Roldán, J. A. Silva-Guillén, P. Ordejón, and F. Guinea, “Tight-binding model and direct-gap/indirect-gap transition in single-layer and multi-layer MoS_2 ,” *Phys. Rev. B*, vol. 88, p. 075409, Aug 2013.
- [97] R. Roldán, M. P. López-Sancho, F. Guinea, E. Cappelluti, J. A. Silva-Guillén, and P. Ordejón, “Momentum dependence of spin-orbit interaction effects in single-layer and multi-layer transition metal dichalcogenides,” *2D Mater.*, vol. 1, no. 3, p. 034003, 2014.
- [98] E. Ridolfi, D. Le, T. Rahman, E. Mucciolo, and C. Lewenkopf, “A tight-binding model for MoS_2 monolayers,” *J. Phys.: Condens. Matter*, vol. 27, no. 36, p. 365501, 2015.

-
- [99] A. Dias, F. Qu, D. L. Azevedo, and J. Fu, “Band structure of monolayer transition-metal dichalcogenides and topological properties of their nanoribbons: Next-nearest-neighbor hopping,” *Phys. Rev. B*, vol. 98, no. 7, p. 075202, 2018.
- [100] F. Zahid, L. Liu, Y. Zhu, J. Wang, and H. Guo, “A generic tight-binding model for monolayer, bilayer and bulk MoS₂,” *Aip Adv.*, vol. 3, no. 5, p. 052111, 2013.
- [101] S. Pavlović and F. M. Peeters, “Electronic properties of triangular and hexagonal MoS₂ quantum dots,” *Phys. Rev. B*, vol. 91, p. 155410, Apr 2015.
- [102] C. Segarra, J. Planelles, and S. E. Ulloa, “Edge states in dichalcogenide nanoribbons and triangular quantum dots,” *Phys. Rev. B*, vol. 93, p. 085312, Feb 2016.
- [103] O. Ávalos-Ovando, D. Mastrogiuseppe, and S. E. Ulloa, “Symmetries and hybridization in the indirect interaction between magnetic moments in MoS₂ nanoflakes,” *Phys. Rev. B*, vol. 94, p. 245429, Dec 2016.
- [104] A. M. Alsharari, M. M. Asmar, and S. E. Ulloa, “Proximity-induced topological phases in bilayer graphene,” *Phys. Rev. B*, vol. 97, p. 241104, Jun 2018.
- [105] T. Čadež, L. Li, E. Castro, and J. Carmelo, “Robust one dimensionality at twin grain boundaries in MoSe₂,” *Phys. Rev. B*, vol. 99, no. 15, p. 155109, 2019.
- [106] O. Ávalos-Ovando, D. Mastrogiuseppe, and S. E. Ulloa, “Lateral interfaces of transition metal dichalcogenides: A stable tunable one-dimensional physics platform,” *Phys. Rev. B*, vol. 99, no. 3, p. 035107, 2019.
- [107] A. Manchon, H. C. Koo, J. Nitta, S. Frolov, and R. Duine, “New perspectives for rashba spin-orbit coupling,” *Nat. Mater.*, vol. 14, no. 9, p. 871, 2015.
- [108] C. L. Kane and E. J. Mele, “Quantum spin Hall effect in graphene,” *Phys. Rev. Lett.*, vol. 95, no. 22, p. 226801, 2005.
- [109] Y. S. Dedkov, M. Fonin, U. Rüdiger, and C. Laubschat, “Rashba effect in the graphene/Ni (111) system,” *Phys. Rev. Lett.*, vol. 100, no. 10, p. 107602, 2008.
- [110] E. I. Rashba, “Graphene with structure-induced spin-orbit coupling: Spin-polarized states, spin zero modes, and quantum Hall effect,” *Phys. Rev. B*, vol. 79, no. 16, p. 161409, 2009.
- [111] T. Frank, P. Högl, M. Gmitra, D. Kochan, and J. Fabian, “Protected pseudo-helical edge states in Z₂-trivial proximitized graphene,” *Phys. Rev. Lett.*, vol. 120, p. 156402, Apr 2018.

-
- [112] E. I. Rashba, “Spin–orbit coupling goes global,” *J. Phys.: Condens. Matter*, vol. 28, p. 421004, aug 2016.
- [113] Y. A. Bychkov and E. I. Rashba, “Oscillatory effects and the magnetic susceptibility of carriers in inversion layers,” *J. Phys. C: Solid State Phys.*, vol. 17, no. 33, p. 6039, 1984.
- [114] B. K. Nikolic, L. P. Zarbo, and S. Souma, “Spin currents in semiconductor nanostructures: A non-equilibrium Green-function approach,” in *Oxford Handbook of Nanoscience and Technology*, 2010.
- [115] J. Sinova, S. O. Valenzuela, J. Wunderlich, C. H. Back, and T. Jungwirth, “Spin Hall effects,” *Rev. Mod. Phys.*, vol. 87, no. 4, p. 1213, 2015.
- [116] R. Winkler, “Rashba spin splitting in two-dimensional electron and hole systems,” *Phys. Rev. B*, vol. 62, no. 7, p. 4245, 2000.
- [117] R. Winkler, *Spin-orbit coupling effects in two-dimensional electron and hole systems*, vol. 191. Springer Science & Business Media, 2003.
- [118] C. R. Ast, J. Henk, A. Ernst, L. Moreschini, M. C. Falub, D. Pacilé, P. Bruno, K. Kern, and M. Grioni, “Giant spin splitting through surface alloying,” *Phys. Rev. Lett.*, vol. 98, no. 18, p. 186807, 2007.
- [119] P. King, R. C. Hatch, M. Bianchi, R. Ovsyannikov, C. Lupulescu, G. Landolt, B. Slomski, J. Dil, D. Guan, J. Mi, *et al.*, “Large tunable Rashba spin splitting of a two-dimensional electron gas in Bi₂Se₃,” *Phys. Rev. Lett.*, vol. 107, no. 9, p. 096802, 2011.
- [120] Y. Zhai, S. Baniya, C. Zhang, J. Li, P. Haney, C.-X. Sheng, E. Ehrenfreund, and Z. V. Vardeny, “Giant rashba splitting in 2D organic-inorganic halide perovskites measured by transient spectroscopies,” *Sci. Adv.*, vol. 3, no. 7, p. e1700704, 2017.
- [121] I. Žutić, A. Matos-Abiague, B. Scharf, H. Dery, and K. Belashchenko, “Proximitized materials,” *Mater. Today*, 2018.
- [122] A. M. Alsharari, M. M. Asmar, and S. E. Ulloa, “Mass inversion in graphene by proximity to dichalcogenide monolayer,” *Phys. Rev. B*, vol. 94, no. 24, p. 241106, 2016.

-
- [123] A. G. Swartz, P. M. Odenthal, Y. Hao, R. S. Ruoff, and R. K. Kawakami, “Integration of the ferromagnetic insulator EuO onto graphene,” *ACS Nano*, vol. 6, no. 11, pp. 10063–10069, 2012.
- [124] P. Wei, S. Lee, F. Lemaitre, L. Pinel, D. Cutaia, W. Cha, F. Katmis, Y. Zhu, D. Heiman, J. Hone, J. S. Moodera, and C.-T. Chen, “Strong interfacial exchange field in the graphene/EuS heterostructure,” *Nat. Mater.*, vol. 15, no. 7, p. 711, 2016.
- [125] J. C. Leutenantsmeyer, A. A. Kaverzin, M. Wojtaszek, and B. J. van Wees, “Proximity induced room temperature ferromagnetism in graphene probed with spin currents,” *2D Mater.*, vol. 4, no. 1, p. 014001, 2016.
- [126] D. Pesin and A. H. MacDonald, “Spintronics and pseudospintronics in graphene and topological insulators,” *Nat. Mater.*, vol. 11, no. 5, p. 409, 2012.
- [127] W. Amamou, I. V. Pinchuk, A. H. Trout, R. E. A. Williams, N. Antolin, A. Goad, D. J. O’Hara, A. S. Ahmed, W. Windl, D. W. McComb, and R. K. Kawakami, “Magnetic proximity effect in Pt/CoFe₂O₄ bilayers,” *Phys. Rev. Mater.*, vol. 2, p. 011401, Jan 2018.
- [128] Y. G. Semenov, K. W. Kim, and J. M. Zavada, “Spin field effect transistor with a graphene channel,” *Appl. Phys. Lett.*, vol. 91, no. 15, p. 153105, 2007.
- [129] H. Haugen, D. Huertas-Hernando, and A. Brataas, “Spin transport in proximity-induced ferromagnetic graphene,” *Phys. Rev. B*, vol. 77, no. 11, p. 115406, 2008.
- [130] N. Li, J. Zhang, Y. Xue, T. Zhou, and Z. Yang, “Large valley polarization in monolayer MoTe₂ on a magnetic substrate,” *Phys. Chem. Chem. Phys.*, vol. 20, pp. 3805–3812, 2018.
- [131] Y. Song and G. Dai, “Spin filter and spin valve in ferromagnetic graphene,” *Appl. Phys. Lett.*, vol. 106, no. 22, p. 223104, 2015.
- [132] D. V. Averyanov, I. S. Sokolov, A. M. Tokmachev, O. E. Parfenov, I. A. Karateev, A. N. Taldenkov, and V. G. Storchak, “High-temperature magnetism in graphene induced by proximity to EuO,” *ACS Appl. Mater. Interfaces*, vol. 10, no. 24, pp. 20767–20774, 2018.
- [133] X. Du, Z. Y. Wang, and G. Q. Huang, “Rashba-type spin splitting and the electronic structure of ultrathin Pb/MoTe₂ heterostructure,” *Mater. Res. Express*, vol. 3, no. 11, p. 116302, 2016.

-
- [134] X. Liang, L. Deng, F. Huang, T. Tang, C. Wang, Y. Zhu, J. Qin, Y. Zhang, B. Peng, and L. Bi, “The magnetic proximity effect and electrical field tunable valley degeneracy in MoS₂/EuS van der Waals heterojunctions,” *Nanoscale*, vol. 9, no. 27, pp. 9502–9509, 2017.
- [135] L. Xu, M. Yang, L. Shen, J. Zhou, T. Zhu, and Y. P. Feng, “Large valley splitting in monolayer WS₂ by proximity coupling to an insulating antiferromagnetic substrate,” *Phys. Rev. B*, vol. 97, no. 4, p. 041405, 2018.
- [136] G. Yang, J. Li, H. Ma, Y. Yang, C. Li, X. Mao, and F. Yin, “Induced valley splitting in monolayer MoS₂ by an antiferromagnetic insulating CoO (111) substrate,” *Phys. Rev. B*, vol. 98, no. 23, p. 235419, 2018.
- [137] X. Li, T. Cao, Q. Niu, J. Shi, and J. Feng, “Coupling the valley degree of freedom to antiferromagnetic order,” *Proc. Natl. Acad. Sci. U.S.A.*, vol. 110, no. 10, pp. 3738–3742, 2013.
- [138] S. Datta and B. Das, “Electronic analog of the electro-optic modulator,” *App. Phys. Lett.*, vol. 56, pp. 665–667, Feb. 1990.
- [139] P. Sharma, “How to create a spin current,” *Science*, vol. 307, no. 5709, pp. 531–533, 2005.
- [140] Z.-X. Shen and J. Sobota, “Condensed-matter physics: Taking control of spin currents,” *Nature*, vol. 549, no. 7673, p. 464, 2017.
- [141] E. I. Rashba, “Spin currents in thermodynamic equilibrium: The challenge of discerning transport currents,” *Phys. Rev. B*, vol. 68, no. 24, p. 241315, 2003.
- [142] H. Zhang, Y. Yun, X. Zhang, H. Zhang, Y. Ma, X. Yan, F. Wang, G. Li, R. Li, T. Khan, Y. Chen, W. Liu, F. Hu, B. Liu, B. Shen, W. Han, and J. Sun, “High-mobility spin-polarized two-dimensional electron gases at EuO/KTaO₃ interfaces,” *Phys. Rev. Lett.*, vol. 121, p. 116803, Sep 2018.
- [143] J. C. Leutenantsmeyer, J. Ingla-Aynés, J. Fabian, and B. J. van Wees, “Observation of spin-valley-coupling-induced large spin-lifetime anisotropy in bilayer graphene,” *Phys. Rev. Lett.*, vol. 121, p. 127702, Sep 2018.
- [144] J. Xu, T. Zhu, Y. K. Luo, Y.-M. Lu, and R. K. Kawakami, “Strong and tunable spin-lifetime anisotropy in dual-gated bilayer graphene,” *Phys. Rev. Lett.*, vol. 121, p. 127703, Sep 2018.

-
- [145] Q. Liu, L. Li, Y. Li, Z. Gao, Z. Chen, and J. Lu, “Tuning electronic structure of bilayer MoS₂ by vertical electric field: a first-principles investigation,” *J. Phys. Chem. C*, vol. 116, no. 40, pp. 21556–21562, 2012.
- [146] H.-P. Komsa and A. V. Krasheninnikov, “Native defects in bulk and monolayer MoS₂ from first principles,” *Phys. Rev. B*, vol. 91, no. 12, p. 125304, 2015.
- [147] J. Hong, Y. Pan, Z. Hu, D. L. C. Jin, W. Ji, J. Yuan, and Z. Zhang, “Direct imaging of kinetic pathways of atomic diffusion in monolayer molybdenum disulfide,” *Nano Lett.*, vol. 17, no. 6, p. 3383, 2017.
- [148] M. Kertesz and R. Hoffmann, “Octahedral vs. trigonal-prismatic coordination and clustering in transition-metal dichalcogenides,” *J. Am. Chem. Soc.*, vol. 106, no. 12, pp. 3453–3460, 1984.
- [149] E. Benavente, M. Santa Ana, F. Mendizábal, and G. González, “Intercalation chemistry of molybdenum disulfide,” *Coord. Chem. Rev.*, vol. 224, no. 1, pp. 87–109, 2002.
- [150] X. Hong, J. Kim, S.-F. Shi, Y. Zhang, C. Jin, Y. Sun, S. Tongay, J. Wu, Y. Zhang, and F. Wang, “Ultrafast charge transfer in atomically thin MoS₂/WS₂ heterostructures,” *Nat. Nanotechnol.*, vol. 9, no. 9, pp. 682–686, 2014.
- [151] D. Xiao, M.-C. Chang, and Q. Niu, “Berry phase effects on electronic properties,” *Rev. Mod. Phys.*, vol. 82, no. 3, p. 1959, 2010.
- [152] X. Fan, W. Zheng, J.-L. Kuo, D. J. Singh, C. Sun, and W. Zhu, “Modulation of electronic properties from stacking orders and spin-orbit coupling for 3R-type MoS₂,” *Sci. Rep.*, vol. 6, p. 24140, 2016.
- [153] A. Castellanos-Gomez, R. Roldán, E. Cappelluti, M. Buscema, F. Guinea, H. S. van der Zant, and G. A. Steele, “Local strain engineering in atomically thin MoS₂,” *Nano Lett.*, vol. 13, no. 11, pp. 5361–5366, 2013.
- [154] P. San-Jose, V. Parente, F. Guinea, R. Roldán, and E. Prada, “Inverse funnel effect of excitons in strained black phosphorus,” *Phys. Rev. X*, vol. 6, no. 3, p. 031046, 2016.
- [155] J. Feng, X. Qian, C.-W. Huang, and J. Li, “Strain-engineered artificial atom as a broad-spectrum solar energy funnel,” *Nat. Photon.*, vol. 6, no. 12, pp. 866–872, 2012.

-
- [156] A. P. Rooney, A. Kozikov, A. N. Rudenko, E. Prestat, M. J. Hamer, F. Withers, Y. Cao, K. S. Novoselov, M. I. Katsnelson, R. V. Gorbachev, *et al.*, “Observing imperfection in atomic interfaces for van der Waals heterostructures,” *Nano Lett.*, 2017.
- [157] H. Brauer, H. Starnberg, L. Holleboom, H. Hughes, and V. Strocov, “Modifying the electronic structure of TiS_2 by alkali metal intercalation,” *Journal of Physics: Condensed Matter*, vol. 11, no. 45, p. 8957, 1999.
- [158] Y. Chen, P. Cui, X. Ren, C. Zhang, C. Jin, Z. Zhang, and C.-K. Shih, “Fabrication of MoSe_2 nanoribbons via an unusual morphological phase transition,” *Nat. Commun.*, vol. 8, p. 15135, 2017.
- [159] W. Huang, X. Wang, X. Ji, Z. Zhang, and C. Jin, “In-situ fabrication of Mo_6S_6 -nanowire-terminated edges in monolayer molybdenum disulfide,” *Nano Res.*, vol. 11, no. 11, pp. 5849–5857, 2018.
- [160] H. Rostami, R. Asgari, and F. Guinea, “Edge modes in zigzag and armchair ribbons of monolayer MoS_2 ,” *J. Phys.: Condens. Matter*, vol. 28, no. 49, p. 495001, 2016.
- [161] E. Ridolfi, L. R. Lima, E. R. Mucciolo, and C. H. Lewenkopf, “Electronic transport in disordered MoS_2 nanoribbons,” *Phys. Rev. B*, vol. 95, no. 3, p. 035430, 2017.
- [162] A. P. Schnyder, C. Timm, and P. M. R. Brydon, “Edge currents as a signature of flatbands in topological superconductors,” *Phys. Rev. Lett.*, vol. 111, no. 7, p. 077001, 2013.
- [163] R. Brown, N. R. Walet, and F. Guinea, “Edge modes and nonlocal conductance in graphene superlattices,” *Phys. Rev. Lett.*, vol. 120, no. 2, p. 026802, 2018.
- [164] S. Pan, F. Ceballos, M. Z. Bellus, P. Zereszki, and H. Zhao, “Ultrafast charge transfer between MoTe_2 and MoS_2 monolayers,” *2D Mater.*, vol. 4, no. 1, p. 015033, 2016.
- [165] H. Zhang, Z. Ma, and J.-F. Liu, “Equilibrium spin current in graphene with Rashba spin-orbit coupling,” *Sci. Rep.*, vol. 4, p. 6464, 2014.
- [166] S. A. Wolf, D. D. Awschalom, R. A. Buhrman, J. M. Daughton, S. von Molnar, M. L. Roukes, A. Y. Chtchelkanova, and D. M. Treger, “Spintronics: a spin-based electronics vision for the future,” *Science*, vol. 294, no. 5546, pp. 1488–1495, 2001.

-
- [167] P. Lazić, K. D. Belashchenko, and I. Žutić, “Effective gating and tunable magnetic proximity effects in two-dimensional heterostructures,” *Phys. Rev. B*, vol. 93, no. 24, p. 241401, 2016.
- [168] A. Dankert and S. P. Dash, “Electrical gate control of spin current in van der Waals heterostructures at room temperature,” *Nat. Commun.*, vol. 8, p. 16093, 2017.
- [169] S. Cho, S. Kim, J. H. Kim, J. Zhao, J. Seok, D. H. Keum, J. Baik, D.-H. Choe, K. J. Chang, K. Suenaga, S. W. Kim, Y. H. Lee, and H. Yang, “Phase patterning for ohmic homojunction contact in MoTe_2 ,” *Science*, vol. 349, no. 6248, pp. 625–628, 2015.
- [170] K. Elibol, T. Susi, G. Argentero, M. Reza Ahmadpour Monazam, T. J. Pennycook, J. C. Meyer, and J. Kotakoski, “Atomic structure of intrinsic and electron-irradiation-induced defects in MoTe_2 ,” *Chem. Mater.*, vol. 30, no. 4, pp. 1230–1238, 2018.
- [171] M. Shahbazi, “Linear giant stark effect in WSe_2 nanoribbons,” *Physica B: Condens. Matter*, vol. 545, pp. 159–166, 2018.
- [172] K. Lee, W. S. Yun, and J. Lee, “Giant rashba-type splitting in molybdenum-driven bands of MoS_2/Bi (111) heterostructure,” *Phys. Rev. B*, vol. 91, no. 12, p. 125420, 2015.
- [173] Q. Zhang and U. Schwingenschlögl, “Rashba effect and enriched spin-valley coupling in GaX/MX_2 ($\text{M}=\text{Mo}, \text{W}$; $\text{X}=\text{S}, \text{Se}, \text{Te}$) heterostructures,” *Phys. Rev. B*, vol. 97, no. 15, p. 155415, 2018.
- [174] Q.-F. Yao, J. Cai, W.-Y. Tong, S.-J. Gong, J.-Q. Wang, X. Wan, C.-G. Duan, and J. Chu, “Manipulation of the large Rashba spin splitting in polar two-dimensional transition-metal dichalcogenides,” *Phys. Rev. B*, vol. 95, no. 16, p. 165401, 2017.
- [175] T. Hu, F. Jia, G. Zhao, J. Wu, A. Stroppa, and W. Ren, “Intrinsic and anisotropic Rashba spin splitting in Janus transition-metal dichalcogenide monolayers,” *Phys. Rev. B*, vol. 97, no. 23, p. 235404, 2018.
- [176] Y. Li, Z. Zhou, S. Zhang, and Z. Chen, “ MoS_2 nanoribbons: High stability and unusual electronic and magnetic properties,” *J. Am. Chem. Soc.*, vol. 130, no. 49, pp. 16739–44, 2008.

-
- [177] A. R. Botello-Méndez, F. López-Urías, M. Terrones, and H. Terrones, “Metallic and ferromagnetic edges in molybdenum disulfide nanoribbons,” *Nanotechnology*, vol. 20, no. 32, p. 325703, 2009.
- [178] K. Dolui, C. D. Pemmaraju, and S. Sanvito, “Electric field effects on armchair MoS₂ nanoribbons,” *ACS nano*, vol. 6, no. 6, pp. 4823–4834, 2012.
- [179] M. DavoodianIdalik, A. Kordbacheh, and F. Velashjerdi, “Structural, electronic and transport properties of an edge terminated armchair MoS₂ nanoribbon with N, O and F atoms,” *AIP Adv.*, vol. 9, no. 3, p. 035144, 2019.
- [180] O. Ávalos-Ovando, D. Mastrogiuseppe, and S. E. Ulloa, “Lateral heterostructures and one-dimensional interfaces in 2D transition metal dichalcogenides,” *J. Phys.: Condens. Matter*, vol. 31, no. 21, p. 213001, 2019.
- [181] M. Al Hajj, F. Alet, S. Capponi, M.-B. Lepetit, J.-P. Malrieu, and S. Todo, “Parity law of the singlet-triplet gap in graphitic ribbons,” *Eur. Phys. J. B*, vol. 51, no. 4, pp. 517–522, 2006.
- [182] L. Šmejkal, Y. Mokrousov, B. Yan, and A. H. MacDonald, “Topological antiferromagnetic spintronics,” *Nat. Phys.*, vol. 14, no. 3, p. 242, 2018.
- [183] J. H. Garcia, A. W. Cummings, and S. Roche, “Spin hall effect and weak antilocalization in graphene/transition metal dichalcogenide heterostructures,” *Nano letters*, vol. 17, no. 8, pp. 5078–5083, 2017.
- [184] G. Z. Magda, X. Jin, I. Hagymási, P. Vancsó, Z. Osváth, P. Nemes-Incze, C. Hwang, L. P. Biro, and L. Tapasztó, “Room-temperature magnetic order on zigzag edges of narrow graphene nanoribbons,” *Nature*, vol. 514, no. 7524, p. 608, 2014.
- [185] S. Su, Y. Barlas, J. Li, J. Shi, and R. K. Lake, “Effect of intervalley interaction on band topology of commensurate graphene/euo heterostructures,” *Physical Review B*, vol. 95, no. 7, p. 075418, 2017.
- [186] D. Moldovan, M. Anđelković, and F. Peeters, “pybinding v0.9.4: a Python package for tight-binding calculations,” July 2017. This work was supported by the Flemish Science Foundation (FWO-V1) and the Methusalem Funding of the Flemish Government.
- [187] S. Datta, *Electronic transport in mesoscopic systems*. Cambridge university press, 1997.

-
- [188] S. Datta, *Quantum transport: atom to transistor*. Cambridge university press, 2005.
- [189] Q. Zhang, K. Chan, and J. Li, “Spin-transfer torque generated in graphene based topological insulator heterostructures,” *Scientific reports*, vol. 8, no. 1, p. 4343, 2018.
- [190] N. Troullier and J. L. Martins, “Efficient pseudopotentials for plane-wave calculations,” *Phys. Rev. B*, vol. 43, pp. 1993–2006, Jan 1991.
- [191] S. G. Louie, S. Froyen, and M. L. Cohen, “Nonlinear ionic pseudopotentials in spin-density-functional calculations,” *Phys. Rev. B*, vol. 26, pp. 1738–1742, Aug 1982.
- [192] M. Dion, H. Rydberg, E. Schröder, D. C. Langreth, and B. I. Lundqvist, “Van der Waals Density Functional for general geometries,” *Phys. Rev. Lett.*, vol. 92, p. 246401, Jun 2004.
- [193] V. R. Cooper, “Van der Waals density functional: An appropriate exchange functional,” *Phys. Rev. B*, vol. 81, p. 161104, Apr 2010.
- [194] J. Zhao, H. Nam, T. H. Ly, S. J. Yun, S. Kim, S. Cho, H. Yang, and Y. H. Lee, “Chain vacancies in 2D crystals,” *Small*, vol. 13, no. 1, p. 1601930, 2017.
- [195] S. Cho, S. H. Kang, H. S. Yu, H. W. Kim, W. Ko, S. W. Hwang, W. H. Han, D.-H. Choe, Y. H. Jung, K. J. Chang, Y. H. Lee, H. Yang, and S. W. Kim, “Te vacancy-driven superconductivity in orthorhombic molybdenum ditelluride,” *2D Mater.*, vol. 4, no. 2, p. 021030, 2017.
- [196] J. C. Caulfield and A. J. Fisher, “Electronic structure and scanning tunnelling microscope images of missing-atom defects on and surfaces,” *J. Phys.: Condens. Matter*, vol. 9, no. 18, p. 3671, 1997.

Appendix A

MoS₂ Bilayers

In this Appendix we describe the technical details used in the band structure calculations for the MoS₂ pristine bilayers with 1×1 unit cell in Section 2.1.3, as well as for the MoS₂ Mo-doped bilayers with 3×3 unit cell described in Chapter 3. We also show the relaxed geometry and band structure results for the MoS₂ Mo-doped bilayer in the 3R-phase with AB stacking.

A.1 Simulation Details

Within the density functional of vdW (vdW-DF) used in the calculations in Chapter 3, we consider norm-conserving relativistic ab-initio pseudopotentials in the Troullier Martins form [190], including nonlinear core corrections for inner d -electrons [191]. The exchange and correlation energy are calculated by the non-local vdW-DF, using the parametrization proposed by Dion *et al.* [192], taking into account the exchange energy modification included by Cooper (C09) [193]. In the C09 parametrization, the long-range dispersion effects are included as a perturbation to the local-density approximation correlation term. The vdW parameterization was chosen after comparing the band structure of the AA' system for the 1×1 unit cell with the existing literature [85], in particular the presence of an indirect band gap between the Γ and K points. Note that the bottom of the conduction band can move away from the K point depending on the chosen vdW functional. Basis set is double- ζ polarized (DZP) with numerical atomic orbital with an energy shift of 30 meV, converged to have an extended basis to describe long vdW bonds. The mesh cutoff energy for the integration grid was well converged using 230 Ry. A k -grid of $10 \times 10 \times 1$ Monkhorst-Pack is used to sample the BZ. A vacuum region in the z -direction, of at least 20 Å avoids interactions with periodic images. The structures were relaxed until the force in each atom was less than

10^{-2} eV/Å.

We provide extra technical details to assure the reproducibility of the results. The valence electronic configurations for the atoms in the pseudopotentials calculations were $5s^1 4d^5$ and $3s^2 3p^4$ for Mo and S atoms, respectively. The pseudopotentials core radii and pseudocore radii are included in Table A.1.

	r_s	r_p	r_d	r_{pc}
Mo	2.30	2.46	1.67	1.20
S	1.63	1.76	1.94	1.20

Table A.1: Pseudopotentials core radii for s, p, d channels, and the pseudocore radii r_{pc} for the Mo and S atoms. All the radii are in Bohr.

A.2 Mo Impurities in 3R Phase

Another type of stacking labeled as AB is possible in MoS₂ bilayers, which belongs to the 3R phase. In this stacking type a layer just glides on the other layer. Although our main results show that pristine AB MoS₂ bilayer is slightly more stable than the pristine AA' bilayer, the presence of Mo_{imp} changes the stability order in the order of electron volts. The AB stacking configurations are shown in Fig. A.1 for the MoS₂ bilayer with Mo impurities, which are indicated by red spheres. Similar to the 2H-phase, the Mo_{imp} in the 3R-phase prefers an octahedral environment, as shown in Fig. A.1 for T-AB. The T-AB configuration has the lowest energy in the 3R-phase. Taking the T-AB' configuration (2H-phase) as the energy reference, the T-AB configuration has a total energy of 0.75 eV, which is between the T-AB' and H-AA' configurations of Fig. 3.1. The T'-AB configuration in Fig. A.1 with tetrahedral symmetry lies 1.82 eV above the most stable T-AB', between the T'-AB' and T'-AA' configurations. The band structure for the T-AB and T'-AB Mo_{imp} configurations in the 3R-phase are shown in Fig. A.2. The total magnetic moment follows a similar trend according to the specific site, zero for the T-AB configuration (octahedral) and $2\mu_B$ for the T'-AB configuration (tetrahedral).

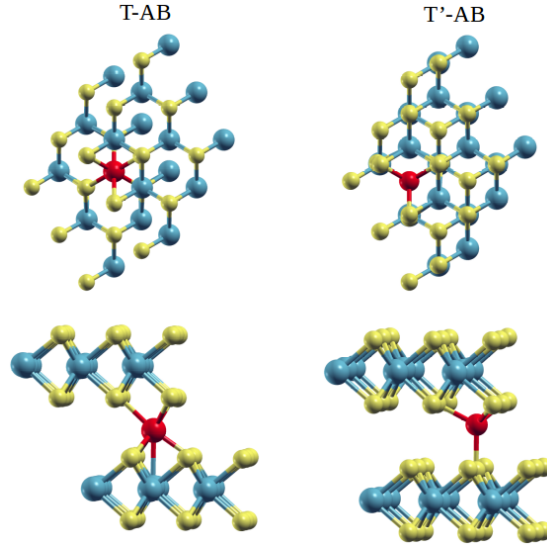


Figure A.1: Top and side views for relaxed structures of MoS₂ bilayer with Mo_{imp} in the 3R phase with AB stacking. T-AB and T'-AB refers to Mo_{imp} on top of a Mo and S atom in the AB stacking, respectively. Red spheres show the Mo_{imp} in each configuration.

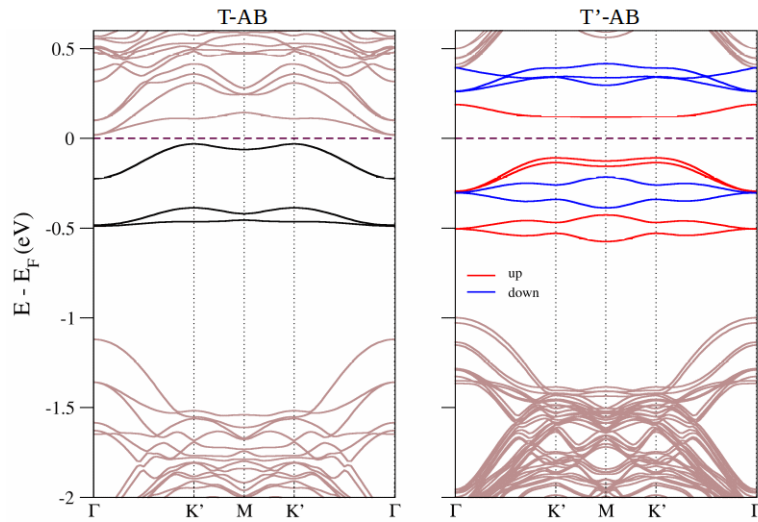


Figure A.2: Band structures for MoS₂ bilayers with Mo_{imp} in the 3R phase and AB stacking. The Fermi energy is set at 0 eV.

Appendix B

MoTe₂ Zigzag Ribbons with Defects

A variety of defects in MoTe₂ flakes such as single or double vacancies, chain vacancies, adatoms, irregular edges, and grain boundaries, among others, can be present in realistic MoTe₂ flakes, and produce interesting effects [169, 194, 170]. For example, chalcogen deficiency (Te-vacancies) may trigger a transition from the 2H to the 1T' phase when the chalcogen vacancy concentration is greater than $\sim 3\%$ [169, 170], and twin-grain boundaries [52, 21] may act as 1D channels in MoTe₂. Similarly, a superconducting state driven by Te-vacancies was seen at low temperatures [195]. Weak random bulk and edge disorder has been shown to not affect significantly the edge modes lying in the band gap, producing only slight deviations from the pristine-edge structure [69]. Here we focus on the effects that Mo and Te vacancies in the MoTe₂ ribbon produce, especially on midgap electronic states, paying special attention to Te-vacancies near the zigzag edges.

By means the *magnetized* 3OTB Hamiltonian of Section 4.2, we model disorder in the zigzag ribbon, such as Te- (Te_v) and Mo-vacancies (Mo_v) using two different approaches depending on the nature of the vacancy [161]: For Mo_v , one adds a large onsite potential to the desired vacancy-site; for the Te_v , one cuts the intermetallic hoppings surrounding the vacancy-site. We have considered different vacancy configurations, including Mo_v or Te_v at either the Mo-edge or the Te-edge, vacancies in the bulk, and random combinations of these. Note that the chalcogen-edge in this model has an unambiguous single midgap state, unlike the multiple metal-edge states in a representation with more orbitals [60, 69]. The results we present here study vacancy configurations in the system with the weaker exchange field of Section 4.3, as the electronic Mo-modes are well decoupled from the bulk and located midgap. Similar results

and conclusions are applicable for other values of the exchange field.

The probability density for different states can be projected in the ribbon real-space for each orbital [101, 160], providing insightful information on the wave function behavior; we focus here in the range of midgap states. As the orbital composition of these states shows a d_{z^2} orbital majority, in the following we show the spatial dependence of the projected orbital component (POC) for this orbital—as the other orbital components show identical spatial structure.

It is instructive to first show the POC behavior for pristine MoTe₂ zigzag ribbons. Representative midgap eigenstates with energy E are shown in Fig. B.1 along both the Mo- and Te-edges, for Fermi levels E_{F_1} and E_{F_3} , respectively. In both pristine edges, each metal atom along the edge has the same POC, as expected. This is associated with the well-defined k momentum at each energy, and extracted from the fast Fourier transform (FFT) on the pristine ribbon states. As we will see in the next sections, when the system has vacancy defects, the POC is not constant and oscillates near the site where the vacancy is located, giving the many k momenta contained in each state introduced by backscattering, and obtained after FFT decomposition.

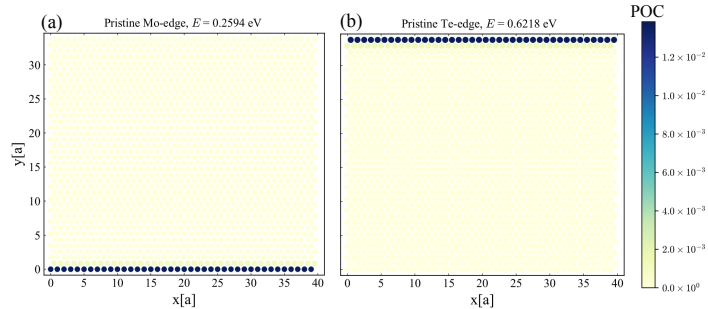


Figure B.1: Projected d_{z^2} orbital component (POC) for midgap states in pristine MoTe₂ ribbon on ferromagnetic substrate. Each circle corresponds to a Mo-atom site in the ribbon, while the heat color associated to each atom indicates the POC there. The ribbon is periodic along the x -direction so that the zigzag Mo-edge is at $y = 0$ and the zigzag Te-edge is at $y = H$, where H is the ribbon width (here $H = 40a\sqrt{3}/2$). Selected energy eigenstates have midgap energy close to Fermi level E_{F_1} at the Mo-edge in (a), and close to E_{F_3} at the Te-edge in (b). Both eigenstates shown here have positive k , and correspond to states with majority spin up and down along $\langle S_Z \rangle$, respectively. Fermi levels are indicated in Fig. 4.4(c-d).

B.1 Vacancies

As described above, we simulate vacancies in the structure by either modifying the onsite (for Mo_v) or the hopping parameters (for Te_v). This approach has been validated in detailed studies of defects [161], and is shown to produce reliable descriptions.

We have performed a systematic study of the effects of different concentrations and locations of Mo_v and Te_v at the Mo- and Te-edges, as well as in the interior (bulk), for zigzag ribbons with 1600 Mo sites. We have also analyzed these effects for a narrower MoTe_2 ribbon with 400 Mo sites (20 Mo sites along the zigzag direction) and obtained very similar results, ruling out finite size effects. We find comparable effects for Mo_v and Te_v configurations, as explained in detail in the following subsections.

As a general result, we find that energy eigenstates with weight near the defect are slightly shifted with respect to the pristine case. Moreover, even when defects are present in the bulk or opposite edge, the states in a clean edge remain with constant POC as in the pristine case, and associated to a single k momentum. Those unaffected 1D edge modes are then obviously robust to distant perturbation (a few lattice constants away) and accessible to Fermi levels in the bandgap.

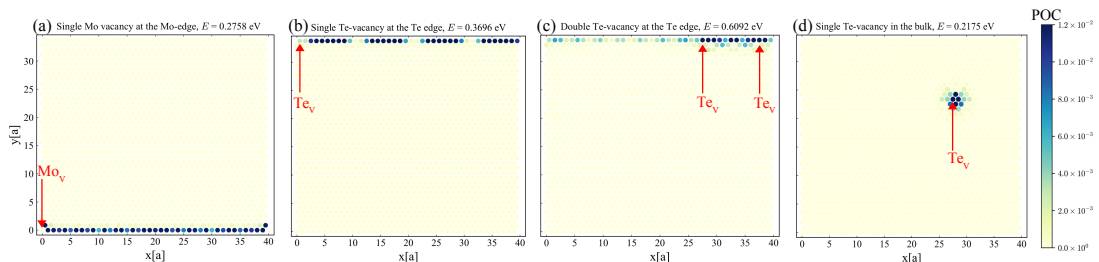


Figure B.2: Projected orbital component (POC) for different vacancy-configurations in MoTe_2 ribbon on a ferromagnetic substrate, and states with energies near the Fermi levels of Fig. 4.4(c)-(d). (a) A single Mo_v on the Mo-edge for $E \simeq E_{F1}$; (b) single Te_v on the Te-edge with $E \simeq E_{F2}$; (c) two Te_v on the Te-edge for $E \simeq E_{F3}$; and (d) state for single Te_v in the bulk for $E \simeq E_{F1}$. Red arrows indicate location and type of vacancy present. For Te_v , the red arrows point to the Mo-atom in the unit cell of the vacancy site, which is $(\mathbf{R}_1 + \mathbf{R}_2)/3$ away.

B.1.1 Te Vacancies at the Edges

Te-vacancies are modeled by cutting the hoppings surrounding the vacancy-site in the lattice. Due to the symmetry in the model, removal of hoppings around a Te-site essentially eliminates a Te-pair above and below the metal plane; in the following we

will refer to this as a Te_v vacancy. At the Mo-edge, this requires cutting the hoppings among the three Mo sites surrounding the vacancy. For a Te_v at the Te-edge, only hoppings in \mathbf{R}_1 and \mathbf{R}_4 directions are cut [see Fig. 2.3(a)].

As the formation energy for Te_v is the lowest (according to DFT studies [194]), we analyze in detail Te_v configurations at the Te-edge. Figure B.2(b) shows a single Te_v at the ribbon first site, on the Te-edge (top row) and at energy $E \simeq E_{F2}$ Fermi level. The POC is non constant and has oscillating behavior, signaling the existence of more than one k momentum component in these eigenstates, and the broken translational invariance in the ribbon introduced by the vacancy. A Te_v at other edge location, such as $x = 28a$, naturally yields the same results. Additionally, we find electronic states with midgap energy $E \simeq 0.1$ eV (below E_{F1}), with POC highly localized around the Te_v -site. Such localized states on the Mo-edge are observed for Te_v with energies $E \simeq 0.2$ eV. We notice this energy range is associated with higher density of states of the edge channels and near degeneracy with bulk states in the valence band, as seen in Fig. 4.4(c-d), which should enhance the role of backscattering introduced by the vacancies.

With two Te_v located at different positions on the Te-edge, such as $x = 28a$ and $x = 38a$ in Fig. B.2(c), the POC near E_{F3} is high around both Te_v sites, and symmetric with respect to the center site between both vacancies. Additional vacancies on the edge produce more states with inhomogeneous POC and more spatial frequencies, as one would expect. There is also a direct relation between the number of localized electronic states below E_{F1} and the number of (non-adjacent) Te_v vacancies on the Te-edge. Each of the localized states is confined around each Te_v , and with nearly degenerate energies.

B.1.2 Mo Vacancies at the Edges

Mo_v vacancies are modeled by changing the onsite potential at the transition metal atom of interest. The onsite potential is made large enough ($\simeq 10^3$ eV), to create a high energy barrier at the vacancy-site, as discussed in the literature [161].

As in the case of Te_v , an Mo_v on the Te-edge produces electronic states with midgap energies $E \simeq 0.1$ eV, with POC localized in the Mo_v vicinity. In Fig. B.2(a), a single Mo_v is at the first site of the Mo-edge (bottom row); the state with $E \simeq E_{F1}$ has vanishing POC at the Mo_v -site, and oscillates along the edge with a combination of several k momenta. Two Mo_v on the Mo-edge show similar vanishing POC around the Mo_v sites, symmetric around the midpoint between the two vacancies.

B.1.3 Vacancies in the bulk

For either a single Mo_v or Te_v in the bulk, vacancy-associated electronic states are found in the midgap, with highly localized POC around the vacancy site. However, the POC for midgap states on both Mo and Te-edges remains uniform, showing a well-defined single k momentum, as in the pristine case. Mo_v in the bulk produces localized states in energy regions $E < E_{F2}$ and $E > E_{F4}$, while Te_v localizes electronic states with $E < E_{F2}$. Figure B.2(d) shows a typical localized POC around a single Te_v in the bulk with $E \simeq E_{F1}$. It is worth noting that our results are in full agreement with early work on vacancies in the MoTe_2 bulk [196].

The effect of two or more vacancies in the bulk is to produce more states in the midgap, in the aforementioned energy regions. All these states have POC localized around the vacancy, and although found in the midgap, they do not carry any current and can not contribute to the spin currents along the Mo- and Te-edges.

We have also tested some other defect configurations: (i) a vacancy at the Mo or Te edge, plus a vacancy near the edge. (ii) one vacancy at each edge plus a vacancy in the bulk. As long as the vacancies are not in adjacent sites, there is no interaction between defects in the bulk and vacancies at the edge, even when they result in midgap states.

We have fully characterized the effects of experimentally realistic defective edges, i.e. atomic vacancies in our MoTe_2 -EuO system, for realistic vacancy concentrations seen in experiments [169, 194, 170, 52, 21, 195].

Appendix C

Pristine Armchair Ribbons

In this Appendix we provide the band structure results for freestanding pristine armchair MoTe₂ ribbons constructed with the 3OTB Hamiltonian of Chapter 2. These results are useful for comparing band structure results when the ribbons are on different AFM substrates, forming MoTe₂-AFM vertical heterostructures, such as the described in Chapter 5.

Figure C.1(a) shows a pristine TMD monolayer with defined zigzag and armchair edges along the x - and y -direction, respectively. The unit cell for the zigzag/armchair ribbon is shown as red/cyan colors. Pristine TMD armchair ribbons are constructed considering PBC along the y -axis. If one stitches both horizontal edges, a N -wide H -long PBC armchair-terminated ribbon is obtained.

The M-M distance projected along the y -axis is $a\sqrt{3}/2$, while the M-M distance projected along the x -axis is a , where $a = 3.56 \text{ \AA}$ is the MoTe₂ lattice constant. Along the y -axis, the length of the armchair unit cell is twice the M-M distance ($a\sqrt{3}$), consequently, the BZ is folded along the momentum k_y , generating a reduced BZ in comparison to the pristine BZ of zigzag ribbons and the 2D bulk [106], as shown in Fig. C.1(b). Therefore, in armchair TMD ribbons, the K and K' symmetry points (or valleys) are both mapped onto the one at Γ ($k_y = 0$) in the reduced BZ [176, 160]. The band structure for the armchair ribbons are obtained by Fourier transforming the real space lattice results from the 3OTB model described in Section 2.3.1.1.

The energy spectrum of pristine TMD ribbons with armchair edges is in stark contrast to that of zigzag-terminated ribbons. Pristine armchair ribbons have semiconducting character with gapped edge modes lying in the bulk gap. This electronic behavior has been demonstrated through diverse approaches [176, 177, 178, 160, 161]. Rostami *et al.* [160] showed that valley mixing is required to open the gap seen at the edges for each spin; accordingly, the origin of the gapped edge modes is attributed to

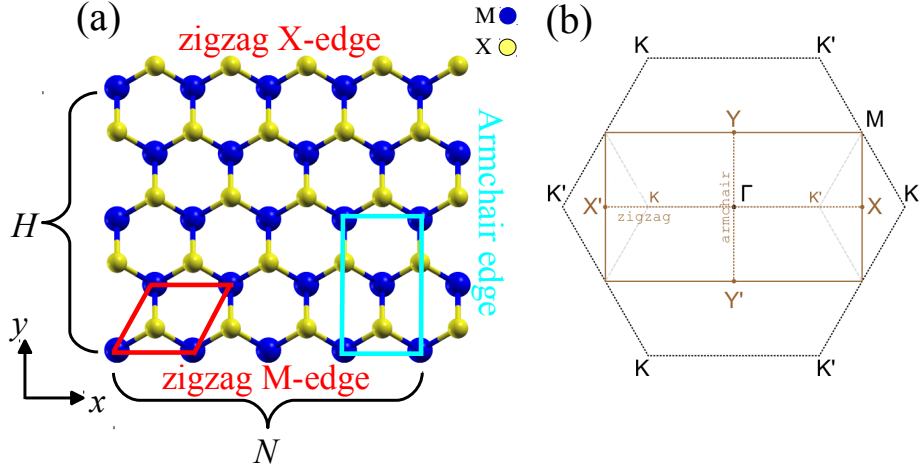


Figure C.1: (a) Top view for a MX_2 pristine monolayer, zigzag/armchair edges are along the x/y -axis, their unit cells are showed as red rhomboid (zigzag) and cyan rectangle (armchair). N , H indicates the size of the ribbon, in this example, $N = 5$ M sites, $H = 5$ M sites, the total amount of M sites is then $N_{sites} = N \times H = 25$ M sites. (b) First BZ for the 2D monolayer (hexagonal), as well as for zigzag and armchair-terminated ribbons (rectangular). The band structure for zigzag/armchair ribbons is projected along the momentum k_x/k_y . The $X' - K - \Gamma - K' - X$ path correspond to k_x momentum projection, while the $Y - \Gamma - Y'$ path correspond to k_y momentum projection.

the mixing of the 1D valleys on the edges of armchair TMD ribbons.

The energy dispersions with SOC for the pristine MoTe_2 armchair ribbon of size $N = 40$, $H = 42$ (1680 Mo sites) with spin up/down projection are shown in Fig. C.2(a)/(b). The semiconducting character is clear, with a direct band gap of 0.51 eV at $k_y = 0$. In both, the spin up and spin down dispersions, a pair of edge modes is close to the valence bulk bands, other pair sits near the conduction bulk bands. By calculating the wave functions associated to each edge state of the edge modes, we have checked that the gapped edge modes are localized along the left and right armchair edges, as is indicated by the symbols in Fig. C.2. The eigenenergies along the edge modes are nearly degenerate around $k_y = 0$, that is, each k_y single value has two eigenenergies (per spin) associated to the band folding, leading to gapped edge modes. Edge mixing for some valence and conduction edge states is also seen for the corresponding k_y value associated, represented as green/dark-pink stars for spin up/down. The edge mixing is attributed to energy states with wave functions distributed simultaneously along both armchair edges (left and right). If we consider both spins in the dispersion, panel (c)

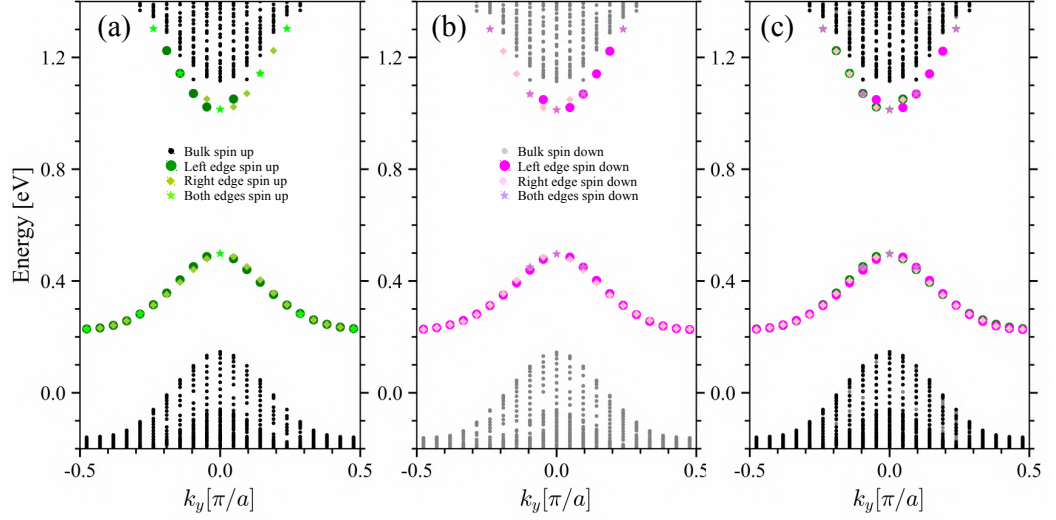


Figure C.2: Energy spectrum for the MoTe_2 pristine armchair-terminated ribbon of size $N = 40$ (width), $H = 42$ (length) (1680 Mo sites). In panel (a) spin up, panel (b) spin down, panel (c) shows both, spin up and spin down [same legends as in panels (a) and (b) apply for panel (c)].

shows that each spin up edge mode has a nearly degenerate spin down band copy. Then, the energy dispersion for the edge modes in pristine armchair TMD ribbons with full SOC, shows there are four eigenenergies associated to a single value of the momentum k_y due to the spin degeneracy and band folding.

Appendix D

List of Publications and Presentations

D.1 Publications

- **Natalia Cortés**, O. Ávalos-Ovando, L. Rosales, P. A. Orellana and S. E. Ulloa, *Tunable spin-polarized edge currents in proximitized transition metal dichalcogenides*, Phys. Rev. Lett. **122**, 086401 (2019).
- **Natalia Cortés**, L. Rosales, P. A. Orellana, A. Ayuela and J. W. González, *Stacking change in MoS₂ bilayers induced by interstitial Mo impurities*, Sci. Rep. **8**, 2143 (2018).

D.2 Other publications

- **Natalia Cortés**, L. Rosales, L. Chico, M. Pacheco and P. A. Orellana, *Enhancement of thermoelectric efficiency by quantum interference effects in trilayer silicene flakes*, J. Phys.: Condens. Matter **29**, 015004 (2017).
- **Natalia Cortés**, Leonor Chico, M. Pacheco, L. Rosales and P. A. Orellana. *Bound states in the continuum: Localization of Dirac-like fermions*, Europhys. Lett. **108**, 46008 (2014).
- M. Ahumada, **Natalia Cortés**, M. L. Ladrón de Guevara and P. A. Orellana, *Dicke and Fano effects in single photon transport*, Opt. Commun. **332**, 366 (2014).

D.3 Work in progress

- **Natalia Cortés**, O. Ávalos-Ovando and S. E. Ulloa, *Edge states in proximitized antiferromagnetic transition metal dichalcogenides*.
- **Natalia Cortés**, L. Rosales, P. A. Orellana, A. Ayuela and J. W. González, *Electric dipole induced by sulfur impurities in MoS₂ bilayers*.

D.4 Presentations

D.4.1 Oral presentations

- **Natalia Cortés**, O. Ávalos-Ovando, L. Rosales, P. A. Orellana and S. E. Ulloa, “Tunable spin-polarized edge currents in proximitized transition metal dichalcogenides”, XXI Simposio Chileno de Física, November 14th, 2018, Antofagasta, Chile.
- **Natalia Cortés**, O. Ávalos-Ovando, L. Rosales, P. A. Orellana and S. E. Ulloa, “Tunable spin-polarized edge currents in proximitized transition metal dichalcogenides”, Invited seminar at the Nanoscaled Experimental Physics Group, Universidad Técnica Federico Santa María, August 7th, 2018, Valparaíso, Chile.
- **Natalia Cortés**, O. Ávalos-Ovando, L. Rosales, P. A. Orellana and S. E. Ulloa, “Efectos de proximidad magnética en dicalcogenuros de metales de transición”, Invited seminar at the 4US group, Universidad Técnica Federico Santa María, September 6th, 2018, Santiago, Chile.
- **Natalia Cortés**, O. Ávalos-Ovando, L. Rosales, P. A. Orellana and S. E. Ulloa, “Spin polarized edge states in ferromagnetized transition metal dichalcogenides”, Panoramas, May 23th, 2018, UTFSM-PUCV, Valparaíso, Chile.
- **Natalia Cortés**, O. Ávalos-Ovando, L. Rosales, P. A. Orellana and S. E. Ulloa, “Spin polarized edge states in proximitized ferromagnetic transition metal dichalcogenides”, APS March Meeting, March 7th, 2018, Los Angeles, CA, USA.
- **Natalia Cortés**, O. Ávalos-Ovando, L. Rosales, P. A. Orellana and S. E. Ulloa, “Efectos de proximidad en dicalcogenuros de metales de transición”, IV Energy Workshop, November 16th, 2017, Universidad Católica del Norte, Antofagasta, Chile.

- **Natalia Cortés**, L. Rosales, P. A. Orellana, A. Ayuela and J. W. González, “Cálculos de primeros principios basados en dicalcogenuros de metales de transición”, III Energy Workshop, October 6th, 2016, Universidad Católica del Norte, Antofagasta, Chile.

D.4.2 Posters presentations

- **Natalia Cortés**, L. Rosales, P. A. Orellana, A. Ayuela and J. W. González, “The effects of impurities on the structural and electronic properties of MoS₂ bilayers”, Workshop on spins, valleys and topological states in 2D and layered materials, June 4th, 2017, Ohio State University, Columbus, USA.
- **Natalia Cortés**, L. Rosales, P. A. Orellana, A. Ayuela and J. W. González, “The effects of impurities on the structural and electronic properties of MoS₂ bilayers”, APS March Meeting, March 13th, 2017, New Orleans, LA, USA.
- **Natalia Cortés**, L. Rosales, P. A. Orellana, A. Ayuela and J. W. González, “Efectos de impurezas en una bicapa de MoS₂”, VIII Escuela de Nanoestructuras, January 10th, 2017, Universidad Técnica Federico Santa María, Valparaiso, Chile.
- **Natalia Cortés**, L. Rosales, L. Chico, M. Pacheco and P. A. Orellana, “Transport Coefficients and Quantum Interference effects in trilayer Silicene flakes”, Graphene Conference, April 19th, 2016, Genova, Italy.

Appendix E

E.1 Fellowships

- 26-03-2014 – *Student Fellowship*. Awarded with “Ayudantía de Investigación” for four semesters of academic year, Convenio de desempeño FSM1204 “Internalización de Doctorados”, UTFSM, Valparaíso, Chile.
- 21-11-2014 – *Student Fellowship*. Awarded with “Programa Incentivo a la Investigación Científica”, “Estudio de las propiedades termoeléctricas en sistemas compuestos por multicapas de grafeno”, for ten months, DGIIP, UTFSM, Valparaíso, Chile.
- 05-02-2016 – *Student Fellowship* Awarded with “Becas de Doctorado Nacional año Académico 2016”, Conicyt, for five semesters of academic year, Santiago, Chile.
- 26-04-2018 – *Student Fellowship*. Awarded with “Programa Incentivo a la Investigación Científica”, “Spin polarized edge states in proximitized ferromagnetic transition metal dichalcogenides”, for ten months, DGIIP, UTFSM, Valparaíso, Chile.
- 31-08-2018 – *Student Fellowship*. Awarded with “Convenio de beca término de tesis de doctorado”, for three months, DGIIP, UTFSM, Valparaíso, Chile.

E.2 Internships

- 07-08-2015 – *Student Internship*. Awarded with “Pasantía en el Extranjero”, Convenio de desempeño FSM1204 “Internalización de Doctorados”, UTFSM, Valparaíso, Chile. For six months 15/11/2015 - 15/06/2016 in Donostia International Physics Center, San Sebastián, Spain. Responsible professors: Jhon González and Andrés Ayuela.

- 08-02-2017 – *Student Internship* Conicyt Chile. For four months 11/03/2017 - 20/07/2017 in Ohio University, Athens, Ohio, USA. Responsible professor: Sergio Ulloa.
- 11-10-2017 – *Student Internship*. Awarded with “ Convenio de beca pasantías y estadías de investigación”, DGIIP UTFSM, Valparaíso, Chile. For two months 11-01-2018 - 11-03-2018 in Ohio University, Athens, Ohio, USA. Responsible professor: Sergio Ulloa.